Faculty of Science and Engineering
Department of Petroleum Engineering

Shale Play Assessment of the Goldwyer Formation in the Canning Basin Using Property Modelling

Munther Alshakhs

This thesis is presented for the Degree of
Master of Philosophy
of
Curtin University

June 2017

Declaration

To the best of my knowledge and belief this thesis contains no material previously published by any other person except where due acknowledgment has been made.

This thesis contains no material which has been accepted for the award of any other degree or diploma in any university.

Signature: _____

Date: 6-6-2017

Abstract

There is an increasing interest in the Goldwyer Formation of the Canning Basin as a potentially prospective shale play. This Ordovician unit is one of the most prominent source rocks in the Canning Basin and has been regarded as highly prospective shale play. This study assesses the potential prospectivity of this source rock as an unconventional hydrocarbon resource. Considering the sparsity of wells penetrating the Middle Ordovician Goldwyer across the vast under-explored area of the Canning Basin, a basin-wide study of the source rock is not warranted. Instead, Goldwyer assessment is carried out only for the Barbwire Terrace, a sub-division of the Canning Basin.

This source rock assessment includes the estimation of key shale play properties, such as total organic carbon, total porosity, water saturation, and brittleness. Each property was estimated from available well data by testing multiple estimation methods. TOC values were derived from multiple regressions of different well data. A simplified Archie's equation was used to estimate water saturation. Density porosity method was mainly used for total porosity estimations. As for brittleness, sonic data was utilized to estimate brittleness index along with density. Thermal maturity was also assessed using Rock-Eval data from Goldwyer rock samples.

Each property was then modelled across the Goldwyer Formation within the terrace. This provided geostatistical estimates on the propagation of such properties. In order to generate sweet spot maps for the Barbwire Terrace, averaged maps of different properties were combined in a weighted manner. This approach attempts to simplify the complexity of unconventional resource assessment, which therefore has provided a single product evaluating the prospectivity of the Goldwyer as a hydrocarbon resource.

Results have shown that TOC and porosity are the most deciding factors for the prospectivity of this source rock. Corresponding values of both properties can be too small where the Goldwyer would be deemed non-prospective. Nonetheless, sweet-spot maps show that the most prospective zone is the Upper Goldwyer (Goldwyer I), followed by the upper parts of the Lower Goldwyer (Goldwyer III). More specifically, southern flanks of north-western and middle regions of the Barbwire Terrace tend to be more prospective. A stricter approach where cut-off values were applied for each property showed that sweet-spot maps are only prospective in the southern flanks of the middle Barbwire Terrace of Goldwyer I.

Table of Contents

Table of Figures

List of Tables

Acknowledgments

Firstly, I would like to express my sincere gratitude to my advisor Professor Reza Rezaee for the continuous support of my postgraduate research, for his patience, and immense knowledge. His guidance and advice helped me throughout all stages of my research.

Besides my advisor, I would like to thank Dr. Hongyan Yu for her insightful comments and valuable help and feedback on different parts of the research.

My sincere thanks also go to Schlumberger for their generous donation of *Petrel* licenses and Saudi Aramco for sponsoring my postgraduate studies at Curtin University.

Chapter 1. Introduction

1.1 Canning Basin Geological and Structural Settings

The Canning Basin is located in the north-western part of Australia with an area greater than 595,000 km^2, making it the largest sedimentary basin in WA (*Summary of Petroleum Prospectivity: Canning Basin*, 2014). The basin is bounded by the Precambrian Kimberley Block from the north and the Pilbara and Musgrave Blocks to the south. The Amadeus Basin is located to the east of the Canning Basin, and the Warri Arch borders the Officer and Canning Basins in the southeast (Cadman et al., 1993).

The sedimentary deposition of the Canning Basin ranges in age from Ordovician to Cretaceous. The basin is simply an intracratonic depression between the Pilbara and Kimberley Blocks that was developed in the Early Paleozoic. It underwent five major tectonic events. The first event was subsidence due to an extension in the Early Ordovician (Brown et al., 1984). In the Early Devonian, a compression and erosion event took place. This was followed by another extension and subsidence event in the Late Devonian. A sequence of compression and subsidence events was in effect during the middle and Late Carboniferous to Permian. Finally in the Early Jurassic, erosion and transpressional uplift events took place. The effect of those tectonic events is reflected in the basin, especially the northern part where it's most affected by major faulting (*Summary of Petroleum Prospectivity: Canning Basin*, 2014).

The tectonic extension had triggered sedimentary deposition in the Canning Basin in the Early Ordovician over an eroded Precambrian surface. During this time, northwest transgressions had initiated a uniform sedimentary deposition across the whole basin (Brown et al., 1984), and it is believed that the transcontinental Larapintine Seaway connected the Canning Basin to the Amadeus Basin and other central basins (Cook & Totterdell, 1990). This was responsible for the deposition of paralic sandstones, intertidal and subtidal shale, siltstones, and carbonates (Upper and Lower Nambeet Formation). The carbonates section of the Willara Formation were widely developed during the Mid-Late Arenigian (Floian) (Cadman et al., 1993). The succession of the Lower Ordovician to the Lower Silurian is a relatively conformable sedimentary section deposited in marine, marginal marine, and terrestrial environments. Devonian, Carboniferous, or Permian strata overlay the previous section unconformably. The Ordovician-Silurian succession is divided into two sections; the Lower-Middle Ordovician, which contains the Nambeet, Willara, Goldwyer and Nita formations, and the overlying Middle Ordovician – Lower Silurian Carribuddy Group (McTavish & Legg, 1976; Nicoll et al., 1994; Haines, 2004).

Macro- and microfossils are well-preserved in the Lower-Middle Ordovician strata. Various fossil studies have been done on trilobites, graptolites, brachiopods, and conodonts (Nicoll et al., 1994; Laurie, 1997; Haines, 2004). Conodonts have shown to be most suitable for correlation within the basin and with other Australian Ordovician basins.

As the sedimentary deposition slowed down during the Middle Ordovician, shallow epeiric sea and subtidal conditions were in effect, which resulted in the deposition of the carbonates and fine-grained clastics of the Goldwyer Formation (Forman & Wales, 1981). The diagenetic process of the dolomitized limestones had essentially formed the Nita Formation.

Restricted marine conditions caused by transgressions from the west were over most parts of the basin during the Silurian – Mid Devonian. This resulted in the development of the evaporitic section of the Carribuddy Formation, especially in the depressed Kidson Sub-basin (Brown et al., 1984). In the Early Devonian, the Tandalgoo Sandstone was deposited in the southern sub-basins. The clastics of the Poulton Formation is thought to be an upper Tandalgoo equivalent in the northern part of the basin (Cadman et al., 1993).

In the Late Devonian, reef complexes of the Pillara Formation had formed in the shallow marine terraces to the south of the fault-bounded Fitzroy Trough. Further south into the basin, the fine-grained clastics were deposited (Gogo Formation). Further depression of the Kidson Sub-basin during the Givetian (Middle Devonian) resulted in the deposition of carbonates and minor evaporates units of Mellinjerie Limestone overlaying the Tandalgoo Sandstone. Deposition in the Kidson Sub-basin had effectively stopped from Fammenian to Late Carboniferous (Cadman et al., 1993).

In the northern part of the Canning Basin, a regression in the Early Famennian had left the entire southern margin of the Fitzroy Trough and fault blocks on the northern flank exposed (Playford, 1980). Resultant erosion in the northern flank produced the breccias of the Napier Virgin Hills Formation. The Clanmeyer Formation and the subsequent Luluigui Formation were deposited at this time in the Fitzroy Trough (Cadman et al., 1993).

A second reef build-up had developed during the Late Famennian forming the Nullara Limestone. This was followed by the shallow marine deposits of the Fairfield Group over parts of the Lennard Shelf, Barbwire, and Jurgurra Terraces (Druce & Radke, 1979). The Anderson Formation of marine and continental clastics and carbonates was deposited in the Fitzroy Trough in the Early Carboniferous. This was mainly triggered by a subsidence of the trough.

A basin-wide uplift and erosion took place from the Westphalian to the Stephanian (Late Carboniferous). Further faulting in the Fitzroy Trough had developed during a subsequent basin-wide subsidence event in the Stephanian to the Sakmarian (Late Carboniferous to Early Permian) (Yeates et al., 1984; Cadman et al., 1993). This was followed by a basin-wide transgression in the Early Permian, which resulted in the deposition of the marine Grant Formation. The Paterson Formation in the south of the basin is thought to be the Grant Formation equivalent (Towner & Gibson, 1983).

The Poole Sandstone was deposited in most of the Canning Basin in the Late Sakmarian (Crowe et al., 1978). This section was overlain by the shale, siltstone and marine sequence of the Noonkanbah Formation. A regression in the Late Artinskian led to the deposition of the Triwhite Sandstone (Carey, 1976). Further north, fluvial and deltaic sediments of the Liveringa Group were deposited in the Fitzroy Trough. A later transgression in the Early Triassic deposited the Blina Shale in the Fitzroy Graben, which was followed by a regression in the Late Scythian that led to the deposition of the overlying fine-grained Erskine Sandstone (Cadman et al., 1993).

A regional erosional unconformity in the Canning Basin was caused by Late Triassic to Early Jurassic rifting. En-echelon anticlinal structures in the Fitzroy Graben were formed by movements of the bounding faults of the trough. Salt structures are also thought to have formed during this time in the Kidson Sub-basin (Brown et al., 1984). The erosional event of the Canning Basin ended in the Middle Jurassic and deposition resumed.

The fluvial, to deltaic and shallow marine Wallal Sandstone was deposited in the Middle Jurassic, making it the oldest Jurassic strata in the basin. This unit was overlain by the Alexander Formation, which mainly consists of mudstones and tidal sandstones. The Jarlemai Siltstone was then deposited during a period of maximum transgression in the Kimmeridgian to earliest Cretaceous. The Barbwire Sandstone and the Meda Formation, which are coarse fluvial clastics, were deposited along the northern edge of the basin (Yeates et al., 1984).

The shallow marine portion of the Broome Sandstone was deposited in the Early Cretaceous above the Jarlemai Siltstone. This sandstone unit is widespread across the basin and was part of a regressive sequence (Cadman et al., 1993). An overview of the stratigraphy of the Canning Basin can be seen in Figure 1.1.

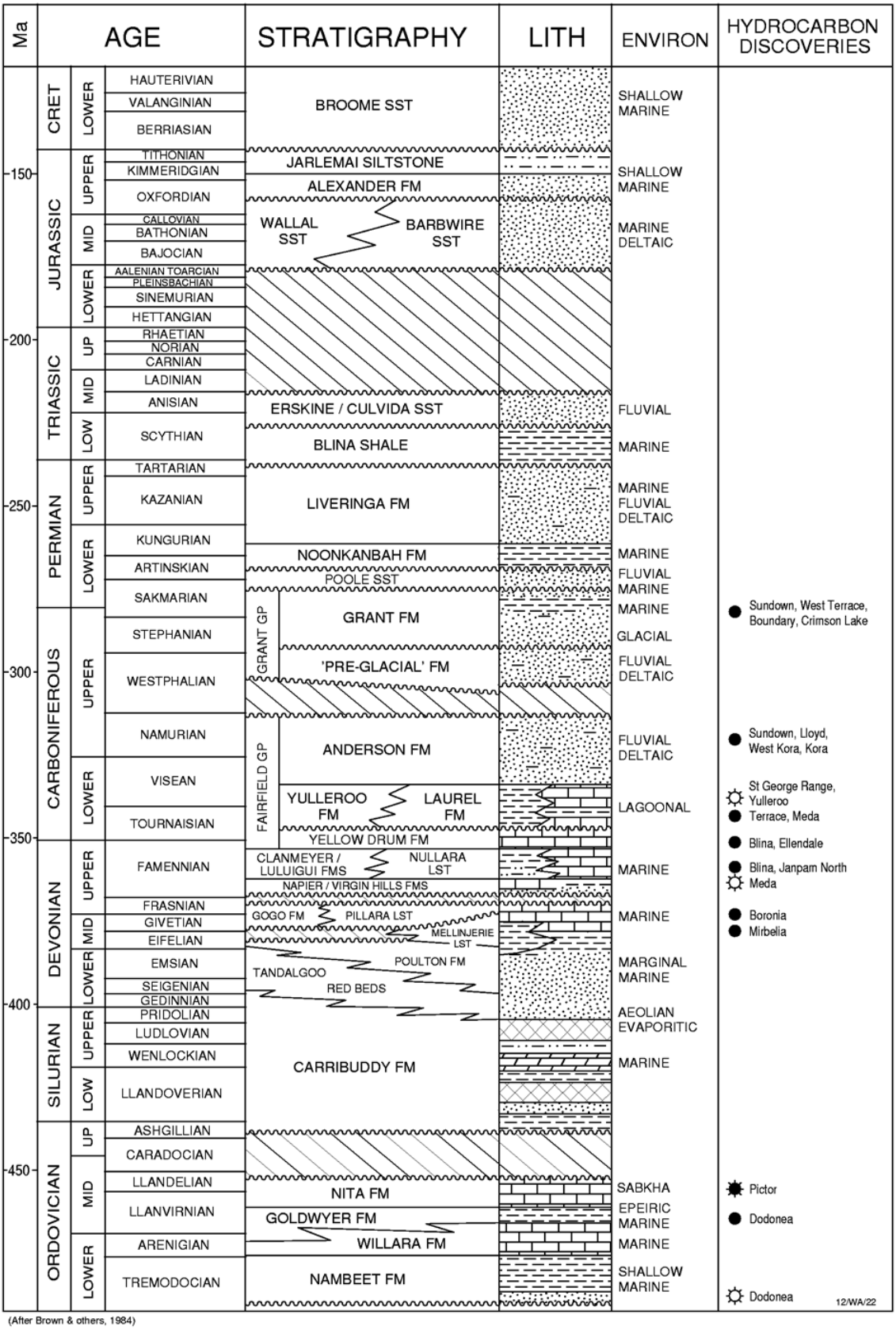

Figure 1.1 Canning Basin general stratigraphy (Cadman et al., 1993)

1.2 Canning Basin Subdivisions

The Canning Basin is subdivided into smaller sections with NW-SE trends. Those subdivisions are mainly platforms, shelves, terraces, troughs, and sub-basins. The Canning Basin has a mid-basinal arch that separates two major troughs of the basin; a northern trough and a southern one (Apak & Carlsen, 1997). Those troughs are bounded by outer shelves (Figure 1.2).

The northern trough of the Canning Basin consists of the Fitzroy Trough and the Gregory Sub-basin. It is thought to be a Paleozoic rift as it has a mainly Paleozoic rock column of up to 15 km thick. This Paleozoic rift is bounded on the south by complex down-faulted blocks; the Barbwire and Jurgurra terraces. Those terraces have a shallow basement of generally less than 2 km deep (Cadman et al., 1993).

The mid-basinal arch is composed of the relatively shallow Broome and Crossland platforms. The relatively thinner sedimentary section thickens toward either northern or southern troughs. However, exploration efforts in the mid-basinal platforms have had many good oil and gas shows (*Summary of Petroleum Prospectivity: Canning Basin*, 2014).

The southern trough of the basin includes the Kidson and Willara Sub-basins. Those sub-basins have thicker sedimentary sections, 4-5 km thick, than the mid-basinal platform but not as thick as the northern trough. Sediments of this part of the basin are predominantly Ordovician to Silurian and Permian in age (Apak & Carlsen, 1997).

The marginal shelves of Anketell and Tabletop in the south and Lennard Shelf in the north have relatively shallower basements. The Lennard Shelf is also the most explored part of the basin and has commercial oil fields (*Western Australia's Petroleum and Geothermal Explorer's Guide*, 2014).

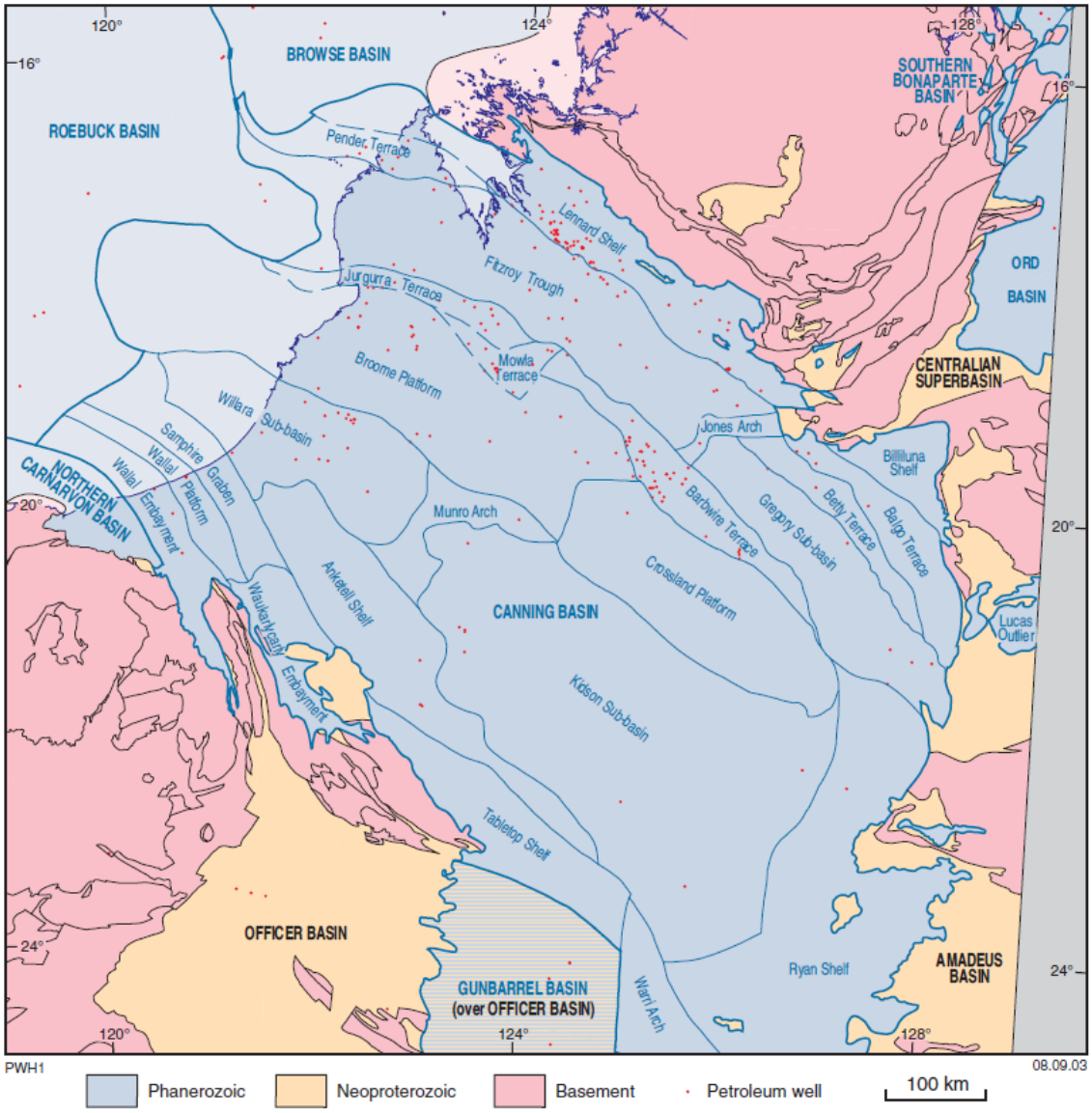

Figure 1.2 Structural settings and subdivisions of the Canning Basin (Haines, 2004).

1.3 Exploration History

The Canning Basin is an underexplored basin. The Summary of Petroleum Prospectivity: Canning Basin (2004) puts this into perspective by explaining that a similar basin in North America would typically have 500 wells per 10,000 km^2, where the Canning Basin has only 4 wells per the same area of 10,000 km^2.

When a number of water wells showed some oil traces in a Lower Carboniferous limestone rock back in 1919, hydrocarbon exploration interest has started. This led to minor exploration efforts during the 1920s, in the Canning Basin led by Freney Oil Company.

The increase in oil prices in the late 1970s – early 1980s led to further oil exploration. The initial drilling focus was to the northern part of the basin. The first commercial oilfield discovery was in the Lennard Shelf, the most explored part of the basin to date. The primary targets of exploration were Devonian and Permian-Carboniferous reservoirs.

The first significant oil discovery after the 1980s exploration work, was in 2011 when Buru Energy targeted a light oil bearing zone of a Carboniferous dolomitized limestone, the Laurel Formation. This has reignited exploration and followed further exploration and appraisal work (*Summary of Petroleum Prospectivity: Canning Basin*, 2014).

Shale oil and gas interest have been lately on the rise in the Canning Basin, as it is believed to have significant hydrocarbon potential. Major international companies, such as Hess, ConocoPhillips, Apache, and Mitsubishi are joining ventures with smaller independent companies to further explore and test different shale plays prospectivity in the basin (*Western Australia's Petroleum and Geothermal Explorer's Guide*, 2014).

In 2013, the US EIA (Energy Information Administration) reported that the Goldwyer Formation of the Canning Basin has the highest shale gas potential in Australia, with estimated potential of about 225 TCF of recoverable shale gas, potentially making it the 8th largest shale gas play in the world.

Further work on volumetrics estimation was done by Triche and Bahar (2013). Table 1.1 summarizes those estimations alongside other previous work. This shows great potential for the Goldwyer Formation, making it the most prospective shale play in the Canning Basin.

Table 1.1 Comparison of volumetric estimates of selected shale gas plays in the Canning Basin (Triche & Bahar, 2013).

	GOLDWYER III		GOLDWYER FM			LOWER LAUREL		LAUREL FM
	Triche and Bahar 2013		ACOLA 2013	EIA 2013	EIA 2011	Triche and Bahar 2013		ACOLA 2013
	Deterministic	Probabilistic				Deterministic	Probabilistic	
GIIP	22.2 (783.9)	24.5 (867.4)	730.6 (2580)*	706.8 (2496)*	721.2 (2547)*	5.5 (193.6)	7.7 (271.5)	11.9 (420)*
Recoverable Resource	3.3 (117.6)	3.7 (130.1)	10.9 (387.0)	10.6 (374.4)*	10.8 (382.1)*	0.8 (29.0)	1.2 (40.7)	1.8 (63.0)
Risked GIIP [50% RF]	11.1 (392.0)	12.3 (433.7)	365.2 (1290)*	353.3 (1248)*	360.6 (1273.5)*	2.7 (96.8)	3.8 (135.8)	5.9 (210)*
Risked GIIP [30% RF]	6.6 (235.2)	7.4 (260.2)	21.9 (774)	21.2 (748.7)	21.6 (764.0)	1.6 (58.1)	2.3 (81.5)	3.6 (126)*
Risked Recoverable Resource [30% RF, 15% ReF]	1.0 (35.3)	1.1 (39.0)	3.3 (116.1)*	3.2 (112.3)*	3.3 (114.6)*	0.2 (8.7)	3.5 (12.2)	5.4 (18.9)

RF: Risk Factor
ReF: Recovery Factor
*extrapolated here from published data

1.4 Goldwyer Formation

1.4.1 Background

The Goldwyer Formation has an average thickness of around 400 m, where the thickest intersection is recorded in Blackstone 1, a Lennard Shelf Sub-basin well, with 739 m of Goldwyer section. Data suggest that the formation is even thicker in this area as the well reached total depth in the Goldwyer. Willara 1, a Willara Sub-basin well, shows the thickest complete Goldwyer section of 736 m (Legg, 1978). Stratigraphy interpretations are mainly based on conodonts (Nicoll, 1993), as discussed earlier.

1.4.2 Lithofacies and Deposition

The Goldwyer Formation is generally scarcely pyritic and mainly consists of mudstone and carbonate, with alternating ratios of the two across the basin. The Goldwyer in deeper parts of the basin tends to be mudstone-dominated. In platforms and terraces, however, it leans towards being carbonate-dominated or at least with higher carbonate to mudstone ratios. In general, carbonate has been initially deposited as limestone and undergone substantial dolomitization in some parts across the Goldwyer. Clastic rocks are generally scarce or limited to fine-grained sandstones that increase in presence in the south-eastern part of the basin. Different sections of the Goldwyer can vary from being weakly to strongly dolomitic or calacarious. Bioturbation is sometimes observed in lean sections only, since organic carbonates and mudstones accumulate in anoxic environments. Discrete cylindrical and branching burrow systems to general churning of the sediments can be observed (Haines, 2004).

Cyclic strata are observed in the Goldwyer Formation. They are more predominant in the platforms and terraces with cyclicity scale ranges from metres to tens of metres. Fully cored Goldwyer sections in the Barbwire Terrace show that the lower Goldwyer is mainly laminated mudstone with thin limestone interbeds, which is succeeded by a grading interval of stylonodular wackestone to fewer amounts of packstone or grainstone. This is then superimposed by the next cycle of laminated mudstone (Haines, 2004).

The mudstone strata and the limestone interbeds of the Goldwyer Formation are locally replaced by massive carbonate build-ups along the Admiral Bay Fault Zone, in the Willara Sub-basin. Those build-ups are sometimes referred to as the Admiral Bay carbonate group (Russell & Edwards, 1984; WAPIMS, 2017). They have not been observed elsewhere in the basin and they are extensively altered by mineralized vein systems. Individual build-ups reach 350 m in thickness and can be 500 m wide. This is interpreted as microbial bioherms localized along the active fault scarps. Throughout deposition of most of the Goldwyer Formation, bioherm tops remained in the surf zone (McCracken, 1994; McCracken et al., 1996; McCracken, 1997).

Given the complex structure of the Canning Basin, the Goldwyer Formation is expected to be variable in depth, lithology, and thickness across the basin. A west-east cross section of wells in the Willara Sub-basin, Broome Platform, and Barbwire Terrace shows some of those variabilities (Figure 1.3). Most notably is the thickness variation of the Goldwyer section where it appears to be more constantly thick in the Broome Platform than it is in the other two subdivisions. A distinct change in thickness and lithology can be observed between Willara 1 and Great Sandy 1 of the Willara Sub-basin, where Great Sandy 1 was drilled on the upthrown block of the Admiral Bay Fault whilst Willara 1 was drilled on the down-thrown side of the fault (Menzel & Norlin, 1982; WAPIMS, 2017).

Different subdivisions were made to the Goldwyer Formation. Multiple geological reports of some wells in the Broome Platform have noted the presence of a lower shale, a middle limestone, and an upper shale units (Figure 1.4). The middle limestone interval varies in development across the basin but is mainly well developed in platforms and terraces. Western Mining Corporation carried out a study on some wells in the Barbwire Terrace and have identified four units in the Goldwyer, WMC units 1 to 4 in ascending order (Foster et al., 1986; Winchester-Seeto et al., 2000). The two subdivision approaches are fairly similar with WMC Units 1 and 2 are basically equivalent to the lower shale interval of the first subdivision approach.

Macrofossils of the Goldwyer indicate an open marine depositional environment. Looking into facies individually, water depths are believed to be alternating throughout the deposition process, where laminated mudstones are mostly deposited during lagoon or subtidal shelf conditions, and the succeeding wackestone, packstone, and grainstone are associated with higher energy intertidal and shoal conditions. This also explains the cyclic behaviour observed in the formation (James, 1984; Haines, 2004).

The organic component *Gloeocapsomorpha Prisca* is abundant in the upper Goldwyer interval. Such component is found to be less concentrated to fairly scarce in lower to middle Goldwyer units. Such distribution can be somewhat variable across the basin where even lithofacies changes influence the occurrence of organic matter. Nevertheless, tested Ordovician oil samples by Edwards et al. (1997) showed a clear presence of the *Gloeocapsomorpha Prisca* component indicating that the Goldwyer Formation is a primary source rock in the Ordovician strata (Haines, 2004).

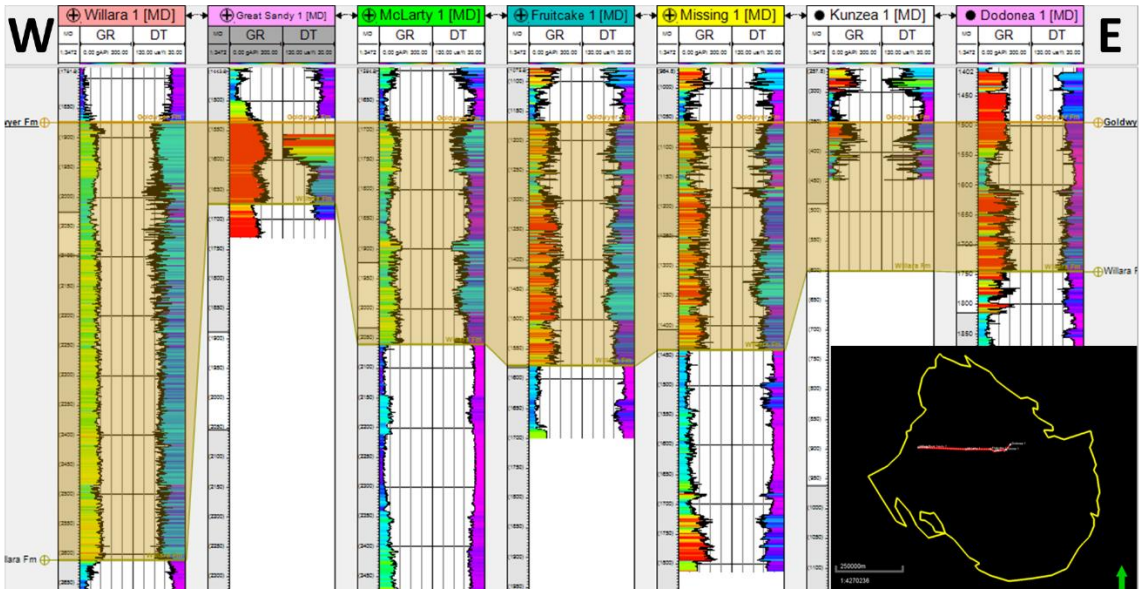

Figure 1.3 West-East well cross section of some wells in the Canning Basin showing variations in thickness and lithology of the Goldwyer Formation. All displayed wells are within Willara Sub-basin, Broome Platform, and Barbwire Terrace.

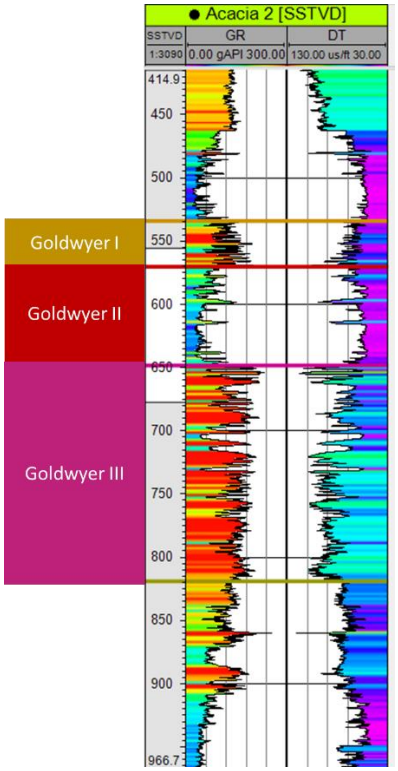

Figure 1.4 The Goldwyer Formation is subdivided here into 3 zones; upper shale (Goldwyer I), middle limestone (Goldwyer II), and lower shale (Goldwyer III). This is the Goldwyer subdivision approach utilized in this study. Acacia 2 is one of the Barbwire Terrace wells.

1.4.3 Thermal Maturity

In the Goldwyer Formation, maturation measurements are very sparse. The source rock data available are insufficient for a thorough source rock maturity analysis. Vitrinite reflectance measurements have limited value as woody plants had not evolved during the Ordovician. That said, the Goldwyer Formation is believed to have excellent source rock potential (Cadman et al., 1993). Maturation modelling developed by Brown et al. (1984) suggests that the Goldwyer Formation is in the post-oil generation in the Fitzroy Trough and within the window of oil generation in most of the southern Canning Sub-basins and the mid-basin platforms (Cadman et al., 1993).

The Broome Platform and the Fitzroy Trough are thought to be in the post-mature window. The part of the Broome Platform near the present-day coastline is immature (Figure 1.5) (*Summary of Petroleum Prospectivity: Canning Basin*, 2014). Nonetheless, these conclusions are based on limited maturation data, and modelling estimates might be updated with more data acquired for the Goldwyer Formation.

The Goldwyer Formation is oil and gas prone with kerogen types II and III (mostly type II). Many Goldwyer samples appear to be in the oil window, which could potentially be the biggest issue for shale gas exploration for the Goldwyer Formation in the Canning Basin (Triche & Bahar, 2013).

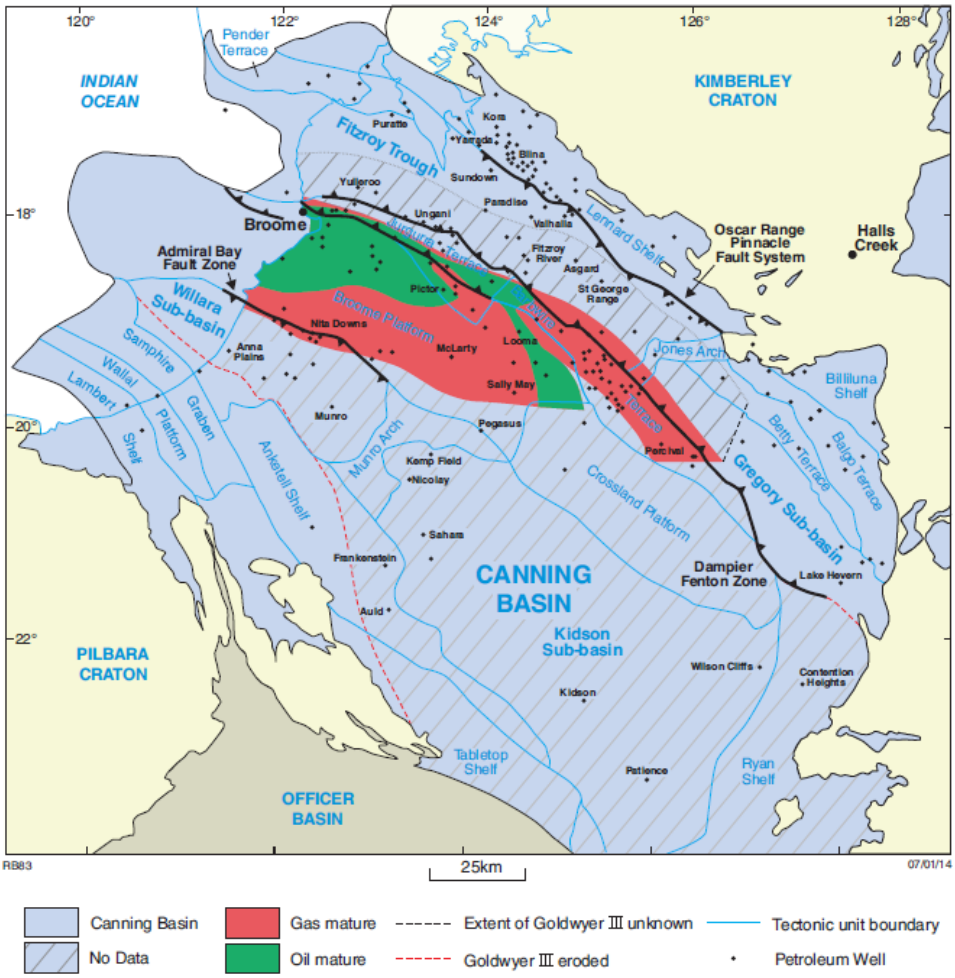

Figure 1.5 Maturity map for the Goldwyer Formation, Canning Basin (*Summary of Petroleum Prospectivity: Canning Basin*, 2014).

Chapter 2. Methods and Materials

2.1 Data Availability

As discussed earlier, the Canning Basin is a very large under explored Paleozoic basin. The sparsity of wells, and/or the lack of wells penetrating the relatively deep Ordovician Goldwyer Formation make the shale play assessment not warranted in some parts of the basin. Hence, searching the database for all wells in the Canning Basin, and categorizing them in terms of location, depth, and available well data was a necessary initial step for the study. Such information allows identifying areas with highest data coverage, and hence more warranted for research (Table 2.1). The Barbwire Terrace was selected to be the area of study in this research given the relatively wider range of available well data, the number of wells, and thermal maturity of the Goldwyer Formation in the Barbwire as it will be discussed in section 2.2. All data were provided by the Government of Western Australia, Department of Mines and Petroleum's database, *WA Petroleum and Geothermal Information Management System (WAPIMS)*.

Table 2.1 Numbers of wells penetrating the Goldwyer Formation in different sub-divisions of the Canning Basin.

Canning Basin Subdivision	#Wells Penetrated Goldwyer
Broome Platform	24
Willara Sub-basin	11
Barbwire Terrace	7
Mowla Terrace	7
Kidson Sub-basin	3
Lennard Shelf	2
Anketell Shelf	1
Gregory Sub-basin	1
Munro Arch	1

After the Barbwire Terrace was selected, all relevant well data were loaded from the database. Data needed to be sorted, edited, and spliced in some cases. The primary software used for this research was Petrel.

Referring to literature and data available, key properties of thermal maturity, total organic carbon content, porosity, fluid saturation, and brittleness were estimated using various methods and verified with rock sample data whenever available.

2.2 Thermal Maturity in the Barbwire Terrace

The WAPIMS database includes some Goldwyer Rock-Eval data with limited vitrinite reflectance data points. T_{max} values from Rock-Eval are directly related to maturity information. It is defined as the

temperature that the maximum amount of hydrocarbon is released by the kerogen during the pyrolysis process. The value of T_{max} increases linearly as the source rock maturation increases. Hence, T_{max} can be used as a measure of the maturity of the source rock (Dellisanti et al., 2010).

T_{max} can also be converted to vitrinite reflectance (R_o) for more familiar maturity expression. Jarvie et al. (2001) derived a relationship between the two variables, using data from the Barnett Shale in the Fort Worth Basin.

$$\%R_o = 0.018 \cdot T_{max} - 7.16 \quad (2.1)$$

This relationship does not hold for samples with very limited S2 or source rocks with kerogen type I. Wust et al. (2013) showed that Eq. 2.1 does not hold either for the Duvernay Shale in the Western Canadian Sedimentary Basin and suggested that this Barnett Shale derived-relationship should not be used for conversion calculation in new formation unless the relationship was verified. Dellisanti et al. (2010) state that T_{max} values in relation to oil and gas maturity windows vary based on organic matter and kerogen type.

The maturity stages of T_{max} data have been correlated with R_o for kerogen type III data and can be seen in Figure 2.1 (Dellisanti et al., 2010).

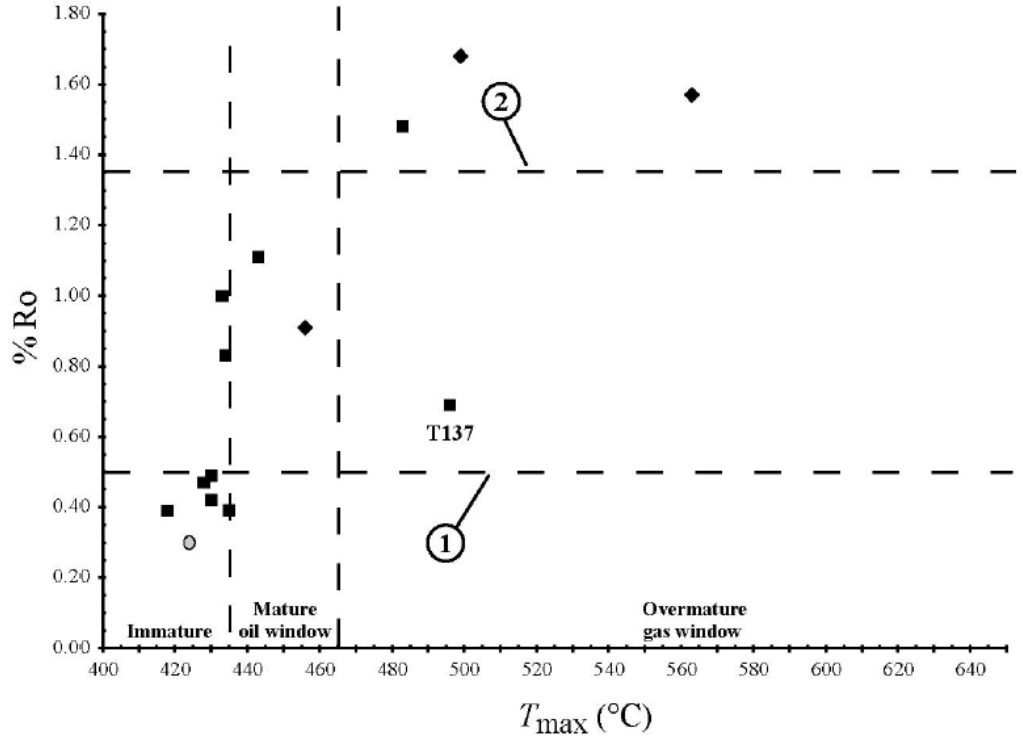

Figure 2.1 Cross-plot of R_o and T_{max}. 1 and 2 show the R_o boundaries of the oil window (Dellisanti et al., 2010).

This relationship provides direct maturity measurements from T_{max} and R_o to the related hydrocarbon generation window. Waples (1985) showed that different kerogen types lead to different T_{max} values for maturity phases (Table 2.2).

Table 2.2 Hydrocarbon generation windows for R_o and T_{max} (Waples, 1985).

		Immature	Mature (Oil Window)	Overmature (Gas Window)
R_o (%)		< 0.5	0.5 - 1.35	> 1.35
T_{max} (°C)	Kerogen Type I	< 445	445 - 460	> 460
	Kerogen Type II	<435	435 - 460	
	Kerogen Type III	<440	440 - 460	

Maturity data from Rock-Eval pyrolysis were analyzed from five wells in the Barbwire Terrace. Similar to the model proposed by Brown et al. (1984), cross-plot of T_{max} and HI (hydrogen index) suggests the Goldwyer Formation, in this terrace, is in the early to peak oil generation window (Figure 2.2). All available Rock-Eval data can be accessed as individual spreadsheets under each well in the Western Australia Petroleum and Geothermal Information Management System WAPIMS (2017).

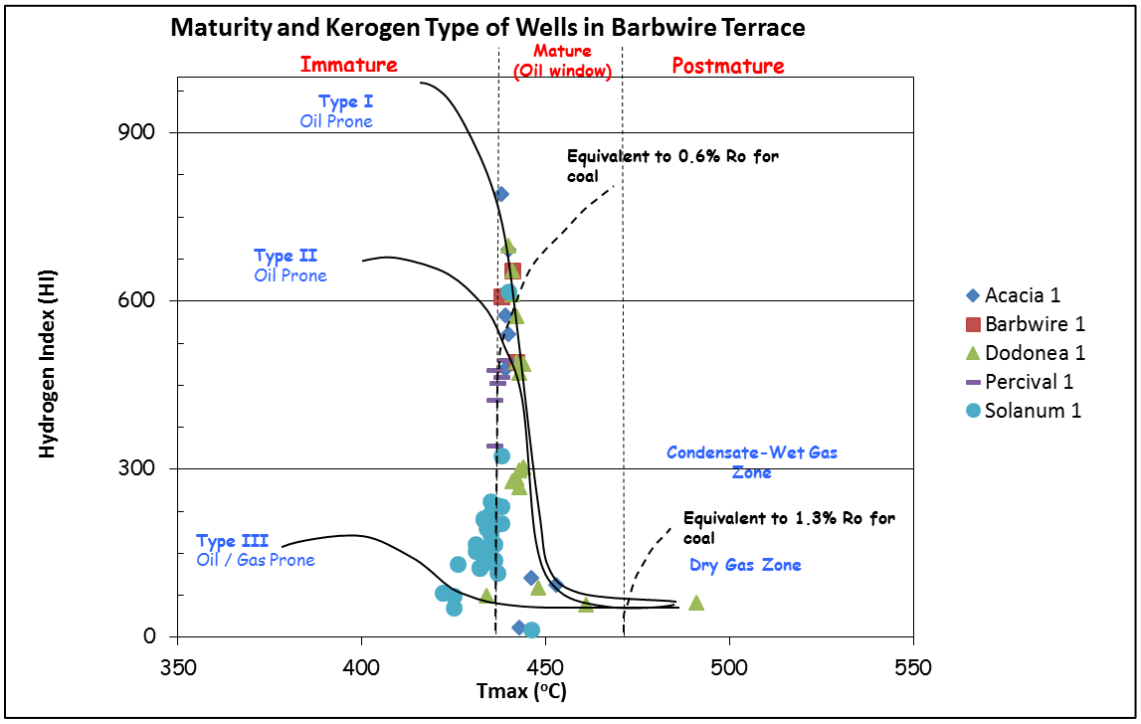

Figure 2.2 Maturation of the Goldwyer Formation in the Barbwire Terrace appears to be in the early to peak oil generation window.

2.3 Total Organic Carbon TOC

This property is a key factor in determining the prospectivity of any shale play. It significantly influences hydrocarbon production (Schmoker, 1989). TOC is traditionally measured in a laboratory from core data, sidewall plugs, and cuttings. Such measurements are relatively more accurate methods in TOC estimation. However, it provides non-continuous measurements of the source rock section as it has limited samples and is usually associated with higher costs and longer measurement time. To overcome these limitations, different continuous wireline data are often utilized to derive TOC.

Petrophysical properties of kerogen and TOC vary greatly to those of the hosting source rock matrix. The presence of TOC generally leads to higher gamma-ray (higher uranium content), lower density, higher resistivity, and slower sonic (Kamali & Mirshady, 2004; Sun et al., 2013). Consequently, different methods and approaches were introduced to estimate TOC from well log data.

The Schmoker method is a widely used approach, and it estimates TOC from formation density logs. In general, a shale mineral matrix density has an average of about 2.7 g/cc whereas the density of organic matter is about half of that. Thus, the presence of organic carbon will highly influence the formation bulk density and hence TOC can be calculated from density log when other factors for density variation are taken into consideration (Hester & Schmoker, 1987).

The density method subdivides shales into four components; rock matrix, pyrite, interstitial pores, and organic matter. Therefore, the bulk density of the formation is a function of those components and can be expressed as follows in Eq.2.2 (Schmoker & Hester, 1983):

$$\rho_b = V_o\rho_o + V_p\rho_p + \emptyset_i\rho_i + (1 - V_o - V_p - \emptyset_i)\rho_m \quad (2.2)$$

V = Volume fractions
$\emptyset$ = Porosity
ρ_b = Bulk density
m, p, i, and o are matrix, pyrite, interstitial pores (pore fluid), and organic matter, respectively.

Schmoker (1979) derived a linear relationship between pyrite and organic matter, empirically:

$$V_p = 0.135V_o + 0.0078 \quad (2.3)$$

Taking this relationship in Eq.2.3 and assuming the porosity changes in a shale rock are minimal and with low original values, to begin with, schmoker has simplified the relationship:

$$V_o = \frac{\rho - 0.992\rho_m - 0.039}{\rho_o - 1.135\rho_m + 1.675} \quad (2.4)$$

This can be expressed in terms of TOC, as:

$$TOC = \frac{(100\rho_o)(\rho - 0.992\rho_m - 0.039)}{R(\rho_o - 1.135\rho_m + 0.675)} \quad (2.5)$$

R = Ratio of weight percent organic matter to weight percent TOC.

Schmoker has derived TOC equations for specific shales in North America. Eq.2.5 is tailored for the Marcellus Shale of the Appalachian Basin (Schmoker, 1989). By combining his different derivations for various shale plays (Schmoker, 1979; Schmoker & Hester, 1983; Hester & Schmoker, 1987), we can use a more simplified/generalized version of his method, Eq.2.6:

$$TOC = \frac{157}{\rho_b} - 58.3 \quad (2.6)$$

Passey et al. (1990) method was proposed as an advanced technique to estimate TOC compared to the simple estimation from density or gamma-ray logs (Cluff & Miller, 2010). The $\Delta logR$ technique of Passey et al. (1990) includes estimating TOC from three methods; sonic/resistivity, neutron/resistivity, and density/resistivity logs. The approach evolves around the log separation that occurs between the resistivity and the other logs, due to the presence of organic matter (Sun et al., 2013).

Taking the sonic/resistivity log method as an example, a separation between the two curves will be observed along the intervals of 'hot' shales (presence of organic matter). The two logs are overlayed on the same track, with the resistivity log displayed in logarithmic and the sonic in linear scales (Figure 2.3). Slight modification to the scale length and interval might be required to emphasize the

separation of the logs. The mathematical expression to quantify this separation is in Eq.2.7 (Passey et al., 1990).

$$\Delta logR = \log\left(\frac{R}{R_{baseline}}\right) - P(\Delta t - \Delta t_{baseline}) \quad (2.7)$$

$\Delta logR$ is the separation between the two logs measured in logarithmic resistivity cycle.
R is the resistivity in Ω·m.
P is the ratio of the scaling of the two displayed curves. For example, P in Figure 2.3 is 0.02, since there is one resistivity cycle per 50 μs/ft of transit time ($P = \frac{1}{50} = 0.02$).
Δt is the sonic measurement in μs/ft.
$\Delta t_{baseline}$ is the sonic corresponding to $R_{baseline}$ in the lean shale interval (non-source rock).

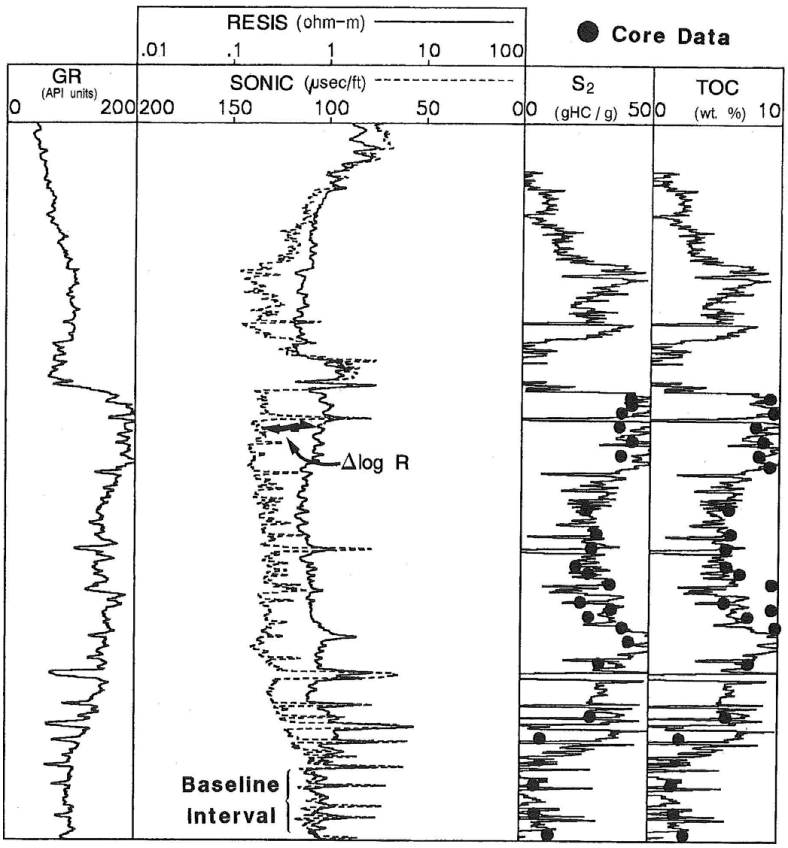

Figure 2.3 Illustration of the overlay and separation of the sonic and resistivity logs (Passey et al., 1990).

With the log separation quantified, TOC can be calculated using Eq.2.8.

$$TOC = \Delta logR \times 10^{[2.297-(0.1688\times LOM)]} \quad (2.8)$$

LOM is the level of maturity.

For any specific ΔlogR, TOC decreases as LOM increases (Cluff & Miller, 2010). LOM can be derived from maturity information, such as vitrinite reflectance R_o (Figure 2.4).

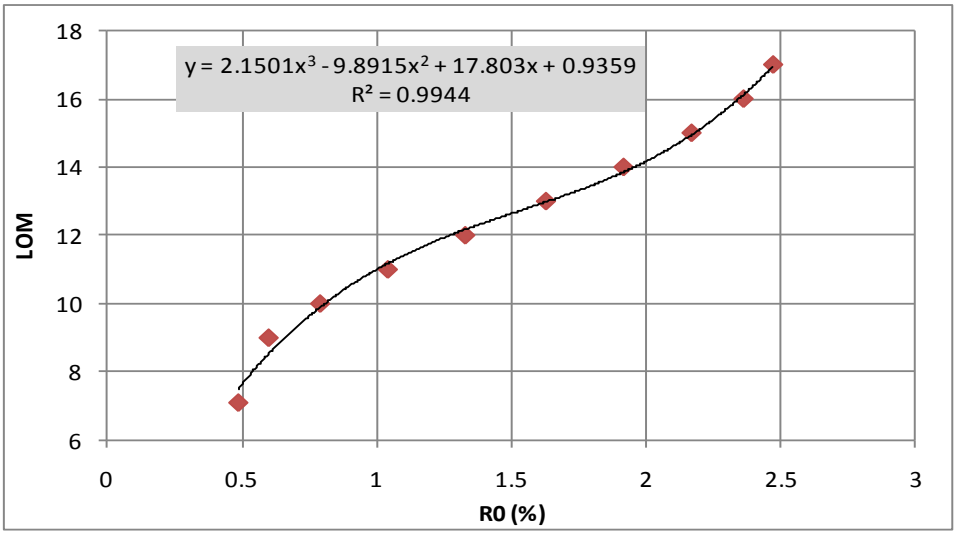

Figure 2.4 A polynomial of 3rd degree expresses the relationship between R_o and LOM.

There are some limitations associated with the approach of Passey et al. (1990). It might not be as reliable with high maturation levels, as resistivity logs do not continue increasing with maturity. They tend to fall back at some level of increasing maturity. Furthermore, TOC relationship was extrapolated after being derived and calibrated with low ΔlogR and LOM 6-9. This again might pose some issues when dealing with values at the far end of the spectra (Cluff & Miller, 2010).

The two approaches of Schmoker and Passey et al. are considered main techniques for TOC estimation. Such methods were utilized in this study to calculate TOC and then validated with TOC Rock-Eval measurements.

Another common approach in TOC estimation is data regression. Given there is sufficient TOC measurements, single and multivariate regressions are plotted to derive TOC from various wireline log data. This was also widely utilized and validated for this study.

2.4 Saturation

Estimating the resistivity values of water-filled porous rocks is the key step of estimating the water, oil, and gas saturations of a given formation. Accordingly, Archie (1942) introduced such a relationship using sandstone samples.

$$R_o = FR_w \tag{2.9}$$

Where R_o is the resistivity of the sand when all pores are filled with water, R_w is the brine resistivity and F is the formation resistivity factor.

F is generally a function of the type of the formation and its characteristics. Changes in permeability and porosity of the formation will influence the value of F (Figure 2.5). Hence, the formation resistivity factor and porosity have the following relationship:

$$F = \frac{1}{\emptyset^m} \tag{2.10}$$

By combining Eq.2.9 and Eq.2.10.

$$R_o = \frac{R_w}{\emptyset^m} \tag{2.11}$$

Where Φ is porosity and m is the cementation exponent, which is the slope of the line representing the relationship (Figure 2.5). For consolidated/unconsolidated sandstones, m is generally in the range from 1.3 to 2.0.

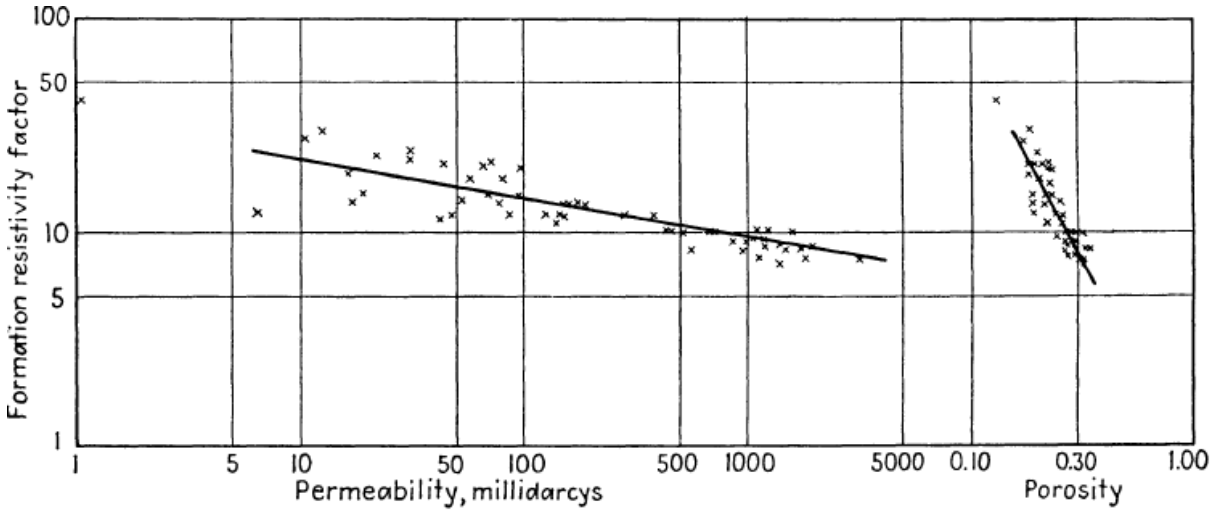

Figure 2.5 Permeability and porosity vs. formation resistivity factor (F) for consolidated sandstone core of the Gulf Coast (Archie, 1942).

In the case of the presence of oil or gas in the formation, Archie (1942) derived an equation to estimate the water saturation (S_w).

$$S_w = \sqrt[n]{\frac{R_o}{R_t}} \tag{2.12}$$

Substituting Eq.2.11 into Eq.2.12 gives:

$$S_w = \sqrt[n]{\frac{R_w}{\emptyset^m R_t}} \tag{2.13}$$

Where R_w is the brine resistivity, R_t is the log resistivity and n is the saturation exponent, whose value is ~2 for consolidated sandstones.

It is very difficult to estimate R_w from shales. They are not water producing formations, and shale salinity tends to be highly variable and hence substituting a value for R_w might be unreliable (Sondergeld et al., 2010; Labani & Rezaee, 2015). Archie's method assumes one value for water resistivity and does not account for different electrical contributions from different types of water partially filling the pores of shale. Therefore, this simplified model can be a source of error when used for shales as we can't account for the different electrical contributions coming from free water and clay-bound water in shale source formations (Glorioso & Rattia, 2012).

In a conventional sense, electrical current flows in the rock using the formation water as pathways. In shales, the abundance of clay and the associated clay-bound water increase these pathways and hence increase the ease of the electric current flow. This would lead to a reduction in the formation factor and, consequently, a reduction in m (cementation exponent) to a value smaller than 2 (Zhao et al., 2007; G. Yu & Aguilera, 2011; Labani & Rezaee, 2015).

Eq.2.12 is a simplified form of Archie's method and can be used to quantify water saturation of a shale interval. R_o is the resistivity of a lean shale in the interval, where it represents a shale rock with water-filled pores (Labani & Rezaee, 2015). R_t is simply the resistivity log along that shale interval. Saturation exponent n can be given the value of 1.7 as proposed by Luffel and Guidry (1992) as it provides a good match to water saturation derived from core data. With the water saturation estimated, the hydrocarbon saturation S_h can be calculated using Eq.2.14 (Glorioso & Rattia, 2012):

$$S_h = 1 - S_w \tag{2.14}$$

2.5 Total Porosity

There are different techniques used to measure porosity and permeability in petroleum shales in a laboratory. Sample crushing was one technique introduced by Luffel and Guidry (1992) to increase surface area. Porosity estimations of this method require bulk density, dry matrix density, bulk volume, and grain volume measurements. However, removal of capillary and clay bound water, pore access difficulties to gas, adsorption, sample size, crushing methods, crushed sample weight, and effect of pore pressure and overburden on microfractures are all different factors affecting the validity of those measurements (Sondergeld et al., 2010).

There are other direct porosity measurements of shales but they are still affected by some of the factors mentioned earlier. Those measurements include nuclear magnetic resonance NMR and high-pressure mercury injection capillary pressure MICP. NMR total porosities are validated with those of core measurements and they both agree for a wide range of shale plays (Jacobi et al., 2009). MICP measurements were typically done for shales to assess seal capacity (Sneider et al., 1997). Nonetheless, this method has recently become popular for estimating porosity for shale plays (Olson & Grigg, 2008).

Shale gas reservoirs have typically low porosities. They usually have a range of 3-10%. Reliable porosity estimations from petrophysical logs in shale gas is an important tool for economic shale evaluation. Different methods were developed for porosity measurements in the conventional reservoirs. However, porosity in shale reservoirs has more complexity in the estimation of variable mineralogy, kerogen low-density and distribution, fluid types, and complex nano- to micropore volumes (Sondergeld et al., 2010; Franquet et al., 2012).

Total porosity is commonly derived from density log for a given formation (density porosity, DPHI). Eq.2.15 shows the bulk density in a general rock (Labani & Rezaee, 2015).

$$\rho_b = \rho_{ma}(1 - \emptyset) + \rho_f \emptyset \tag{2.15}$$

Where ρ_b is bulk density, ρ_{ma} is matrix density, ρ_f is fluid density and $\emptyset$ is total porosity.

The expression can be customized for shale reservoirs by adding the TOC component as follows:

$$\rho_b = \rho_{ma}(1 - \emptyset - V_{TOC}) + \rho_f \emptyset + \rho_{TOC} V_{TOC} \tag{2.16}$$

V_{TOC} is TOC volume fraction

Since TOC is commonly expressed in weight fraction and not volume fraction, Eq.2.16 is modified accordingly in Eq.2.17 while solving for porosity (density porosity):

$$\emptyset_{density} = \frac{(\rho_{ma} - \rho_b) + \rho_b \left(w_{TOC} - \rho_{ma} \frac{w_{TOC}}{\rho_{TOC}} \right)}{\rho_{ma} + \rho_f} \tag{2.17}$$

Where $\emptyset_{density}$ is the total porosity derived from density (DPHI) and w_{TOC} is TOC weight fraction.

Fluid density can be assumed to be 0.5 g/cc for gas and 0.8 g/cc for oil. However, when considering multiple fluid types in the rock, fluid density in the case of shale gas can be estimated as shown in Eq.2.18.

$$\rho_f = \rho_g(1 - S_w) + \rho_w S_w \tag{2.18}$$

Where S_w is water saturation, ρ_w is water density, and ρ_g is gas density, in the case of shale oil, ρ_g is replaced with ρ_o (oil density).

Similarly, total porosity can be derived from sonic logs (sonic porosity, SPHI). Such relationship is expressed as follows (Labani & Rezaee, 2015):

$$\emptyset_{sonic} = \frac{(DT - DT_{ma}) + \left(\frac{w_{TOC}}{\rho_{TOC}} \times \rho_b\right) \times (DT_{ma} - DT_{TOC})}{DT_f - DT_{ma}} \tag{2.19}$$

Where $\emptyset_{sonic}$ is the total porosity derived from sonic data (SPHI), DT is rock transit time (us/ft), DT_{ma} is matrix transit time (us/ft), typical values are 55.5 us/ft for quartz, 47.5 us/ft for calcite, and 43.5 us/ft for dolomite (*Porosity Logging*), DT_f is fluid transit time (us/ft), and DT_{TOC} is kerogen transit time (us/ft), transit time of kerogen in coal is around 120 us/ft.

Another measurement is neutron log, which is a downhole log that measures porosity (NPHI). In fact, it is a direct measurement of hydrogen in the formation. Since hydrogen is typically abundant in pore spaces that are filled with water, oil, or gas, hydrogen measurement provides a direct indication of porosity. In shales, however, the relationship is not quite straight forward as hydrogen occurs in multiple other places, like in clay minerals, organic matter, and water/hydrocarbon in the formation (Labani & Rezaee, 2015).

This entails that NPHI reading can increase due to an increase of clay minerals, or it can decrease due to the increase of gas (gas has lower HI). It is also noted that NPHI generally decreases with the increase of the thermal maturity of shale gas. Thus, NPHI reading in shale can suggest misleading interpretation if analyzed independently. Alternatively, analysis of all available logs, such as gamma ray, resistivity, and density should provide a better understanding of the behaviour of NPHI log (Labani & Rezaee, 2015).

In this study, density porosity (DPHI) was mainly utilized for total porosity estimations, Eq.2.17. In wells where sonic logs are available, sonic porosity (SPHI) was also estimated and then compared to the DPHI results. As for neutron porosity, it was utilized alongside the calculated porosity in the non-shaly intervals of the Goldwyer, as it will be discussed in further details in Chapter 3.

2.6 Brittleness

It is a measure of the ability for a rock to fracture and is commonly expressed in brittleness index. It is a function of multiple and complex factors; lithology, mineral composition, TOC, effective stress, reservoir temperature, diagenesis, porosity, thermal maturity, and fluid type (Wang & Gale, 2009; Labani & Rezaee, 2015). According to Jarvie et al. (2007), brittleness of a rock is primarily related to mineralogy. For example, the variable contents of quartz, clay, and carbonate in the Barnett Shale result in variable brittleness and hence variable fracture gradient of the source rock interval.

Generally, brittleness in shales increases with the increase of quartz content and decreases (more ductile) with the increase of clay. Carbonate-rich source rocks are usually moderate in brittleness. Thus, brittleness index can be expressed in terms of the mineral composition of a shale rock (Labani & Rezaee, 2015).

$$BI_{mineralogy} = \frac{Quartz}{Quartz + Carbonates + Clays} \times 100 \quad (2.20)$$

$BI_{mineralogy}$ is the brittleness index derived from mineralogy composition.

Those mineralogy compositions can be determined by using different methods; X-ray powder diffraction (XRD), Fourier transform infrared transmission spectroscopy (FTIR), X-ray fluorescence (XRF), energy-dispersive X-ray spectroscopy setting on the scanning electron microscopy (EDS-SEM), or thin section analysis (TS). In general, XRD, FTIR, and XRF are the most common methods of mineral composition analysis in the oil and gas industry (Labani & Rezaee, 2015).

Alternatively, brittleness index can be defined using the geomechanical elastic properties of the source rock. According to Grieser and Bray (2007), the elastic properties of Young's modulus and Poisson's ratio are key geomechanical parameters and are used to identify the brittle/ductile intervals of a shale source rock. Figure 2.6 is a cross-plot of the two parameters showing brittle and ductile areas.

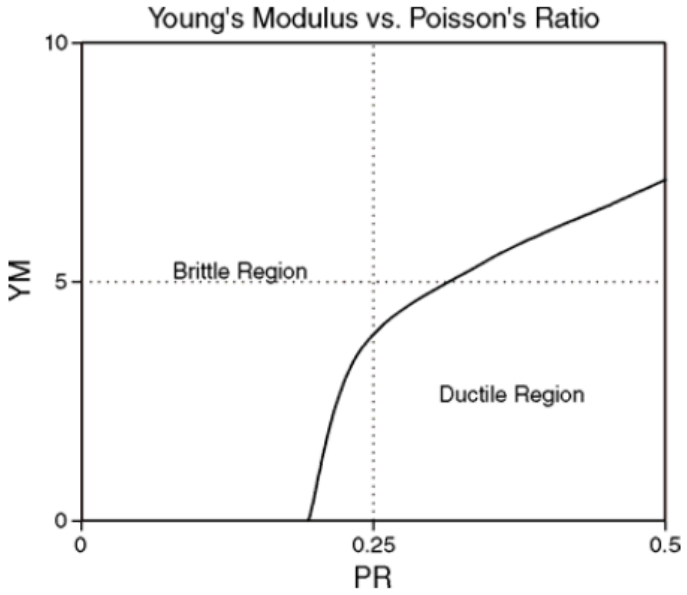

Figure 2.6 Young's modulus and Poisson's ratio cross-plot indicating brittle and ductile areas (Grieser & Bray, 2007).

Whenever a hydraulic stimulation is required for commercial production, brittle areas are preferable to frac into as they are prone to instigate a larger and more complex fracture geometry than those of ductile nature. Figure 2.7 illustrates the difference of frac geometry depending on the brittleness of the rock interval and the values of Young's modulus and Poisson's ratio. A brittle interval would have high Young's modulus and low Poisson's ratio values (Waters et al., 2011).

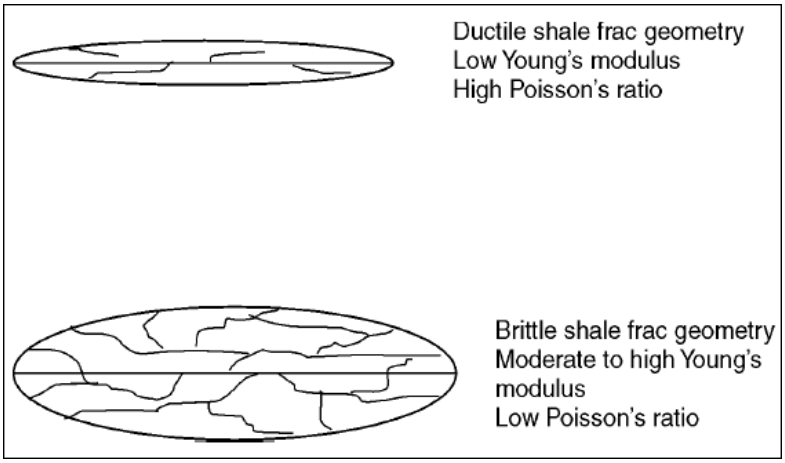

Figure 2.7 Frac geometry differences in brittle and ductile rock intervals (Grieser & Bray, 2007).

In order to determine the brittleness index using this method. Young's modulus and Poisson's ratio need to be calculated. They can be estimated using the compressional and shear velocities as follows (Rickman et al., 2008):

$$E = \frac{\rho V_s^2 \left(3V_p^2 - 4V_s^2\right)}{V_p^2 - V_s^2} \tag{2.21}$$

$$\nu = \frac{V_p^2 - 2V_s^2}{2\left(V_p^2 - V_s^2\right)} \tag{2.22}$$

Where E is Young's modulus, ρ is density, ν is Poisson's ratio, V_p is compressional velocity, and V_s is shear velocity.

In order to implement E and ν for the calculation of the brittleness index (BI), we first need to normalize those parameters (Grieser & Bray, 2007; Labani & Rezaee, 2015).

$$E_{brittle} = \frac{E - E_{min}}{E_{max} - E_{min}} \tag{2.23}$$

$$\nu_{brittle} = \frac{\nu - \nu_{max}}{\nu_{min} - \nu_{max}} \tag{2.24}$$

Where E_{min} is the minimum value of Young's modulus in the interval of interest, E_{max} is the maximum value of Young's modulus in the interval of interest, ν_{min} is the minimum value of Poisson's Ratio in the interval of interest, and ν_{max} is the maximum value of Poisson's Ratio in the interval of interest.

With the normalization of E and ν, the brittleness index (BI) is defined to be the average of these two values (Grieser & Bray, 2007; Labani & Rezaee, 2015).

$$BI_{sonic} = \frac{E_{brittle} + \nu_{brittle}}{2} \times 100 \tag{2.25}$$

BI_{sonic} is the brittleness index derived from sonic.

This approach is dependent on the sonic well data, of both compressional and shear velocities. In many instances, shear velocity is not available in the well data. Therefore, shear wave velocity is typically estimated from compressional wave velocity. Castagna et al. (1985) derived an empirical linear relationship between V_s and V_p. This relationship was derived from worldwide data and became known as the mudrock equation or the ARCO mudrock line (Castagna et al., 1985; Royle & Bezdan, 2001; Labani & Rezaee, 2015).

$$V_s = 0.862V_p - 1.172 \quad (2.26)$$

Both V_p and V_s are in km/s.

Similarly, Krief et al. (1990) defined another relationship between V_s and V_p (Royle & Bezdan, 2001).

$$V_p^2 = aV_s^2 + b \quad (2.27)$$

V_p and V_s are in km/s.

Both a and b are constants that vary depending on the lithology and the hosted fluid type of the rock. Figure 2.8 shows some linear relationship changes based on lithology in a water-wet rock as illustrated by Krief et al. (1990).

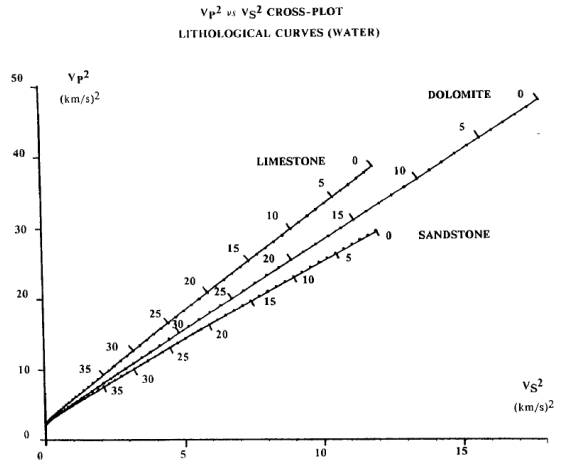

Figure 2.8 A cross-plot of V_p^2 vs. V_s^2 and the corresponding relationship based on lithology, in water wet rock (Krief et al., 1990).

Chapter 3. Property Estimation Results

3.1 TOC Estimation

3.1.1 Schmoker and $\Delta logR$ Methods

There are five key wells in the Barbwire Terrace; Acacia 2, Barbwire 1, Dodonea 1, Percival 1, and Solanum 1, all of which have TOC measurements from Rock-Eval pyrolysis and density logs covering the Goldwyer Formation. In a typical source rock, density logs are most sensitive to variations in TOC content. Hence, deriving TOC logs from density is common practice. A map showing the key well distribution of the Barbwire Terrace can be seen in Figure 3.1. Additionally, a cross section of those key wells showing some of their main logs along the Goldwyer Formation is in Figure 3.2.

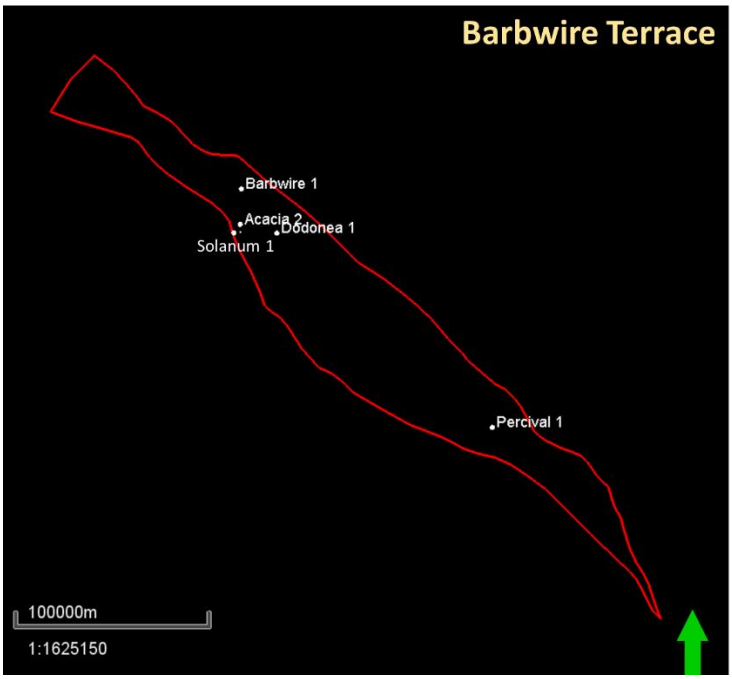

Figure 3.1 A map shows the boundary of the Barbwire Terrace and its key wells.

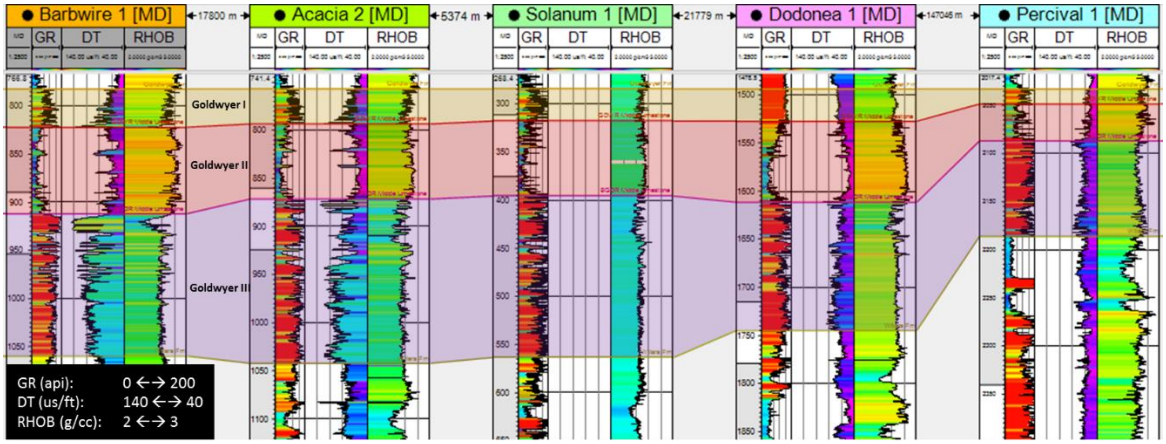

Figure 3.2 A cross section of all five key wells in the Barbwire Terrace, dispalying gamma-ray, sonic, and density logs.

Equation 2.6 is a Schmoker linear regression between TOC and density that was used to estimate TOC for the Barbwire Terrace wells.

TOC was also estimated using ($\Delta logR$) method of Passey et al. (1990). This is a slightly more complicated approach that requires deep resistivity and P-sonic logs. It also needs maturity information of R_o or T_{max} data. Four out of the five key wells in the Barbwire Terrace have the necessary data for TOC to be estimated from the $\Delta logR$ method.

Calculated values of both methods overestimate TOC when validated against TOC measurements from Rock-Eval. This misfit is clearly observed in Figure 3.3, a cross-plot between all estimated TOC values of both methods against TOC measurements from Rock-Eval. Figure 3.4 shows a cross section of two wells emphasizing the misfit caused when using the pre-defined TOC estimation methods.

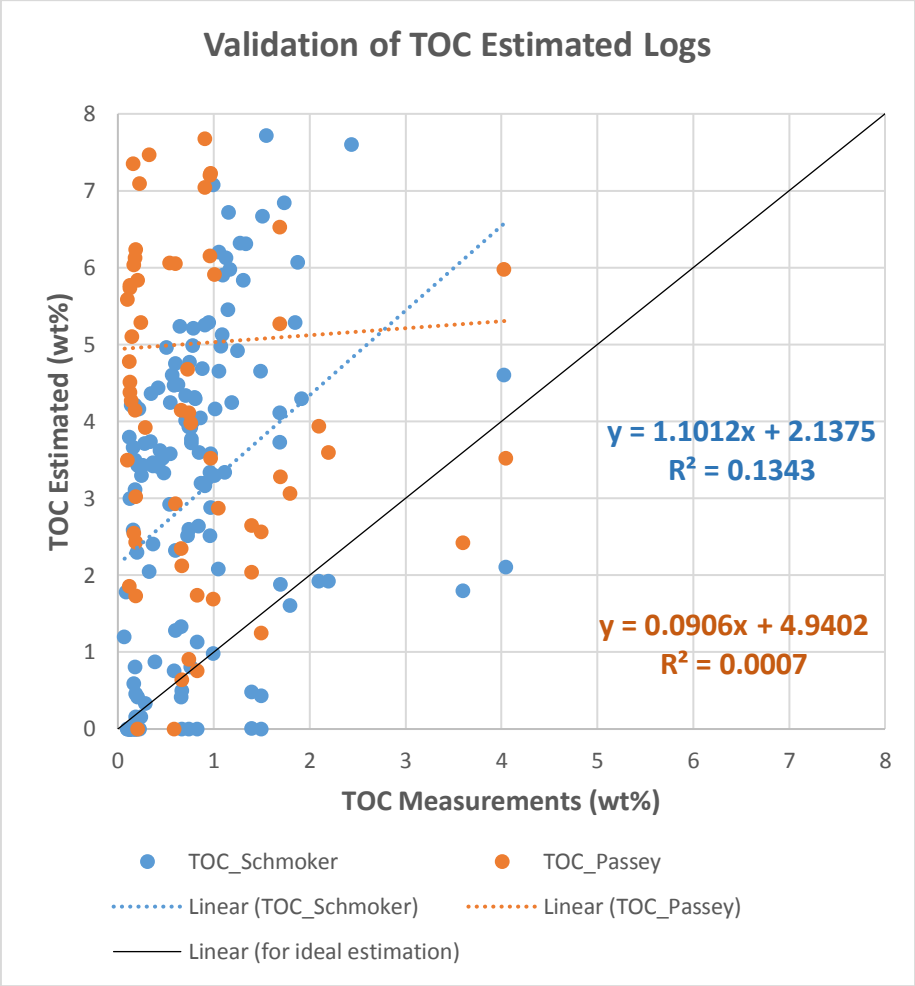

Figure 3.3 A cross-plot showing TOC estimated values from all wells in the Barbwire Terrace plotted against TOC measurements. Both methods overestimate TOC.

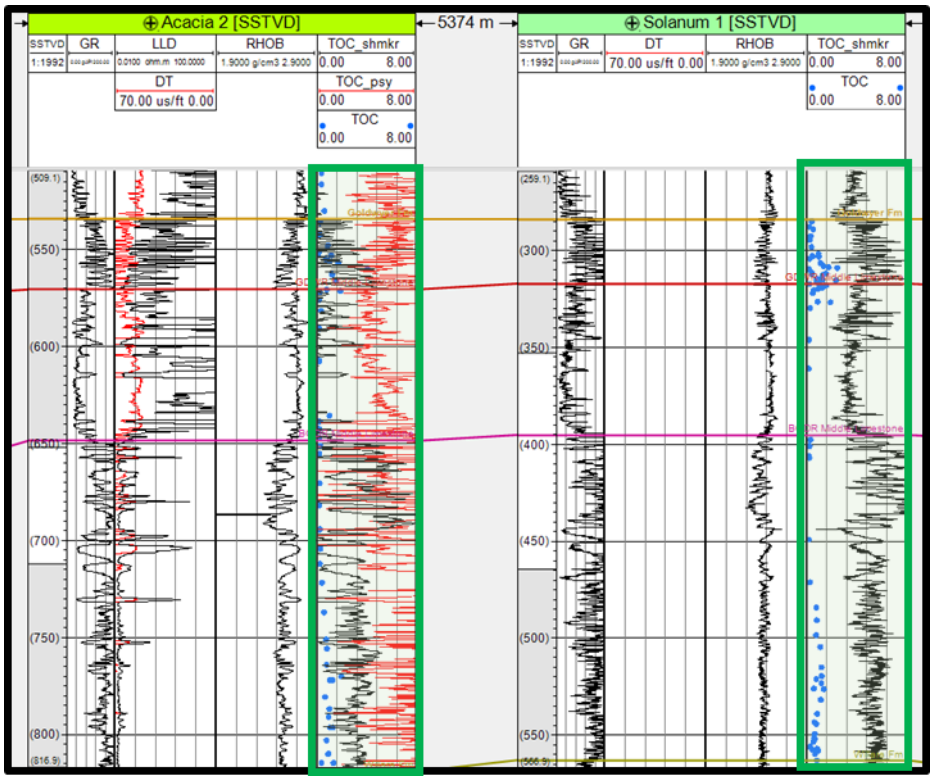

Figure 3.4 Overestimating TOC-Schmoker (black) and TOC-Passey (red) for wells Acacia 2 and Solanum 1. Blue sloid circles are measures of TOC values.

It is noteworthy that applying $\Delta logR$ method has been suitable in other parts of the Canning Basin (H. Yu et al., 2017). This method has yielded acceptable TOC values in some areas of the Goldwyer Formation. However, such results mainly require manipulation of different $\Delta logR$ parameters, which does not necessarily have any scientific basis. For example, available maturity data are not analysed and interpolated. They are often disregarded and simple manipulation of LOM is carried out instead. This simply entails changing the value of LOM for the whole section until the resultant log agrees the most with the TOC measurements. Such manipulations are not necessarily incorrect approaches, but they are not usually backed by sufficient scientific reasoning. For the purpose of this study, it was decided to prioritize exploring other TOC estimation options over the parameters manipulation of the pre-defined methods to deliver an adequate TOC solution of the Goldwyer Formation in the Barbwire Terrace.

3.1.2 Single and Multivariate Regressions

With the pre-defined TOC methods not providing good estimates for the wells in the Barbwire Terrace, using local well data to derive TOC relationships, all in terms of wt%, has become more warranted. Multiple approaches were used, starting from a simple linear regression between Rock-Eval TOC measurements and density (RHOB). This can also be considered as adjusting Schmoker method parameters by utilizing data from the Goldwyer Formation in the Barbwire Terrace. Looking into the Rock-Eval TOC data, measurements were mainly taken from cuttings samples. As a result, depth of those samples cannot be exactly identified. It is very likely that those TOC points are not plotted against their correct corresponding densities. Depth values were edited based on the TOC values and density responses within a range of 3 m (~10 ft), a standard range of error for depths of cutting samples. This depth matching exercise has substantially improved the correlation of TOC and density (Figure 3.5).

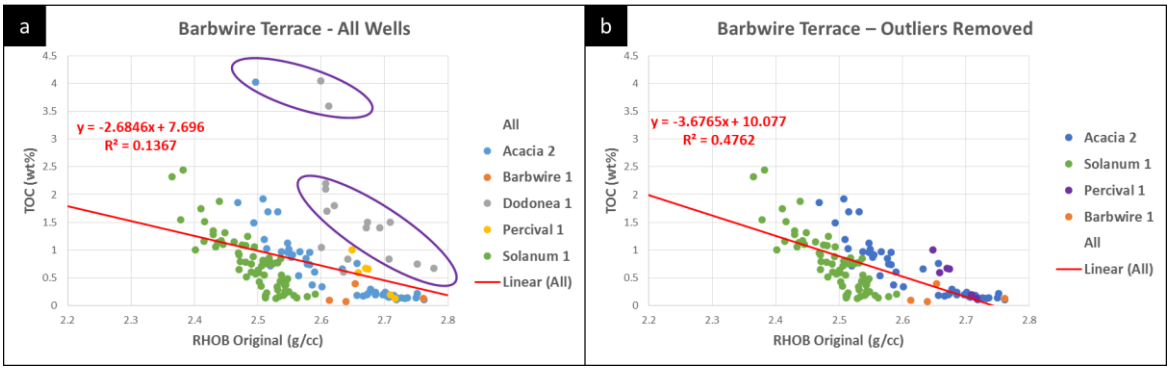

Figure 3.5 (a) TOC vs. RHOB for all wells in the Barbwire Terrace, after depth matching TOC measurements with density. (b) TOC vs. RHOB after depth matching and removing outliers.

TOC data points of Dodonea 1 show different trend and therefore they were treated as outliers and removed from the TOC-Density relationship of the Barbwire Terrace. Goldwyer thickness in this well is about 250 m, whereas all its 16 TOC data points were taken from a range of less than 15 m. TOC values are highly variable (from 0.6% to 4 %) with small density variations. The quality of those measurements is somewhat questionable. Nevertheless, one likely explanation of those anomalous data points is that they all lie in compositionally different facies zone, the generally more calcareous middle limestone zone of the Goldwyer section, and hence, showing different TOC-density trend. In fact, a further look into Figure 3.5a shows that data points of each well could have their own linear trend. This emphasizes the lithological variations of the Goldwyer across those wells. The Goldwyer Formation of Acacia 2 is mainly argillaceous limestone with interbedded calcareous clay siltstones (Watson & Derrington, 1982). Solanum 1 has slightly different Goldwyer section, where it is mostly dolomitic limestone with calcareous siltstone interbeds (France & Scibiarski, 1984). The Goldwyer section of Barbwire 1, however, is more siltstone dominant with dolomitic limestone strata (Young, 1972). Finally, Percival 1 has a Goldwyer interval that is mostly argillaceous dolomite (France, 1986; WAPIMS, 2017).

Nonetheless, TOC was derived from density (RHOB) using the relationship between the two variables of data points of all four wells as can be seen in Figure 3.5b.

$$TOC = -3.68\,RHOB + 10.08 \tag{3.1}$$

Once this single regression between TOC and RHOB was established (Eq.3.1), multivariate regressions were also introduced to analyze any further improvement in TOC estimation. This included deriving TOC from gamma-ray (GR) and density (RHOB), (Eq.3.2)

$$TOC = 0.00435\,GR - 2.469\,RHOB + 6.48 \tag{3.2}$$

TOC was also derived from gamma-ray (GR), density (RHOB), and neutron porosity (NPHI). Eq.3.3 shows this derivation.

$$TOC = 0.00605\,GR - 3.219\,RHOB - 1.333\,NPHI + 8.45 \tag{3.3}$$

Furthermore, other properties and different combinations were used to estimate TOC. Table 3.1 shows an extensive list of derived TOC equations, where the R^2 associated with the cross-plot of calculated TOC versus measured TOC represents the estimated confidence of each approach.

Table 3.1 List of TOC equations derived from different properties, each validated with measured TOC from Rock-Eval.

		Derivation		Validation	
TOC Derived From	**Zones**	**Equation**	**R^2**	**Trendline Eq. of TOC_calc vs. TOC_measured**	**R^2**
RHOB	All	TOC=-3.6765*RHOB+10.077	0.4762	TOC_RHOB=0.4794*TOC+0.3487	0.4827
GR, RHOB	All	TOC=6.48+0.004355*GR-2.469*RHOB	0.4942	TOC_GR-RHOB=0.6132*TOC+0.2852	0.5879
V_{sh}, RHOB	All	TOC=6.52+0.968*V_{sh}-2.457*RHOB	0.5013	TOC_Vsh-RHOB=0.5276*TOC+0.3161	0.5303
GR, RHOB, NPHI	All	TOC=5.88+0.00484*GR-2.257*RHOB+0.05695*NPHI	0.5032	TOC_GR-RHOB-NPHI=0.6317*TOC+0.2825	0.5862
GR, RHOB, NPHI	All	TOC=8.45+0.006047*GR-3.219*RHOB-1.333*NPHI	0.5264	TOC_GR-RHOB-NPHI1=1.0274*TOC+0.5091	0.5496
GR, RHOB, NPHI	1	TOC=7.85+0.00770*GR-3.12*RHOB-0.03*NPHI	0.5646	TOC_GR-RHOB-NPHI_3zns=0.6865*TOC+0.0929	0.5359
	2	TOC=8.00+0.00473*GR-2.972*RHOB-1.22*NPHI	0.6921		
	3	TOC=3.84+0.00237*GR-1.449*RHOB+0.627*NPHI	0.517		
GR, RHOB	1	TOC=7.96+0.00763*GR-3.165*RHOB	0.5678	TOC_GR-RHOB_3zns=0.726*TOC+0.2043	0.6687
	2	TOC=6.18+0.00345*GR-2.284*RHOB	0.6851		
	3	TOC=6.09+0.00288*GR-2.300*RHOB	0.5026		
RHOB	1	TOC=-4.4152*RHOB+12.077	0.496	TOC_RHOB_3zns=0.5276*TOC+0.3161	0.5303
	2	TOC=-3.3486*RHOB+9.2515	0.5781		
	3	TOC=-3.3002*RHOB+9.0143	0.433		

To further improve TOC estimation, the Goldwyer section was divided into three zones: upper, middle, and lower. The zoning was interpreted using log responses of common properties, such as gamma-ray, sonic, and density. Each zone had its own TOC estimation. The three-zone and the one-zone approaches were then calculated for those different combinations of multivariate regressions (Table 3.1).

Figure 3.6 reiterates the TOC validation for all estimations that involved NPHI. Whereas the validation of estimated TOC from just GR and RHOB is illustrated in Figure 3.7. The best approach was identified to be the TOC estimated from RHOB and GR for 3 zones in the Goldwyer (Eq.3.4, 3.5, & 3.6), which when cross-plotted against TOC values gives the highest R^2 (lowest error), line slope closest to one, and has the lowest y-intercept value, closest to zero (Figure 3.7). The one-zone approach of derived TOC log from the same properties, GR and RHOB, is the second best estimate.

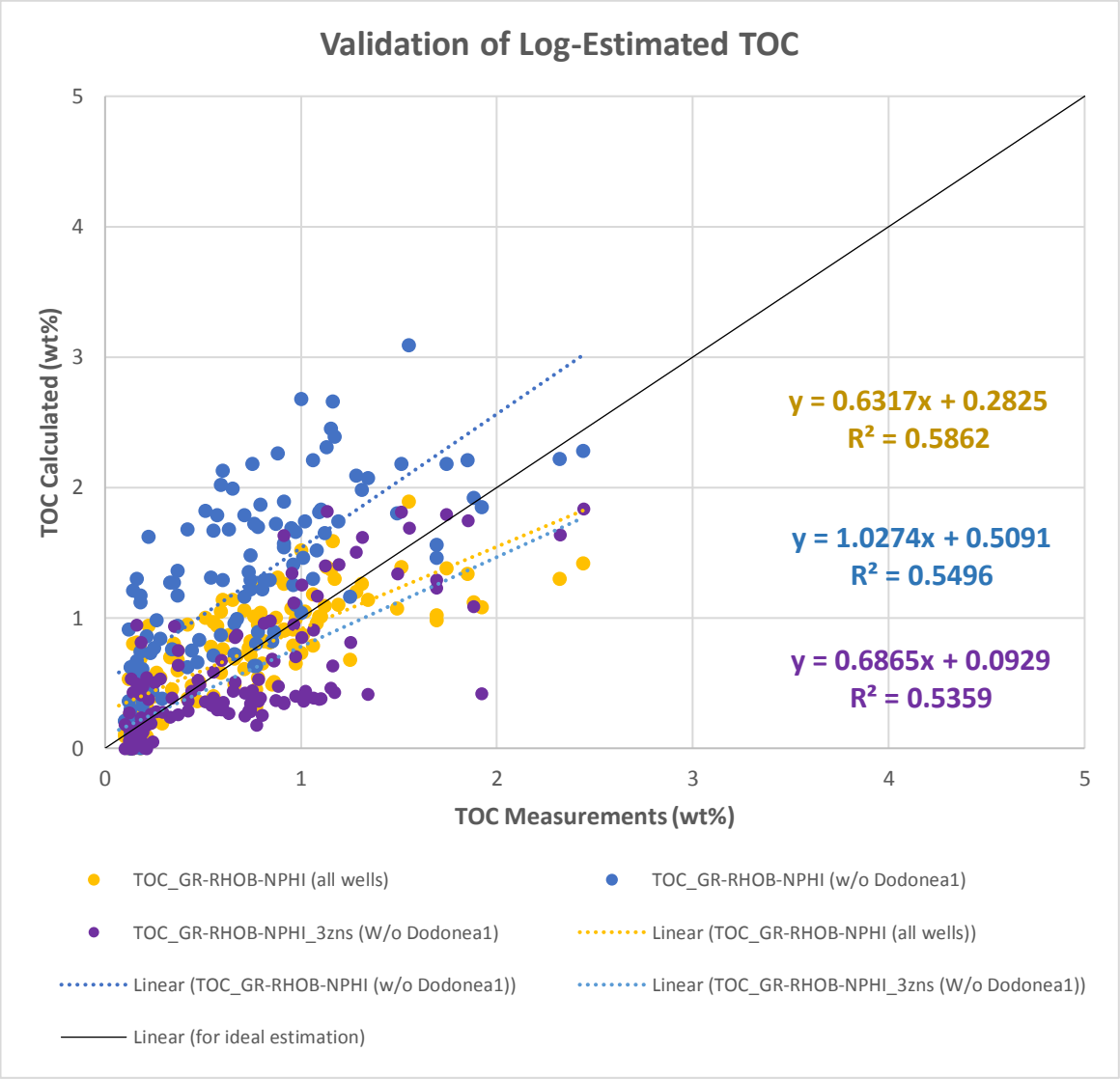

Figure 3.6 TOC calculated from different regressions cross-plotted against measured TOC from Rock-Eval data. TOC values were estimated using gamma-ray, density, and neutron porosity.

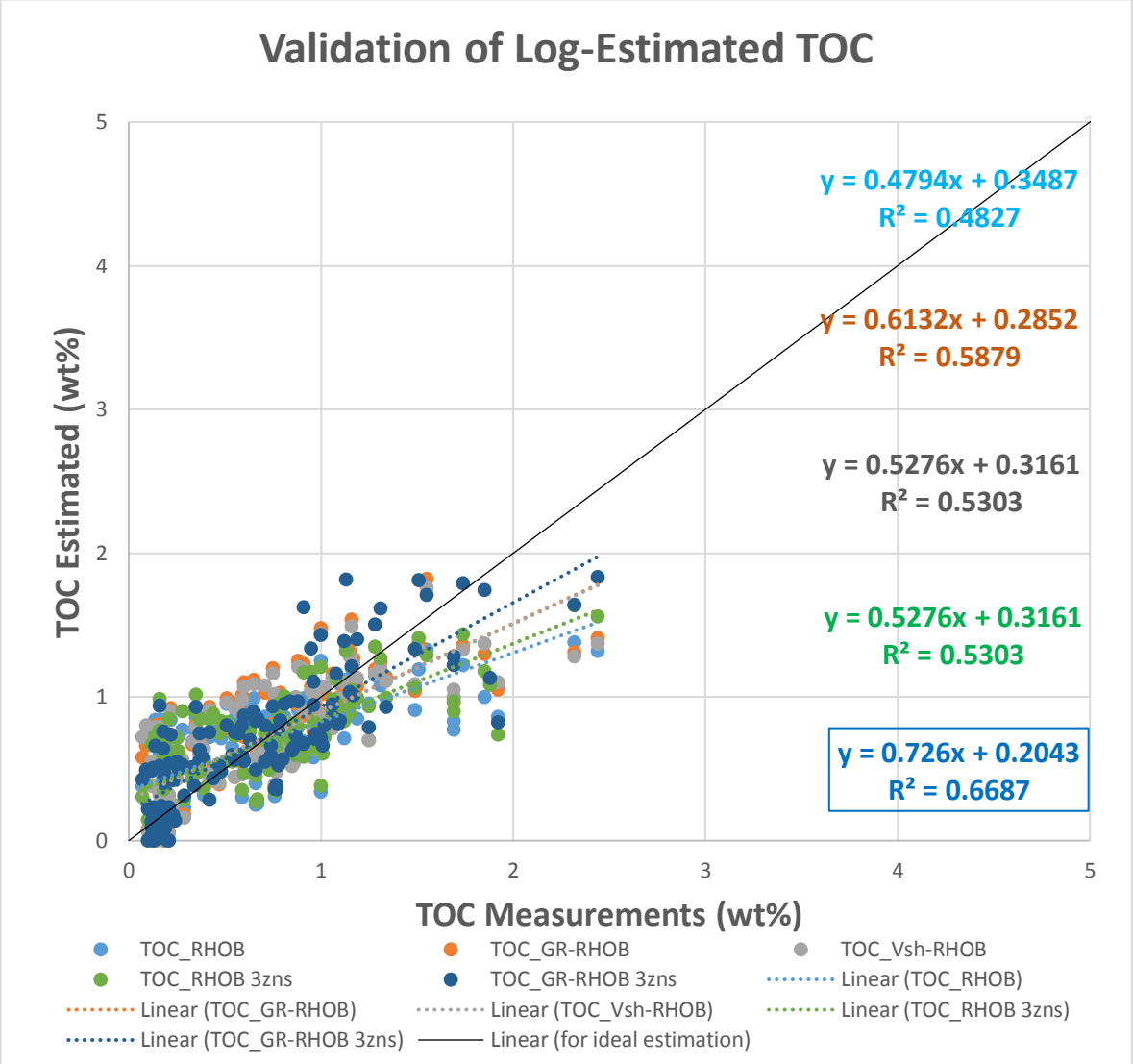

Figure 3.7 Estimated TOC values from different approaches are cross-plotted against TOC measurements from Rock-Eval. The best approach is the one that has a trend line of highest correlation (highest R^2), line slope closest to one, and y-intercept closest to zero.

$$TOC_{zone1} = 0.0076 \cdot GR - 3.165 \cdot RHOB + 7.96 \quad (3.4)$$

$$TOC_{zone2} = 0.0034 \cdot GR - 2.28 \cdot RHOB + 6.18 \quad (3.5)$$

$$TOC_{zone3} = 0.0029 \cdot GR - 2.3 \cdot RHOB + 6.09 \quad (3.6)$$

Equations 3.4, 3.5, and 3.6 were derived from density (RHOB) and gamma-ray (GR), one equation for each Goldwyer zone. These equations were applied to all Barbwire Terrace wells to estimate TOC content of the Goldwyer Formation (Figure 3.8).

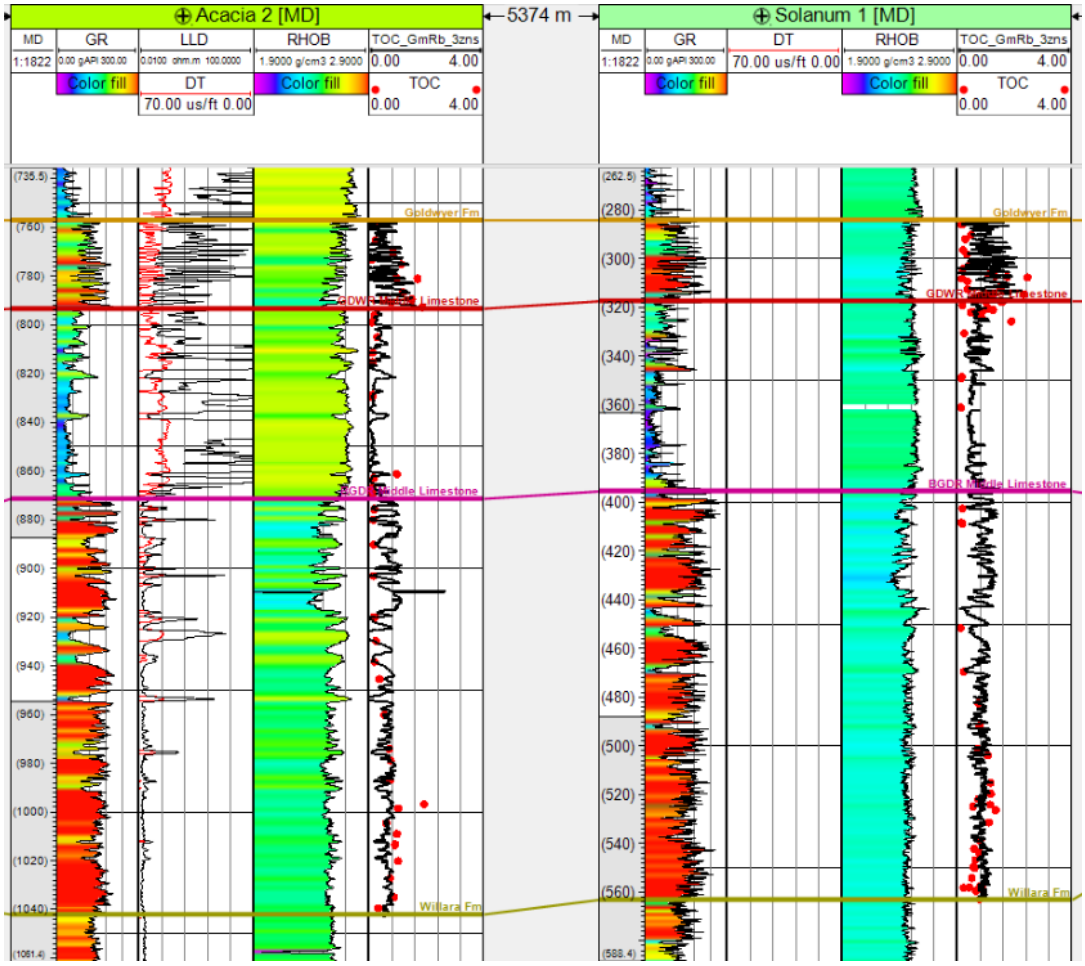

Figure 3.8 TOC log derived from density and gamma-ray for each Goldwyer zone. Good correlation between TOC log and measured TOC points. Wells Acacia 2 and Solanum 1 are shown here as examples.

3.1.3 Global Solution and Application

Further analysis of the TOC estimation was carried out, where transit time sonic log was introduced to the TOC solutions, which provided a superior estimate that tends to work globally. The reason this approach was not implemented in the Barbwire Terrace is that not all wells in the terrace have sonic data across the Goldwyer. Deriving TOC from gamma-ray and density provides sufficient TOC estimates for more wells in the Barbwire Terrace.

3.1.3.1 Further TOC Solutions

The GR-RHOB derived TOC equations provided the best approach for TOC estimation in the Barbwire Terrace. However, when looking beyond the Goldwyer Formation and assessing the reliability of using this relationship to different shale types outside the Canning Basin, something might be quite missing. Gamma-ray and density are properties that are mostly representative of lithology. As lithology is a significant factor in shale evaluation, compaction can be just as significant. Practically, we could have two shale units with analogous lithology, and hence, similar RHOB and GR values but with different TOC values as they have different compaction/burial history.

For any TOC relationship, factors of both lithology and compaction for different shales should be represented for it to be globally more reliable. Utilizing multi-regression analysis we have generated such a relationship using compressional sonic (DT) as the compaction property of the same database used in previous regressions, Eq.3.7.

$$TOC = 0.0026\,GR - 8.22\,RHOB - 0.0226\,DT + 23.57 \quad (3.7)$$

The resulted TOC log showed excellent correlation when cross-plotted against TOC measurements and overlayed in a well section along with other TOC log and measurement points, Figure 3.9 and Figure 3.10, respectively. Estimated R^2 of this equation is 0.82, suggesting that there is 82% confidence in this method for the estimation of TOC in the Barbwire Terrace. In other words, estimated error is 18%. Nevertheless, one well had to be dropped from the derivation as it had no sonic log transit time data across the Goldwyer Formation. Consequently, the apparent higher correlation can partially be regarded to the fewer data used. However, this is not the only reason for this correlation enhancement. We believe that the introduction of the compaction term to the equation is the main reason for the observed uplift, as we have now implemented both lithology and compaction information in the TOC estimation approach. Furthermore, the equation of derived-TOC from GR, RHOB, and DT (Eq.3.7) was applied to wells outside the Barbwire Terrace for further validation. Those wells are Crystal Creek 1 and Hilltop 1 of Mowla Terrace and Broom Platform, respectively. Derived TOC logs show good correlation with TOC data points (Figure 3.11).

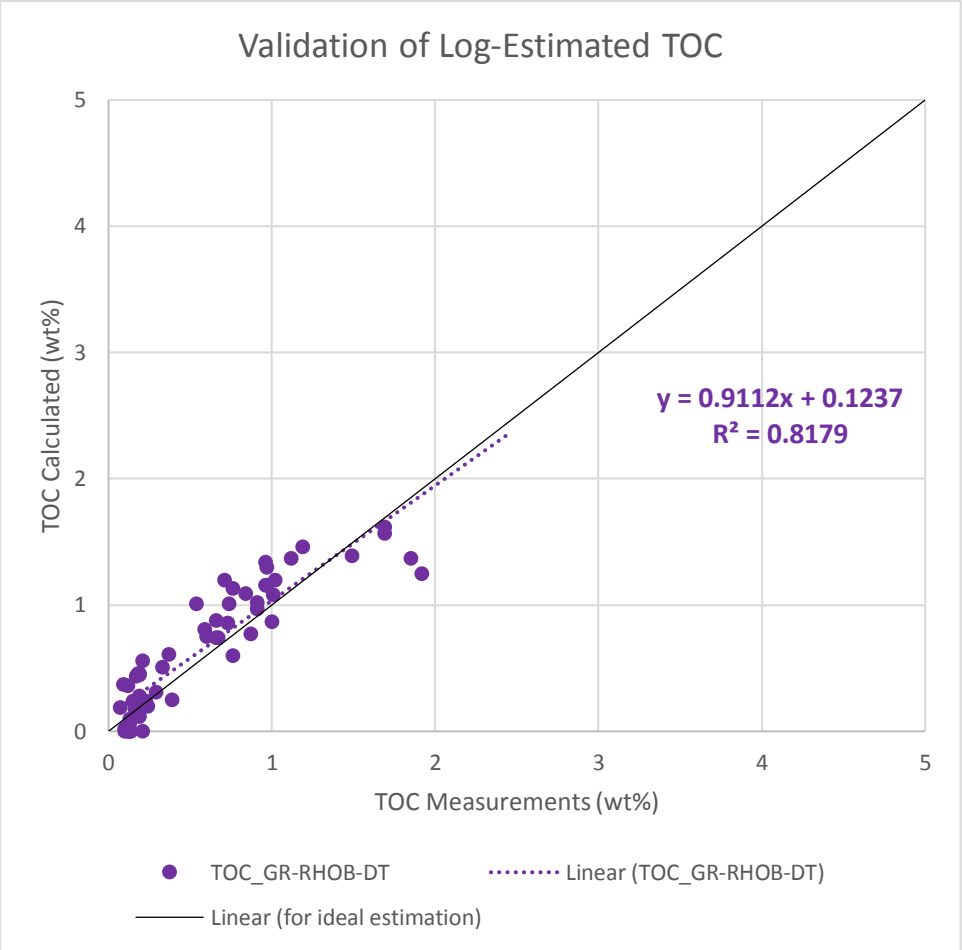

Figure 3.9 Estimated TOC values from GR, RHOB, & DT are cross-plotted against TOC measurements from Rock-Eval. This TOC estimation method would be best as the trend line would have highest correlation (highest R^2), line slope closest to one, and y-intercept closest to zero.

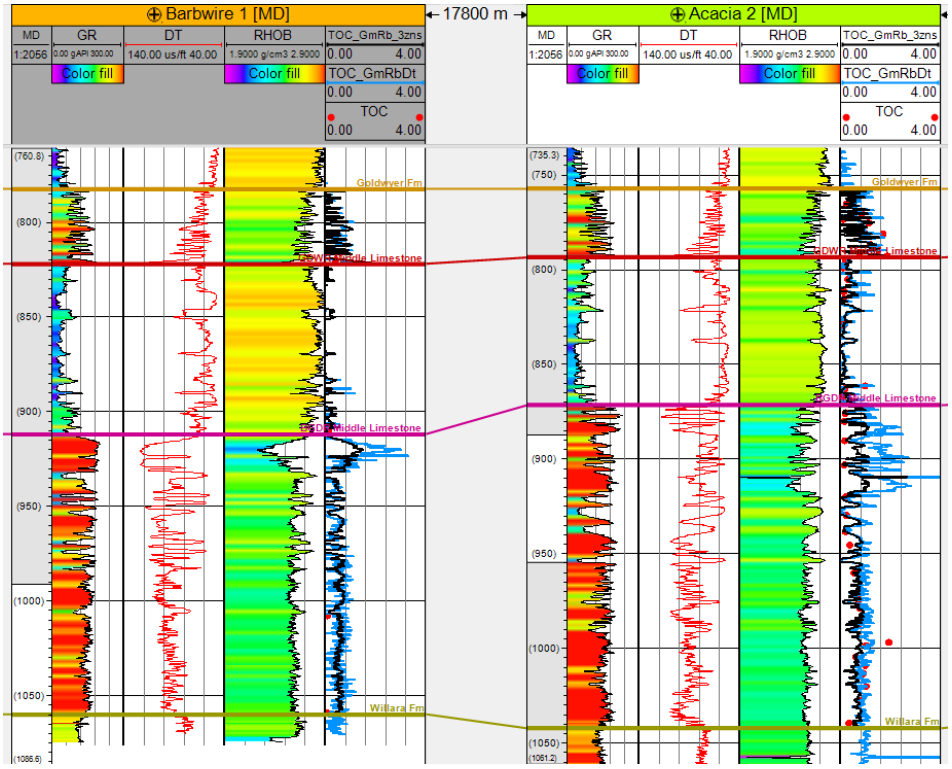

Figure 3.10 See track to the right of both wells. TOC log derived from GR and RHOB for each Goldwyer zone (black curve) overlayed with TOC log derived from GR, RHOB, and DT for the whole Goldwyer as one zone (blue curve). Wells Barbwire 1 and Acacia 2 are shown here as an example.

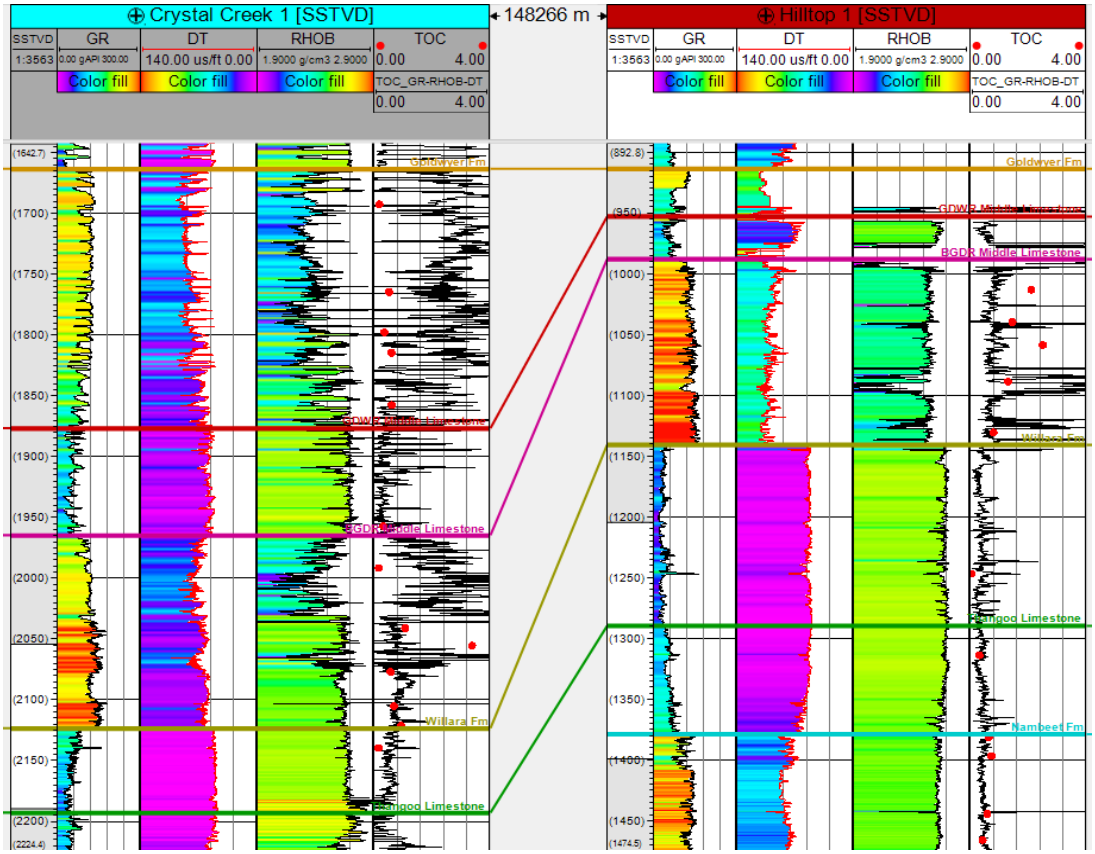

Figure 3.11 TOC logs estimated using the relationship derived from GR, RHOB, and DT to validate the use of this approach outside the study area. Well Crystal Creek 1 of Mowla Terrace and Hilltop 1 of Broome Platform are both shown here.

The improvement in the TOC estimation after adding the compaction term is clearly evident. Such enhancements in the TOC estimation should also be observed when this relationship is applied to shale plays globally. Nonetheless, using a normalized gamma-ray can be more appropriate when applying the equation with the same constants to other shale formations. Consequently, Eq.3.7 can be updated to incorporate V_{sh} instead of GR (Eq.3.8).

$$TOC = 0.679\, V_{sh} - 8.08\, RHOB - 0.025\, DT + 23.35 \tag{3.8}$$

V_{sh}= Volume of shale (normalized gamma-ray)

Alternatively, in shale plays where sufficient data is available, deriving the source rock's own constants can be even more reliable. The objective is to use key data of gamma-ray, density, and sonic transit time for TOC estimations where constants can change whenever appropriate (Eq.3.9).

$$TOC = a \cdot GR + b \cdot RHOB + c \cdot DT + d \tag{3.9}$$

For a specific shale formation, either GR or V_{sh} can be used for TOC estimation. Both equations (Eq.3.10 and Eq.3.9) can be used interchangeably as they would yield almost identical results.

$$TOC = a \cdot V_{sh} + b \cdot RHOB + c \cdot DT + d \tag{3.10}$$

3.1.3.2 Global Shale Application

To further validate the findings of this approach, TOC is estimated for a lacustrine shale outside Australia. This lacustrine source rock had been deposited in fluvial-lacustrine settings during the Late Triassic. Additionally, very high TOC values were measured from core samples of this shale, with TOC values averaging around 4.8%.

Given that a sufficient number of TOC samples are available, TOC was estimated using Eq.3.9. Parameters a, b, c, and d were all derived from this lacustrine shale. For comparison, TOC was also estimated using different approaches, as multiple equations were derived from RHOB, GR, DT, and NPHI. Table 3.2 shows a list of these equations and their estimated parameters.

Table 3.2 A list of TOC equations derived from different properties for the lacustrine shale.

TOC Derived From	Equation	R^2
RHOB	TOC=57.65-21.65*RHOB	0.5067
GR, RHOB	TOC=32.13+0.0208*GR-12.45*RHOB	0.6246
DT, RHOB	TOC=13.88+0.1257*DT-8.37*RHOB	0.6912
GR, RHOB, NPHI	TOC=44.0+0.01618*GR-17.02*RHOB-0.0009*NPHI	0.7036
GR, DT, RHOB	TOC=-8.24+0.01946*GR+0.1206*DT-0.3*RHOB	0.7941

Estimated TOC values were then cross-plotted against TOC measurements to evaluate each estimation approach. TOC derived from Eq.3.9, which uses gamma-ray, sonic transit time and density (GR, DT, & RHOB), once again, shows its superiority over other equations, with estimated R^2 of 0.79 (Figure 3.12). This further confirms that TOC derived from those three properties relatively provides an accurate estimation for TOC. A well cross section of the estimated TOC log can be seen against TOC measured core samples in Figure 3.13.

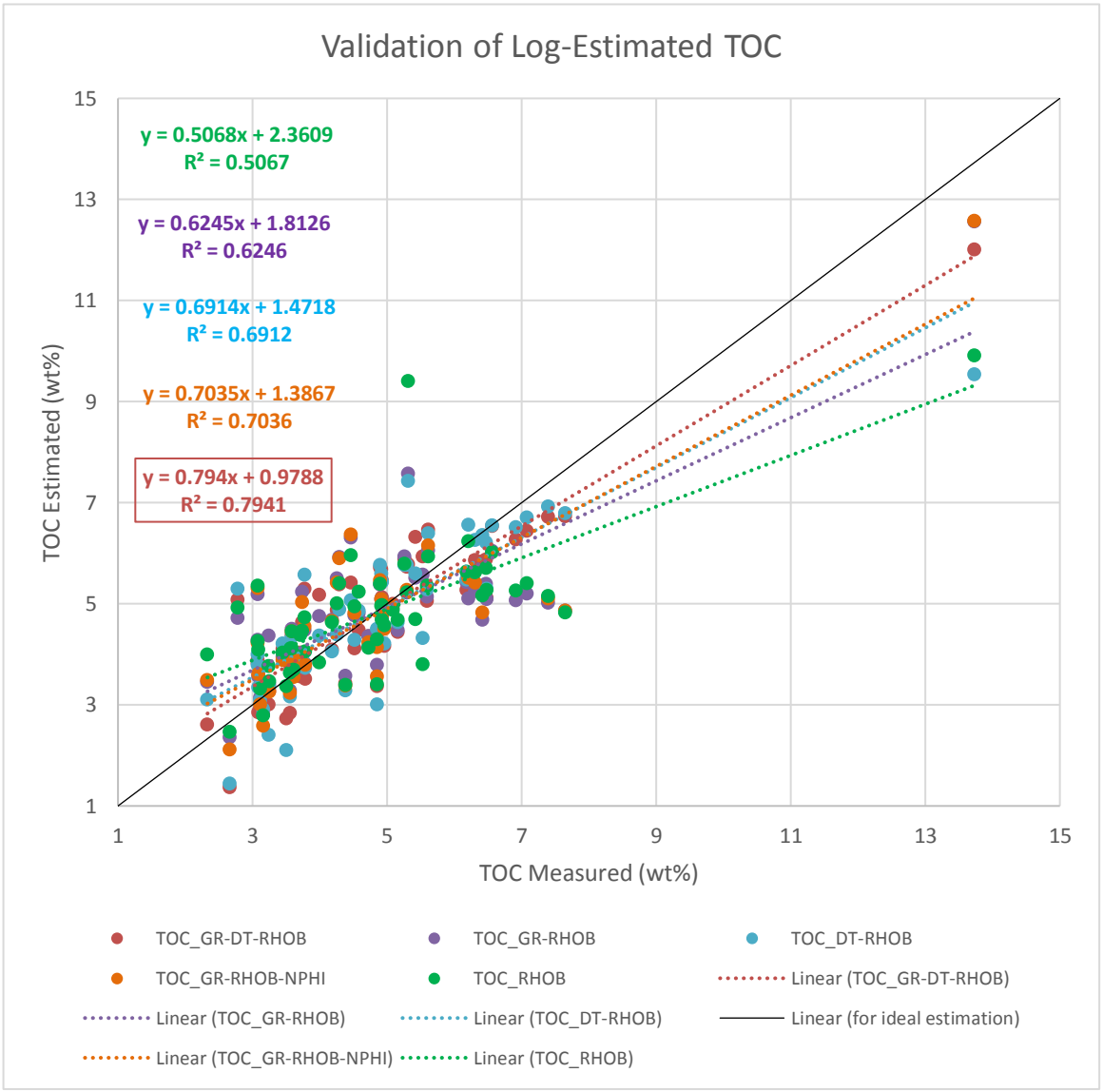

Figure 3.12 Estimated TOC values from different approaches are cross-plotted against TOC core measurements. The best approach is the one that is closest to the solid diagonal black line (TOC_GR-DT-RHOB), which would have a trend line of highest correlation (highest R^2), line slope closest to one, and y-intercept closest to zero.

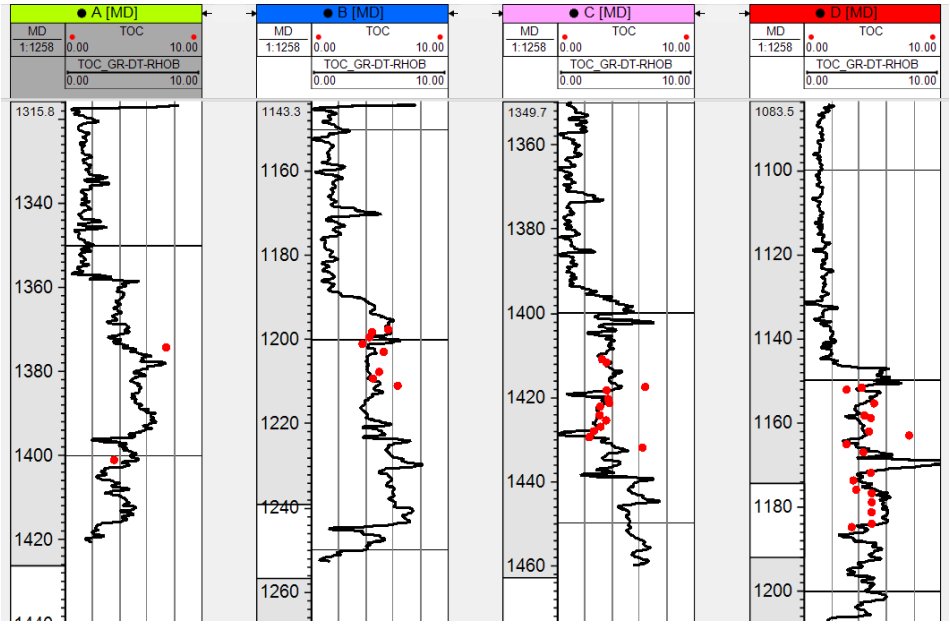

Figure 3.13 A cross-section of four wells showing TOC log derived of the lacustrine source rock from gamma-ray, sonic transit time, and density plotted along with some TOC core measurements.

3.2 Water Saturation

Water saturation estimation uses Eq.2.12 as a simplified form of Archie's equation to calculate saturation for a prospective source rock. The approach solely depends on resistivity log, and hence, water saturation is estimated for all wells with resistivity logs across the Goldwyer Formation. There are four wells in the Barbwire Terrace with resistivity logs covering the whole Goldwyer interval.

Equation 2.12 requires an estimated value of the resistivity of a lean shale. Such a value can be estimated from TOC Rock-Eval measurements and resistivity cross plots. An example of R_o estimation of Acacia 2 can be seen in Figure 3.14. Once R_o is known, water saturation can be estimated using Eq. 2.12. The saturation exponent n is given the value 1.7 for shales as proposed by Luffel and Guidry (1992). R_t is the resistivity log along the Goldwyer interval. The resultant water saturation shows values of generally less than 30% across the whole Goldwyer section of the example well Acacia 2. However, with further analysis, the resultant S_w log quite mimics the TOC log, where S_w increases as TOC increases and vice versa (Figure 3.15). In theory, the relationship between the two properties should be an inverse relationship. As TOC increases, hydrocarbon should consequently increase, which would lead to less water saturated in the rock. Such observation suggests an unreliable estimation of the water saturation.

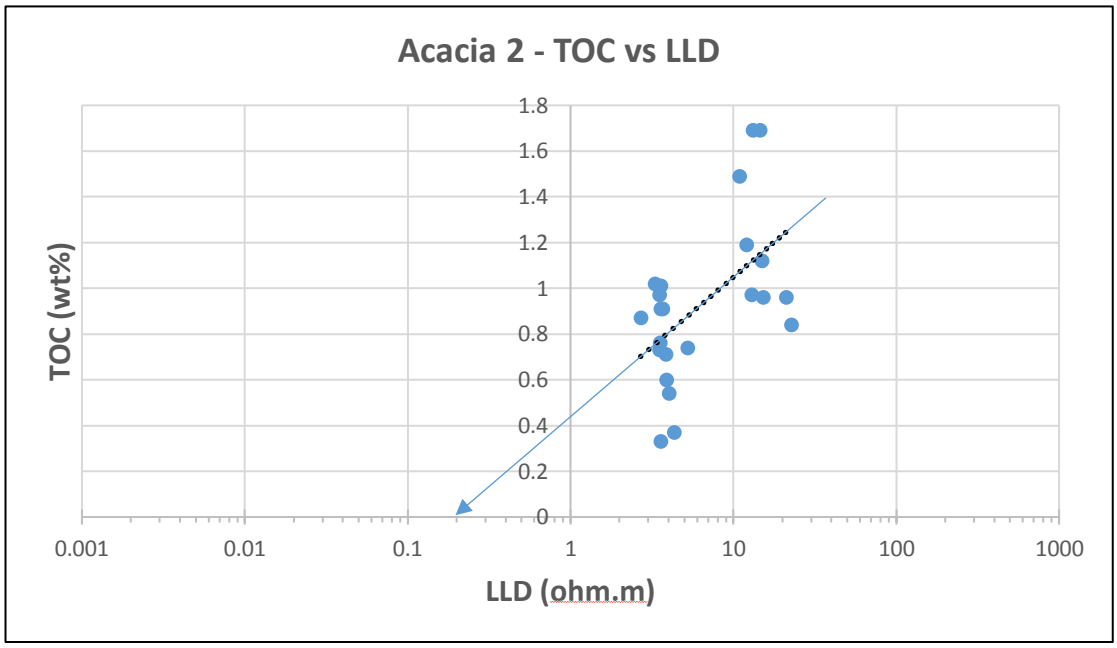

Figure 3.14 TOC-LLD (deep resistivity) cross-plot is used to estimate resistivity of lean shale. Acacia 2 is shown here as an example and estimated R_o = 0.2 Ohm-m. This is the estimated value of resistivity when TOC=0.

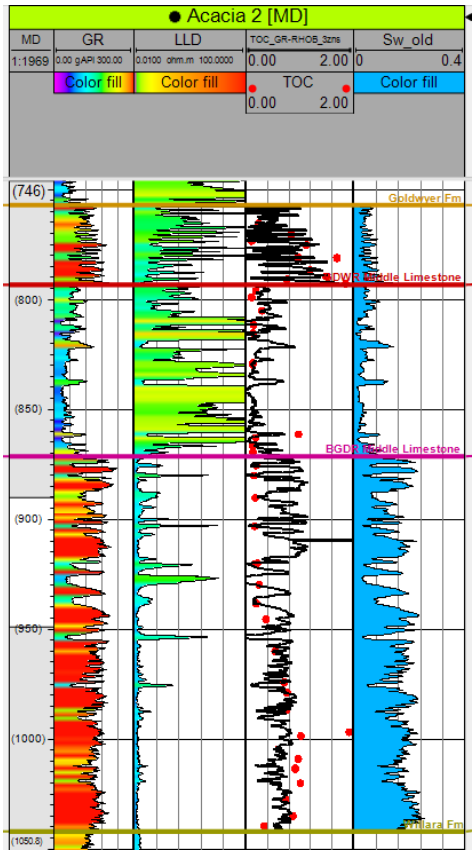

Figure 3.15 Logs TOC and S_w both have the same behaviour, as TOC increases water saturation increases too. This represents a false relationship. Acacia 2 is shown here as an example.

The variations of water depths during the deposition of the Goldwyer Formation from high energy conditions to quiet subtidal shelf or lagoon as noted by Haines (2004), has resulted in alternating facies across the Goldwyer Formation. Lumping those facies altogether and using one R_o value to represent them all has generated unreliable estimations. Alternatively, the Goldwyer Formation was broken down into different facies using the volume of shale log (Eq.3.11) derived from gamma-ray (normalized gamma-ray). Utilized data points were all rock samples that underwent Rock-Eval pyrolysis and have their TOC values measured. For example, the facies breakdown of Acacia 2 and the assignment of R_o for each facies is illustrated in Figure 3.16.

$$V_{SH} = \frac{GR - GR_{min}}{GR_{max} - GR_{min}} \tag{3.11}$$

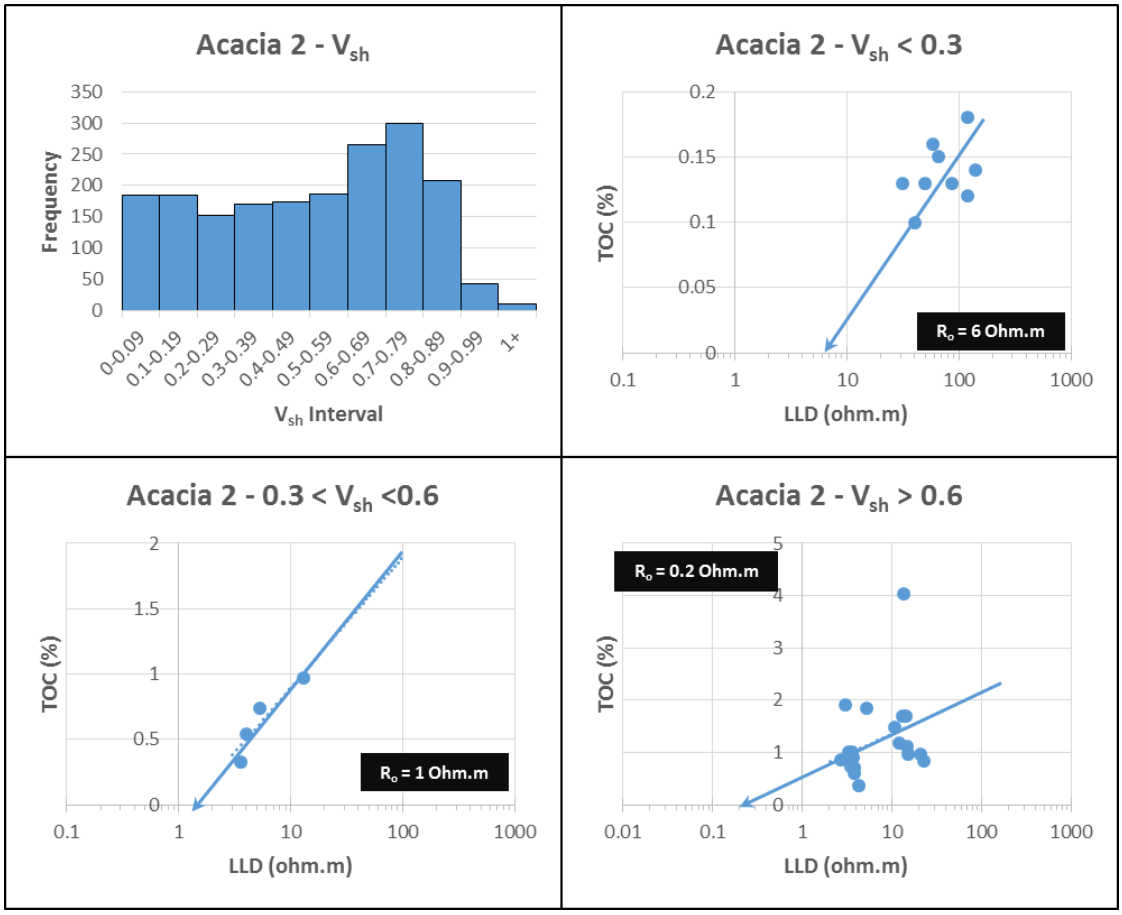

Figure 3.16 In Acacia 2, Goldwyer is broken down into three facies using V_{sh} data. The first facies with the lowest V_{sh} represents the limestone 'dolomitic' intervals. The higher the V_{sh} is, the more shaly that interval gets. Each data point is a rock sample that has its TOC measured from the Rock-Eavl pyrolysis and is plotted against its corresponding deep resistivity value.

Water saturation was then calculated for each facies using the corresponding estimated R_o values. Facies related water saturations were later combined to form S_w log across the whole Goldwyer. Treating each facies individually has improved the water saturation into a more reliable estimation and has eliminated erroneous behaviour that was observed earlier of S_w when compared to TOC log. The newly estimated S_w now accurately corresponds to TOC changes (Figure 3.17). Water saturation decreases as total organic carbon increases, and vice versa.

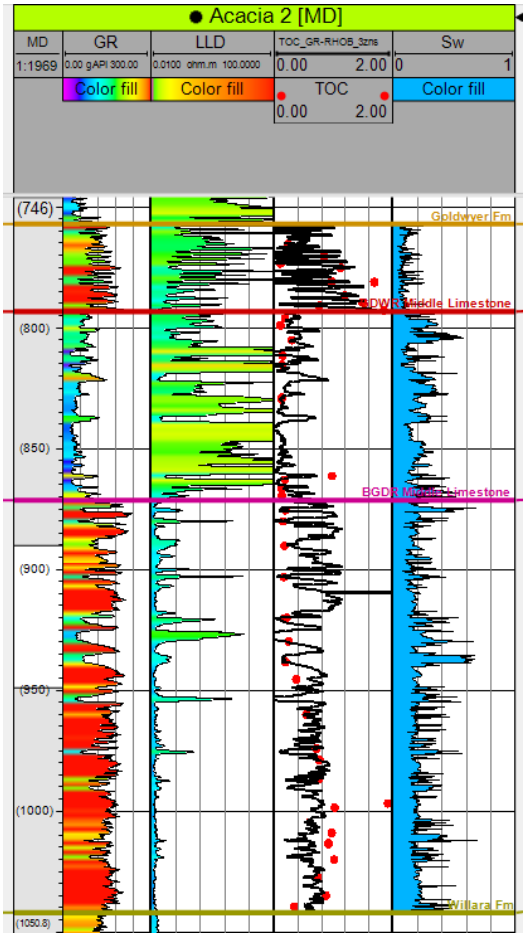

Figure 3.17 Once R_o value was estimated independently for each Goldwyer facies, water saturation accurately corresponds to TOC changes. We can generally observe that as TOC increases, S_w decreases and vice versa. Acacia 2 is shown here as an example.

All other three wells (Dodonea 1, Percival 1, and Solanum 1) went individually through the same process of facies breakdown, individual R_o assignment, and water saturation estimation. The well Barbwire 1 was dropped here because it has no resistivity information across the Goldwyer Formation. It is notable that a test was carried out to seek a more generalized solution for the whole Barbwire Terrace. The aim was to combine data from all four wells. This combined data should then undergo a facies breakdown and R_o value assignment for each facies, the same way it was done for individual wells (Figure 3.16). This R_o value would then be used for all wells within its corresponding facies interval to estimate water saturation. However, the variation of resistivity readings (and resistivity tools, in some cases) of each well across the Goldwyer and the difference in facies breakdown from one well to another have shown cross plots with no obvious trends to estimate R_o with reasonable certainty. Hence, assigning R_o values for each facies type was both more favourable and reliable to be carried out for wells independently.

Nonetheless, the limestone intervals that are predominant in Goldwyer II cannot be considered shaly with the volume of shale that is less than 15%. Therefore, a simplified Archie's equation will not yield reliable saturations. The resistivity of a lean shale (R_o) cannot be estimated from a lean non-shale interval. The full Archie's equation should be applied instead (Eq.2.13). However, identifying the resistivity of formation water is challenging for non-conventional reservoirs as water samples are very difficult to retrieve and water salinity can be variable across the tight rock interval. Hence, no reliable R_w can be utilized for the S_w estimation in Eq.2.13. Since those sections have very low porosities and with effectively zero TOC, they are expected to be fully saturated with water.

Hence, tight limestone intervals with volume shale less than 15% were given water saturation of one, indicating they fully water saturated (Figure 3.18). This volume of shale cut-off was specified based on the well data, where carbonate intervals in the Goldwyer tend to have an overall volume of shale that is less than 15% and zero TOC. Furthermore, this step was only carried out after mud log data and all other available hydrocarbon tests indicated no gas/oil traces are present across such intervals.

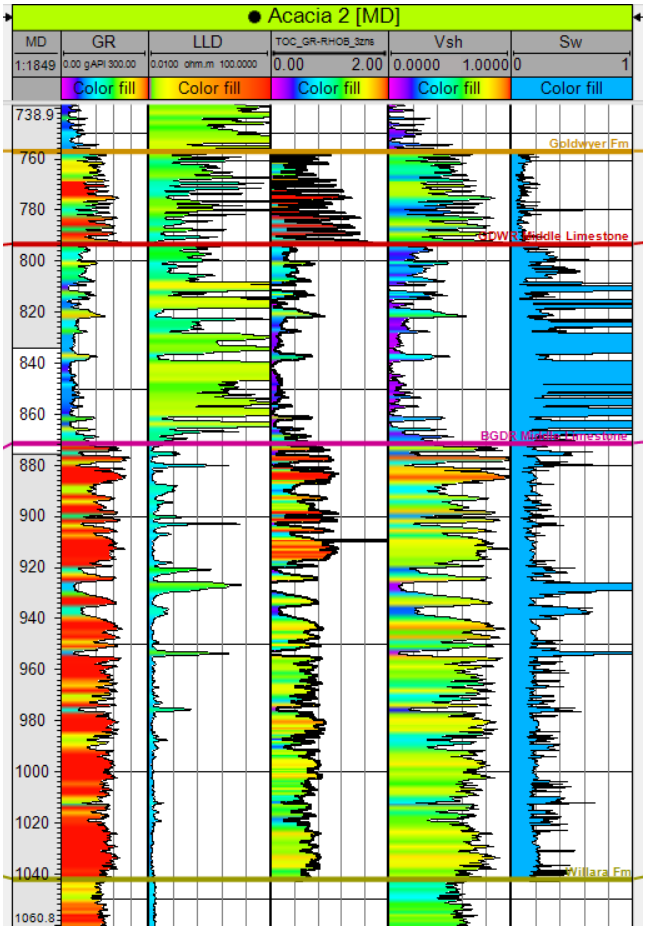

Figure 3.18 Water saturation estimated for the Goldwyer Formation. A simplified Archie's equation is utilized for the estimation, where S_w is assumed to be one in intervals with V_{sh} < 15%.

3.3 Total Porosity

Total porosity (PHIT) can be estimated using density porosity or sonic porosity methods. Both approaches were calculated for wells in the Barbwire Terrace. For density porosity, values were estimated for wells with available density logs across the Goldwyer section. Water saturation and TOC information were also utilized for this porosity estimation, Eq.2.17.

This approach requires assigning values of certain parameters to properly estimate porosity. A value needs to be assigned for the matrix density of the Goldwyer Formation. Goldwyer core analysis indicated that the Goldwyer Formation is calcareous-dominated in different parts of the Canning Basin, including the Barbwire Terrace. It has also locally undergone a significant secondary dolomitization (Core Lab, 2013). Another confidential well completion report in the Canning Basin looked into Goldwyer III core and reported an average matrix density of 2.73 g/cc. This value was

implemented as the matrix density of the Goldwyer in our density porosity estimation. Water density is 1.1 g/cc (for marine water), oil density is 0.8 g/cc, and density of kerogen usually ranges between 1.2-1.4 g/cc (Tissot & Welte, 1978; Smithson, 2012; Gonzalez et al., 2013; Speight, 2014). The density of kerogen is sensitive to its maturity. Ward (2010) illustrated how we can derive kerogen density from vitrinite reflectance, Eq.3.12 (Ward, 2010; Labani & Rezaee, 2015). An average T_{max} value for samples of the Goldwyer Formation in the Barbwire Terrace is 435°C. According to Jarvie et al. (2001), this is equivalent to 0.7 $\%R_o$ (Eq.2.1), which results in kerogen density of 1.2 g/cc once calculated from Eq.3.12.

$$\rho_{kerogen} = 0.342R_o + 0.972 \tag{3.12}$$

Similarly, sonic porosity was used for total porosity estimation in the Barbwire Terrace for wells with available sonic log transit time across the Goldwyer Formation. Well Solanum 1 had to be dropped from this approach as it had no sonic information across the Goldwyer. Values of parameters related to this approach include compressional transit time of matrix, kerogen, water and oil (Eq.2.19). Matrix transit time (compressional sonic) was assigned to be 51 us/ft, a mid value between carbonate and shale transit times. Compressional sonic of kerogen was given to be 120 us/ft. DT_{water} was assigned the value of 185 us/ft (medium salinity). Lastly, DT_{oil} was set to be 238 us/ft (Glover; Schlumberger, 2009; Alford et al., 2012). Table 3.3 lists all parameters utilized for density and sonic porosity estimations.

Table 3.3 Parameters used for estimating density and sonic porosities.

Density Porosity Parameters				Sonic Porosity Parameters			
ρ_{ma}	ρ_{oil}	ρ_{water}	ρ_{TOC}	DT_{ma}	DT_{TOC}	DT_{water}	DT_{oil}
2.73	0.8	1.1	1.2	51	120	185	238

Parameters used for the density porosity approach are better defined and more reliable than those of sonic porosity. Furthermore, the resultant log density porosity (DPHI) is more stable with reasonable estimations than that of sonic porosity (Figure 3.19). Sonic porosity logs (SPHI) appear to be unstable, spiky (noisy), and overestimate porosity. Thus, it was assertively decided to use density porosity (DPHI) as the total porosity approach for wells in the Barbwire Terrace.

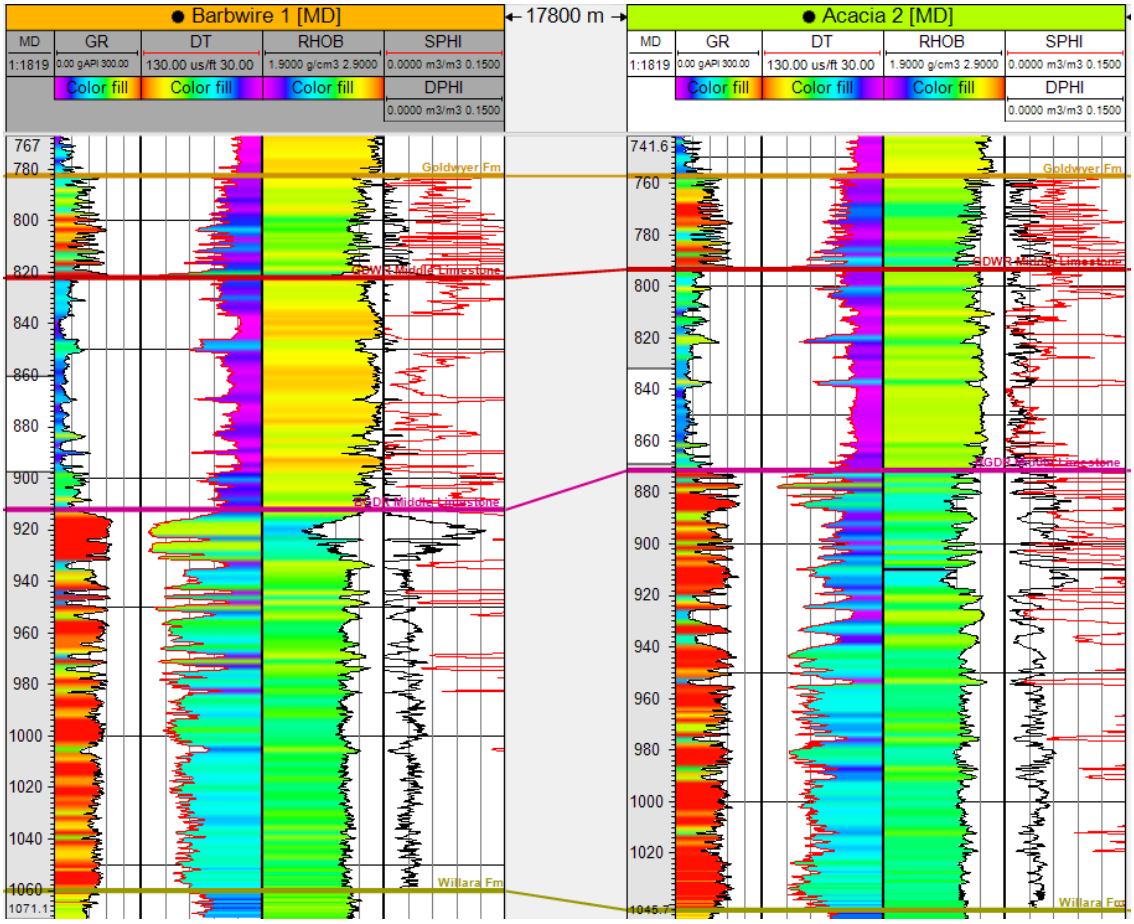

Figure 3.19 A well cross-section showing the difference between the estimated density porosity DPHI (black curve) and sonic porosity SPHI (red curve).

Similar to the estimation of water saturation, the limestone (non-shaly) intervals, which predominantly occur in the Goldwyer II zone, had their porosities calculated differently. Typical limestone matrix density (2.71 g/cc) was used to estimate density porosity, where kerogen density was irrelevant as TOC is effectively zero in these sections. In theory, density porosity values and neutron porosity readings should be the same in a limestone interval that is fully saturated with water (Glover; Selley, 1998). In reality, those sections might not be 100% limestones and/or our assigned parameters can be slightly off, so a difference between the two porosities is expected. Therefore, the resultant average porosity between DPHI and NPHI is taken as the total estimated porosity. This approach was applied for all intervals with the volume of shale less than 15%.

Consequently, the resultant total porosity (PHIT) consists of density porosity for most of the Goldwyer (V_{sh}>15%), and an average porosity of DPHI and NPHI for the non-shaly intervals (V_{sh}<15%). The total porosity log is fairly stable with reasonable values. Porosity is lowest in the Middle Goldwyer Zone (Goldwyer II), which is thought to be the zone of lowest TOC richness and predominantly consists of tight carbonate rock. Porosity estimation generally increases in the other two zones of Upper and Lower Goldwyer (Figure 3.20).

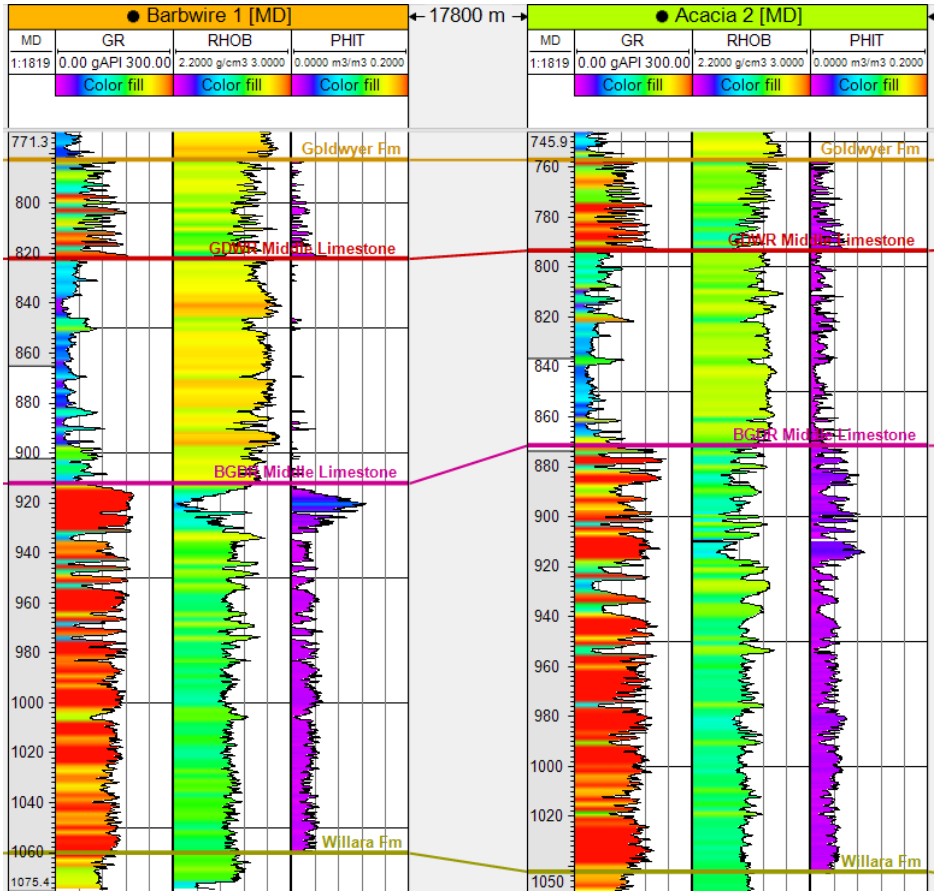

Figure 3.20 A well cross-section showing estimated total porosity (PHIT) for the Goldwyer Formation. Barbwire 1 and Acacia 2 are shown here as an example.

3.4 Brittleness Index

Brittleness can be simply described as the measurement of the ability for a rock to fracture. This property is dependent on various rock factors, including mineralogy, porosity, and effective stress (Wang & Gale, 2009). It is generally expressed in terms of Brittleness Index (BI), which can be calculated by solely using lithology information, $BI_{lithology}$ (Eq.2.20). Alternatively, the brittleness index can be defined using the geomechanical elastic properties of the shaly rocks, BI_{sonic} (Eq.2.25).

A comparison between the brittleness indices derived from mineralogy and sonic was presented by Labani and Rezaee (2015). $BI_{mineralogy}$ and BI_{sonic} cross-plots show fair correlation between the two different methods for the XRD determined mineralogy example (Figure 3.21). However, $BI_{mineralogy}$ is thought to have less reliable estimations, as it only looks at the mineralogy of the rock. This is an important factor in determining the brittleness of the rock, but not the only one as previously discussed. Therefore, BI_{sonic} is thought to account for several brittleness factors and hence generate more accurate estimations. For those reasons, the BI_{sonic} approach was utilized in this study.

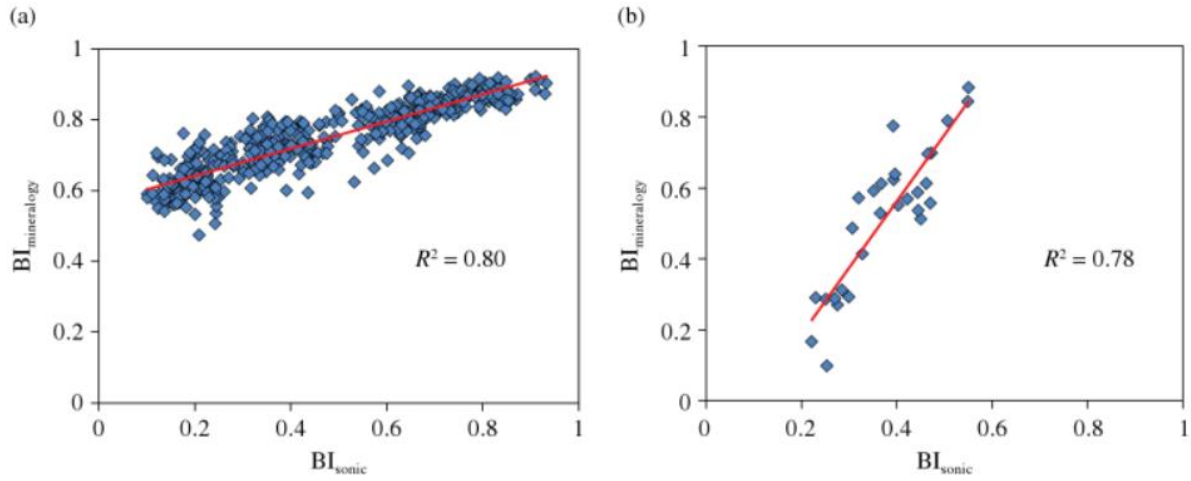

Figure 3.21 Analysis between $BI_{mineralogy}$ and BI_{sonic} for two wells in Perth Basin, WA. Mineralogy in well (a) was determined using log data, whereas XRD analysis was used for well (b) (Labani & Rezaee, 2015).

Prior to estimating BI_{sonic}, calculating both Young's modulus (Eq.2.21) and Poisson's ratio (Eq.2.22) is required. Shear velocity (V_s) data are not available in wells of the Barbwire Terrace. V_s data are therefore derived from the relationship proposed by Castagna et al. (1985) in Eq.2.26.

The resultant Young's modulus and Poisson's ratio are then normalized before undergoing the estimation of the Brittleness Index. The normalization, however, uses the minimum and maximum values that are only extracted from parts of the Goldwyer where V_{sh} more than 50%, to ensure that the normalization process is tailored around the shaly sections of the Goldwyer Formation.

A well section of some key wells in the Barbwire Terrace with brittleness data is shown in Figure 3.22. The middle Goldwyer zone is the most brittle. Lower brittleness values are observed in the top and lower Goldwyer zones.

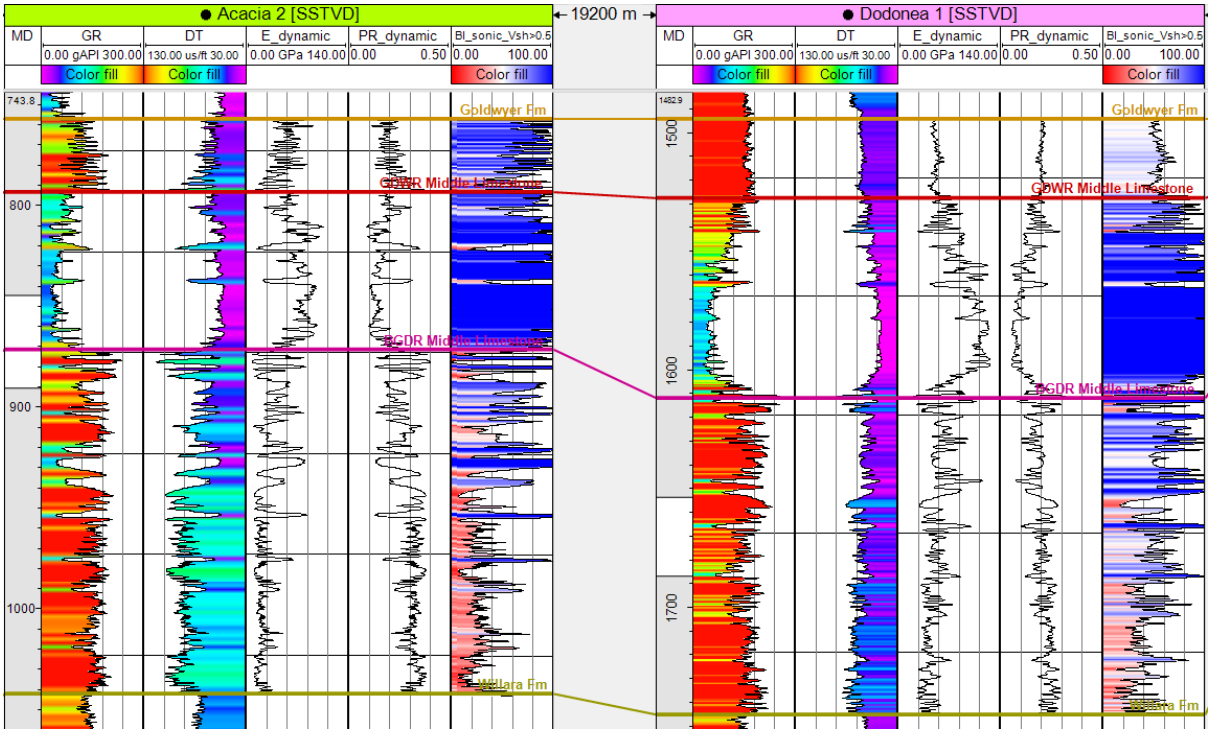

Figure 3.22 A well cross-section showing estimated brittleness index and the corresponding Young's modulus and Poisson's ratio. Acacia 2 and Dodonea 1 are shown here as an example of key wells in the Barbwire Terrace.

Chapter 4. Property Modelling

4.1 Surface Generation

Formation surfaces are essential for building any model. In this study, surfaces were generated using well tops data. Those surfaces are the main structural inputs for the property models, which only contain the Goldwyer Formation and assess property estimation and distribution. Therefore, only surfaces necessary for building the whole Goldwyer section were generated; Goldwyer I, Goldwyer II, Goldwyer III, and Willara (base of Goldwyer Formation).

Given the limited well control and the uneven well distribution across the Barbwire Terrace (Figure 3.1), a considerable amount of extrapolation is undertaken in some parts of the terrace. In such case, surface intersections and pinch-outs commonly occur, especially between closely spaced generated surfaces (Figure 4.1a). Such inaccurate geologic features occur because surface generation algorithms tend to estimate surfaces independently from each other.

The utilized software, *Petrel*, offers a tool that generates surfaces simultaneously while incorporating conformability information into the generation process. This algorithm also appears to struggle in generating fully conformable surfaces in the Goldwyer section. In many instances, the surface trends upward and intersects the overlaying surface, the algorithm then tries to correct and forces the surface downward resulting into rough and still non-conformable surfaces (Figure 4.1b).

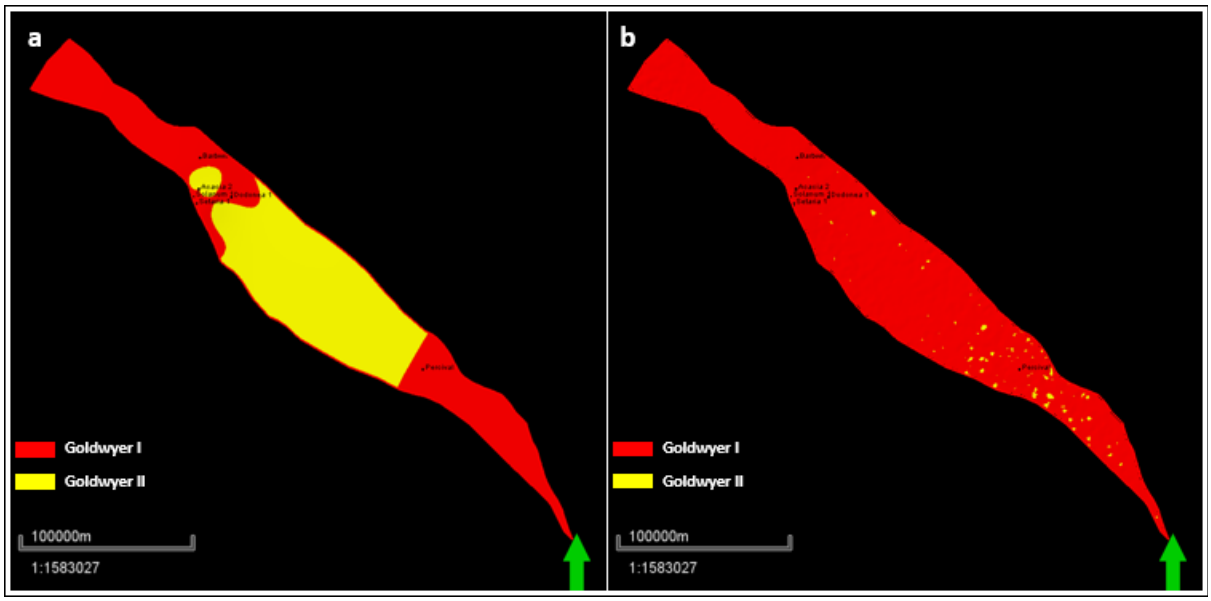

Figure 4.1 (a) Generated surfaces intersect each other due to lack of well control in some parts of the Barbwire Terrace. (b) Utilizing different surface generation algorithms (Horizon Modelling) still provide non-conformable surfaces.

Alternatively, pseudo-wells with pseudo well tops have been utilized in areas that lack well control. Such points help to guide the algorithm to generate conformable and geologically sound surfaces. Additionally, neighbouring well tops outside the Barbwire Terrace were also implemented to adequately expect the logical behaviour of the surface at the terrace's boundary (Figure 4.2). Needless to mention, this step can be harmful in building any model if data was assigned prematurely. Careful placement of formation tops and zone thicknesses is a crucial step in this process. Hence, a sufficient geological understanding of the formation extension and structure is

necessary. In this study, this approach has proven to be most effective in providing best geologically estimated surfaces of the Goldwyer zone in the Barbwire Terrace (Figure 4.3).

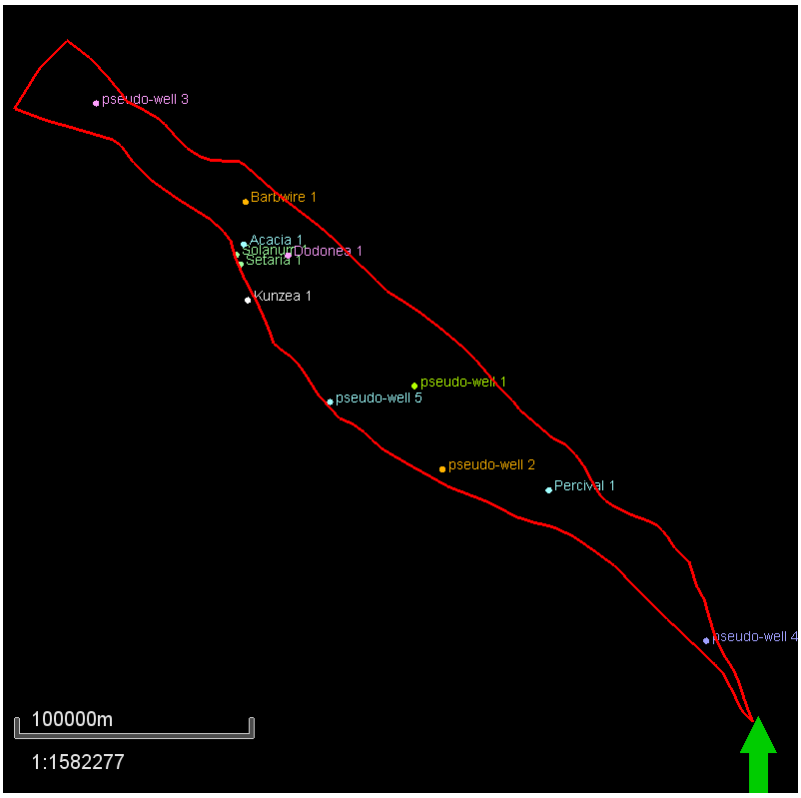

Figure 4.2 This Barbwire Terrace boundary map shows key wells within the terrace, pseudo-wells, and one example of a neighbouring well outside the terrace that were all implemented in the surface generation process.

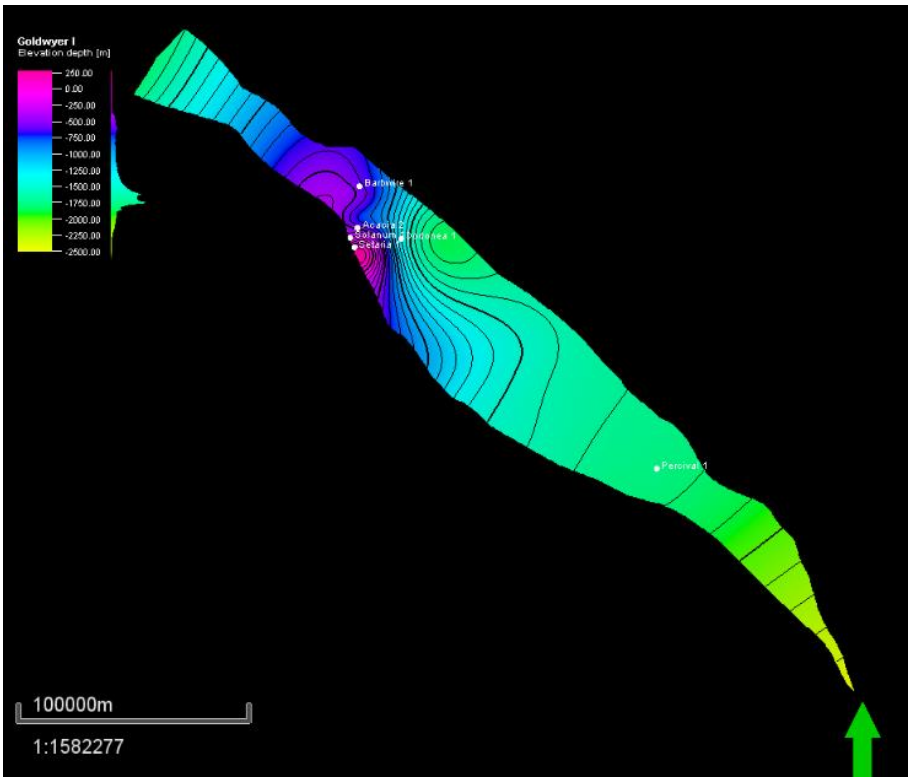

Figure 4.3 Goldwyer I surface here is conformably overlaying the other remaining surfaces. Added data points have helped generating conformable surfaces that agree with our geological understanding of the terrace.

4.2 Model Generation

With the surfaces of interest have been generated, building a structural model is now feasible. This is a simple model that is only considering the Goldwyer section and its boundaries. Surfaces used for the generation of the structural model were Goldwyer I (GDWR1), Goldwyer II (GDWR2), Goldwyer III (GDWR3), and Willara of the Barbwire Terrace. This has provided three main zones; Goldwyer I Zone (GDWR1-GDWR2), Goldwyer II Zone (GDWR2-GDWR3), and Goldwyer III Zone (GDWR3-Willara). The grid increment of the model was set to be 500 x 500 m. This is the lateral cell size of both *x* and *y* directions.

More information can be added to the structural model, such as fault surfaces and layering. No fault information has been incorporated in this study. However, subzones were integrated into the model. Goldwyer I (*Zone 1*) was divided into two subzones. The two subzones are identical in thickness. Goldwyer II (*Zone 2*) was split into three subzones of identical thicknesses. Whereas Godlwyer III (*Zone 3)* was divided into six subzones that are also identical in thickness.

The number of subzones for each zone was determined by the resultant average thickness of the subzones. The goal is to generate subzones with similar average thicknesses across the whole model (Table 4.1). This will make an assessment of different prospective subzones of the Goldwyer more reliable, as average maps are calculated and compared from all subzones. This step ensures that average maps are comparable across different zones as they have similar thicknesses.

Table 4.1 Average thicknesses of all zones and subzones of the generated model.

Zone	Zone Avg. Thickness (m)	Subzone	Subzone Avg. Thickness (m)
Goldwyer I	45.5	GDWR1a	22.7
		GDWR1b	
Goldwyer II	63.8	GDWR2a	21.3
		GDWR2b	
		GDWR2c	
Goldwyer III	120.6	GDWR3a	20.1
		GDWR3b	
		GDWR3c	
		GDWR3d	
		GDWR3e	
		GDWR3f	

Layering, which represents the model's vertical resolution, was then defined into the model. Looking into facies changes and well log behaviour, it is important to decide the appropriate vertical resolution for the model. Rock profiles with minimal change in characteristics can afford to have a coarse resolution. Similarly, Goldwyer II Zone has overall consistent lithology with minimum change in rock properties and therefore was assigned a vertical resolution of about 5 m in average. Goldwyer I & III, however, have more alternating facies and variable well logs characteristics. Subsequently, they were assigned a higher vertical resolution of about 3 m in average (Figure 4.4).

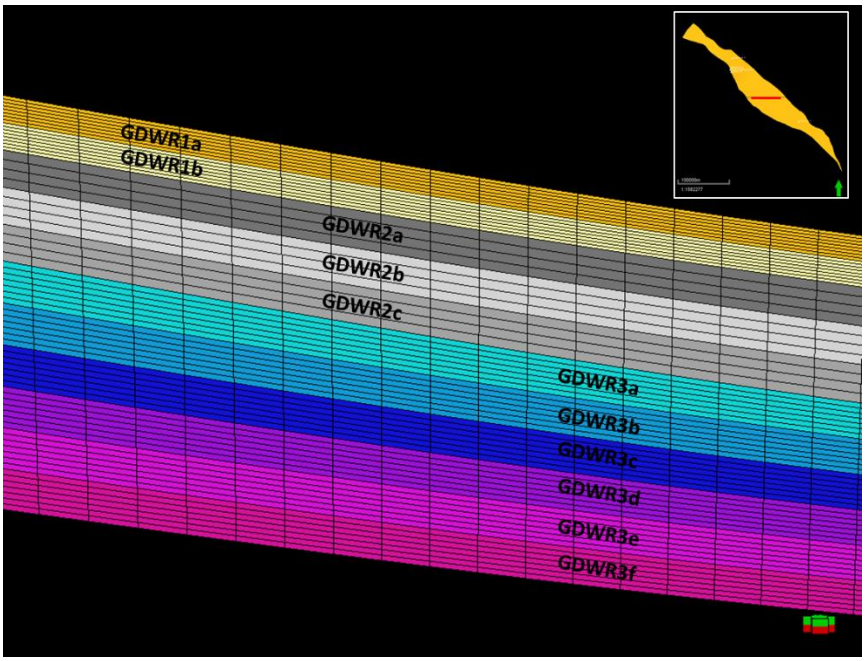

Figure 4.4 A cross section of the model illustrating the subzoning and vertical resolution.

4.3 Petrophysical Modelling

Once all geometrical aspects of the model were finalized, property modelling was carried out. The first step of this process was upscaling well logs. TOC, PHIT, S_w, and BI logs were upscaled to the model's vertical resolution. This was achieved by estimating a single property value for each vertical resolution block through arithmetic average method. Then a 3D petrophysical model for each property in the Barbwire Terrace was calculated using a Gaussian Random Function Simulations. The simulations used the default isotropic lateral distribution with a spherical variogram type. Since there is no evidence to assume a large difference between neighbouring samples (Clark, 2010), nugget value was kept small at 1 x 10^{-4} (Figure 4.5).

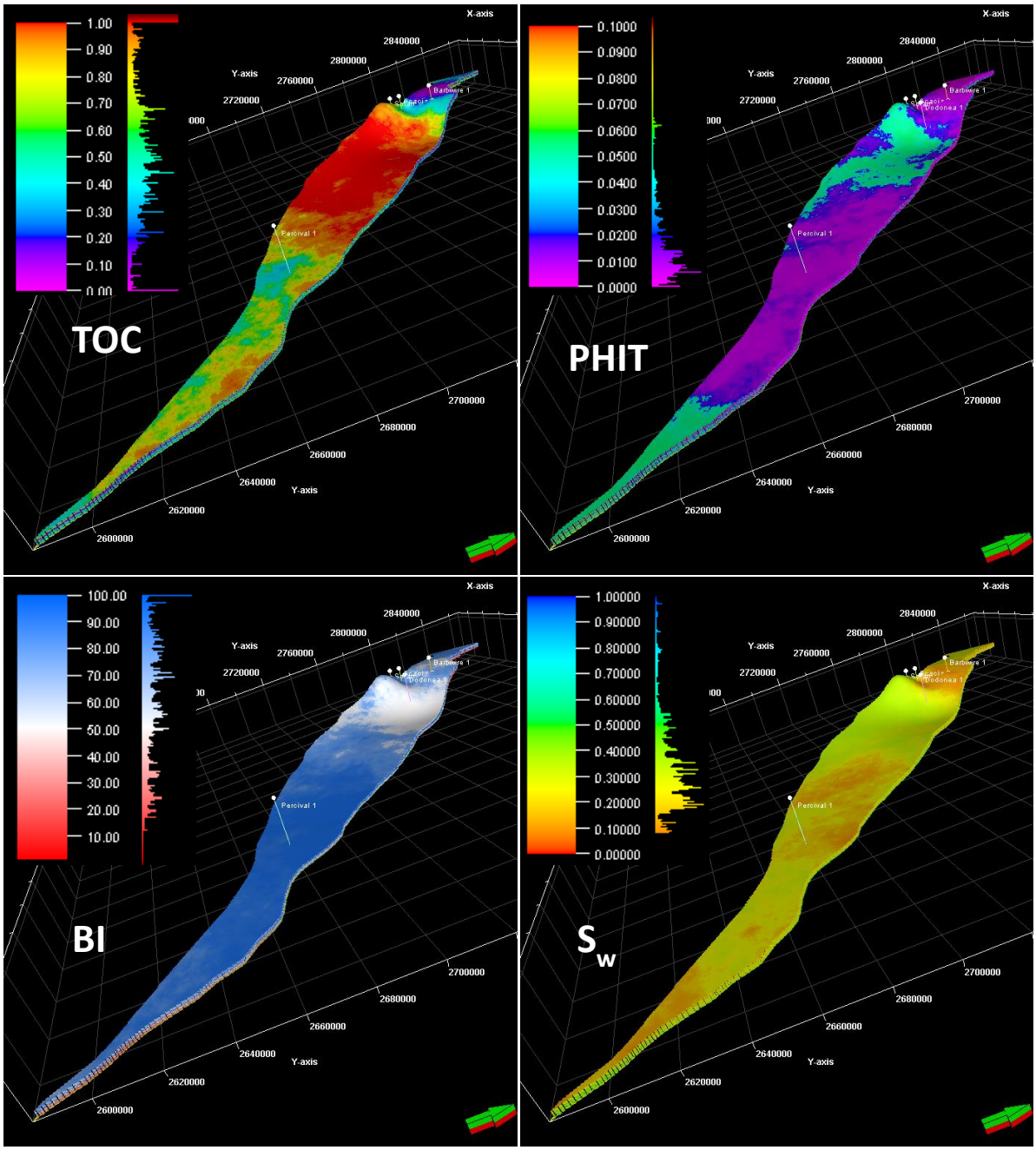

Figure 4.5 Property models for the Goldwyer Formation, Barbwire Terrace.

4.4 Model Average Maps

Sieving through all petrophysical models and evaluating areas of high and low potential is time-consuming and often impractical. For the purpose of this study, property average maps were generated for each subzone in the 3D model. This is a common practice to simplify the assessment of the prospectivity estimated by the model. Average maps have been generated for each property. There are eleven subzones in the model, where one average property map was produced for each subzone.

4.4.1 TOC Average Maps

The aforementioned average maps were generated for the TOC model. This, again, resulted in 11 TOC average maps; two in Goldwyer I, three in Goldwyer II, and six in Goldwyer III. An overview of those average maps can be seen in Figure 4.6.

Goldwyer I is the thinnest zone in the Goldwyer section. The two subzones making up the Goldwyer I show relatively high TOC values, where highest average TOC values are shown to be on the southern flanks of the central part of the Barbwire Terrace. TOC values in this area have averages higher than 1 %.

Looking into the maps, GDWR1b has higher average TOC values than the above GDWR1a subzone. The northwestern part of the Barbwire Terrace appears to have higher average TOC values in GDWR1b. This is also true in most of the central parts of the terrace.

Goldwyer II is thought to be lean limestone zone, with the least prospectivity. Consequently, lowest average TOC values can be observed here in the three subzones making up this mainly middle limestone section. GDWR2a subzone shows relatively higher average TOC values than the other two subzones, however, values are still too low for any prospectivity consideration.

The thickest Goldwyer section is the Goldwyer III zone. It consists of six subzones. The top subzone GDWR3a shows relatively the highest average TOC values. The second top subzone GDWR3b shows the second highest average TOC values. Generally in this zone, the deeper it is, the less average TOC maps are observed.

In summary, average TOC values are highest in the top zone of Goldwyer I, where GDWR1b has the highest average TOC values than any other part of the model, which reinforces Cadman et al. (1993) statement of the top Goldwyer zone being the most prospective in terms of TOC. On the other hand, Goldwyer II is the least prospective with the lowest TOC values. As for the lower Goldwyer zone (Goldwyer III), top subzones show higher average TOC values than the lower ones. However, no subzone in the Goldwyer III shows average TOC values as high as those in Goldwyer I.

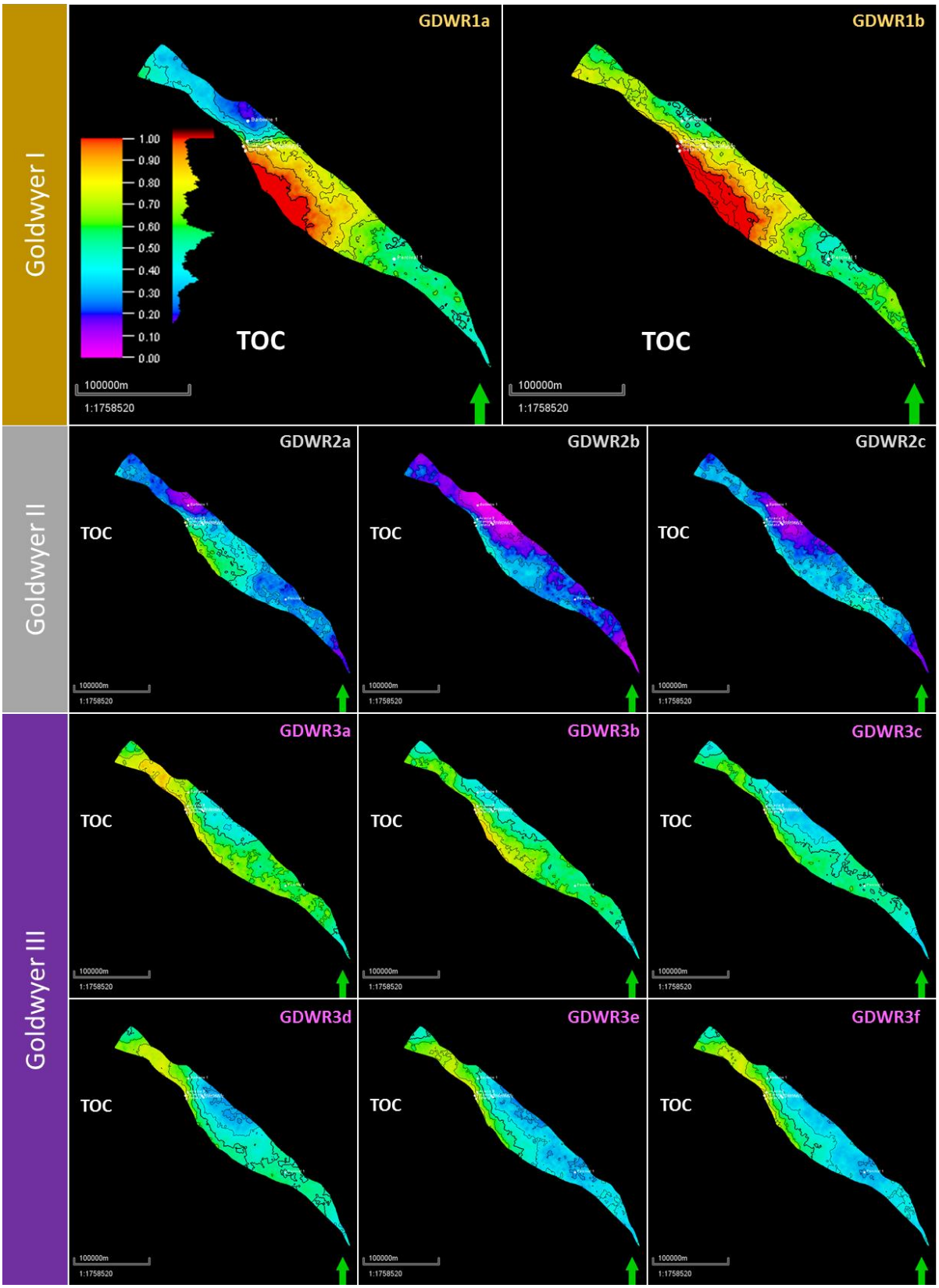

Figure 4.6 TOC property model average maps for each subzone in the Goldwyer. Colour scale legend is displayed for the top subzone and is representative for all maps.

4.4.2 S_w Average Maps

Similar to TOC assessment, S_w model was averaged into eleven average maps based on the model subzones. A property average map has been generated for each subzone in the model. In this case, this resulted in eleven water saturation average maps (Figure 4.7). Both average maps in Goldwyer I show similar average values and trends of water saturation distributions. The S_w model in this zone shows less water saturation in the north western and south eastern areas of the Barbwire Terrace.

Subzones in the middle limestone section show the highest water saturation estimates in the Goldwyer. This is in agreement with the independent water saturation logs estimated for each well in the Barbwire Terrace independently. The lean non-shaly intervals tend to be fully water saturated.

In Goldwyer III, water saturation average maps generally show less saturation in the north western and south eastern parts of the terrace. GDWR3b is the subzone with least water saturation average values in the whole Goldwyer III section.

In general, all average maps in Goldwyer I & III of the model show values that are within the low range of water saturation. Goldwyer II zone is the only section in the Barbwire Terrace that is deemed non-prospective for being predominantly water saturated.

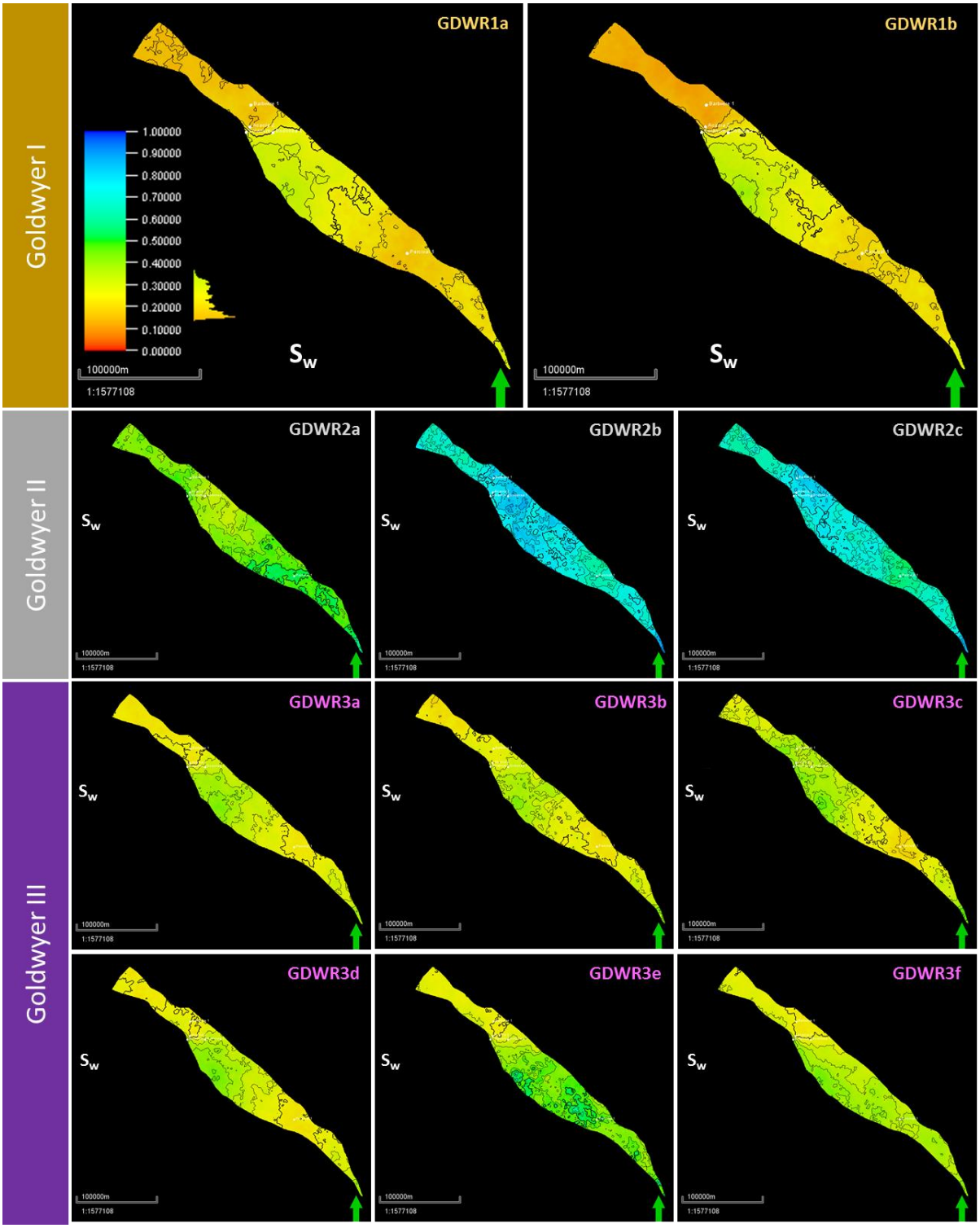

Figure 4.7 S_w property model average maps for each subzone in the Goldwyer. Colour scale legend is displayed for the top subzone and is representative for all maps.

4.4.3 PHIT Average Maps

An overview of the eleven PHIT average maps can be seen in Figure 4.8. The two subzones of Goldwyer I show similar trends and data distribution. Both maps show an increase in PHIT data around the western central parts of the Barbwire Terrace, especially in the vicinity of the wells Acacia 2 and Solanum 1. Slightly more data with higher average PHIT are observed in GDWR1a than those in the lower GDWR1b subzone.

The middle section (Goldwyer II), which mostly consists of lean and tight limestone, has the lowest average total porosity values. All three subzones of this section indicate very low porosity estimations. GDWR2a and GDWR2b show slightly higher average porosity values in the proximity of Solanum 1. This slight increase in a limited location is insignificant for an overall assessment of the whole Goldwyer II zone.

Average PHIT maps in Goldwyer III show increase in average porosity in the northwestern part of the Barbwire Terrace. All six subzone maps show consistent behaviour and similar data distribution. GDWR3a, however, shows highest average PHIT values of ~8%.

To summarize, both Goldwyer I & III zones show good average PHIT estimations with similar value ranges. Nevertheless, areas of higher porosity values are different from one zone to the other. Central and western central parts of Goldwyer I in the Barbwire Terrace have higher average porosity estimations, wherein the Goldwyer III of the terrace higher PHIT average values appear in the northwest part of the terrace.

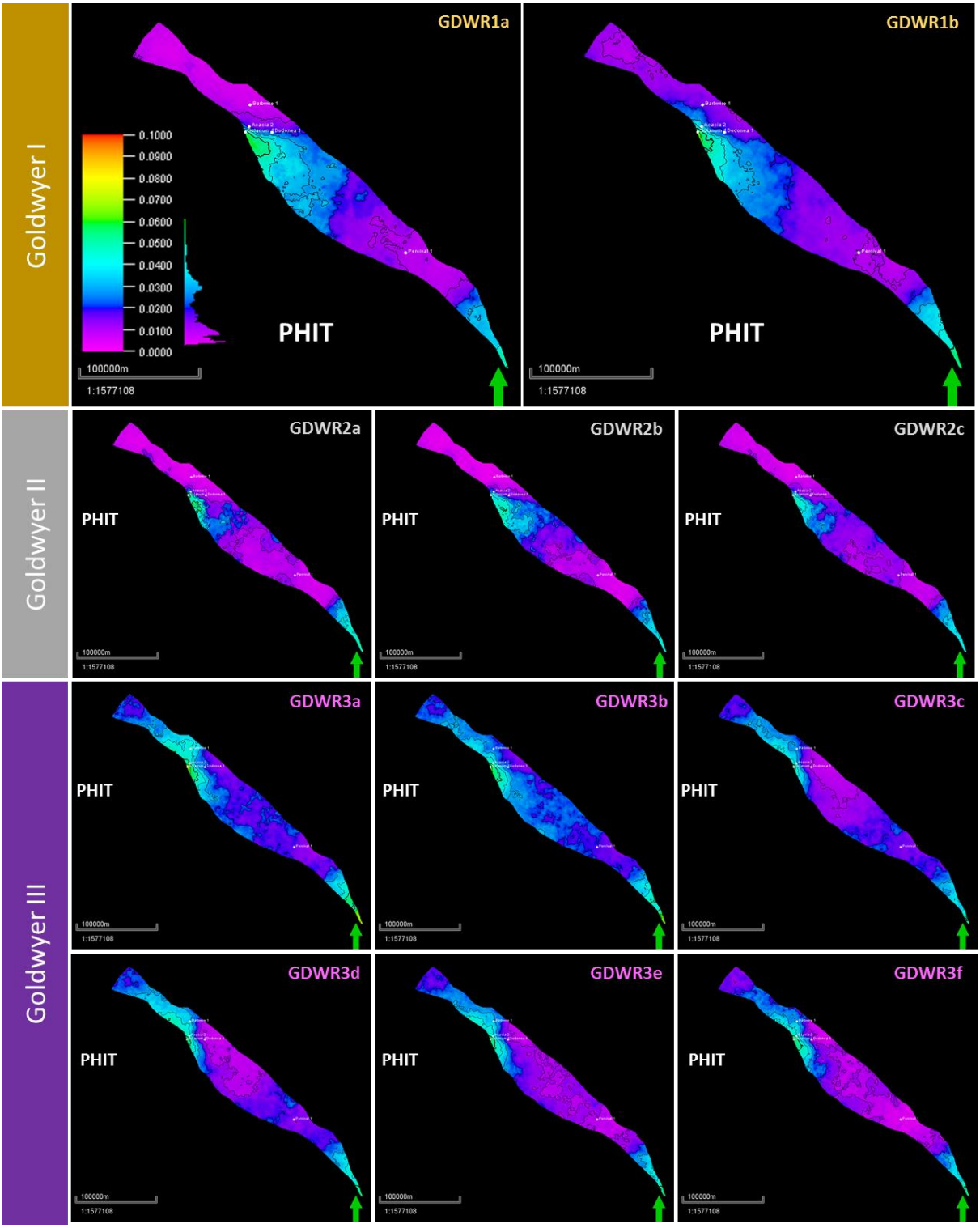

Figure 4.8 PHIT property model average maps for each subzone in the Goldwyer. Colour scale legend is displayed for the top subzone and is representative for all maps.

4.4.4 BI Average Maps

Following the previously discussed properties, the Brittleness Index model was split into eleven average maps, one average map for each subzone in the model (Figure 4.9). Similar BI average values appear in both subzones of the Goldwyer I. GDWR1a has slightly higher BI average values than the lower subzone, especially in the northwestern part of the terrace.

Since the middle limestone zone is lean and tight, it is likely to be most brittle. The BI average maps of Goldwyer II show just that. They have the highest brittleness index in the model, where GDWR2b is the most brittle out of the three subzones.

Goldwyer III has a wider range of brittleness values. Almost all maps in this zone have more brittle rock in the central part of the terrace than north western and south eastern parts. This is consistent with the TOC and PHIT maps. Areas with higher TOC and PHIT tend to be relatively less brittle. That said, GDWR1a and GDWR 1b are mapped with the highest contrast between areas of high and low BI average maps.

In summary, the most brittle subzone in the whole model is GDWR2b. Outside the non-prospective most-brittle zone (Goldwyer II), Goldwyer I and more specifically GDWR1a is the most brittle rock in the subzones of Goldwyer I & III.

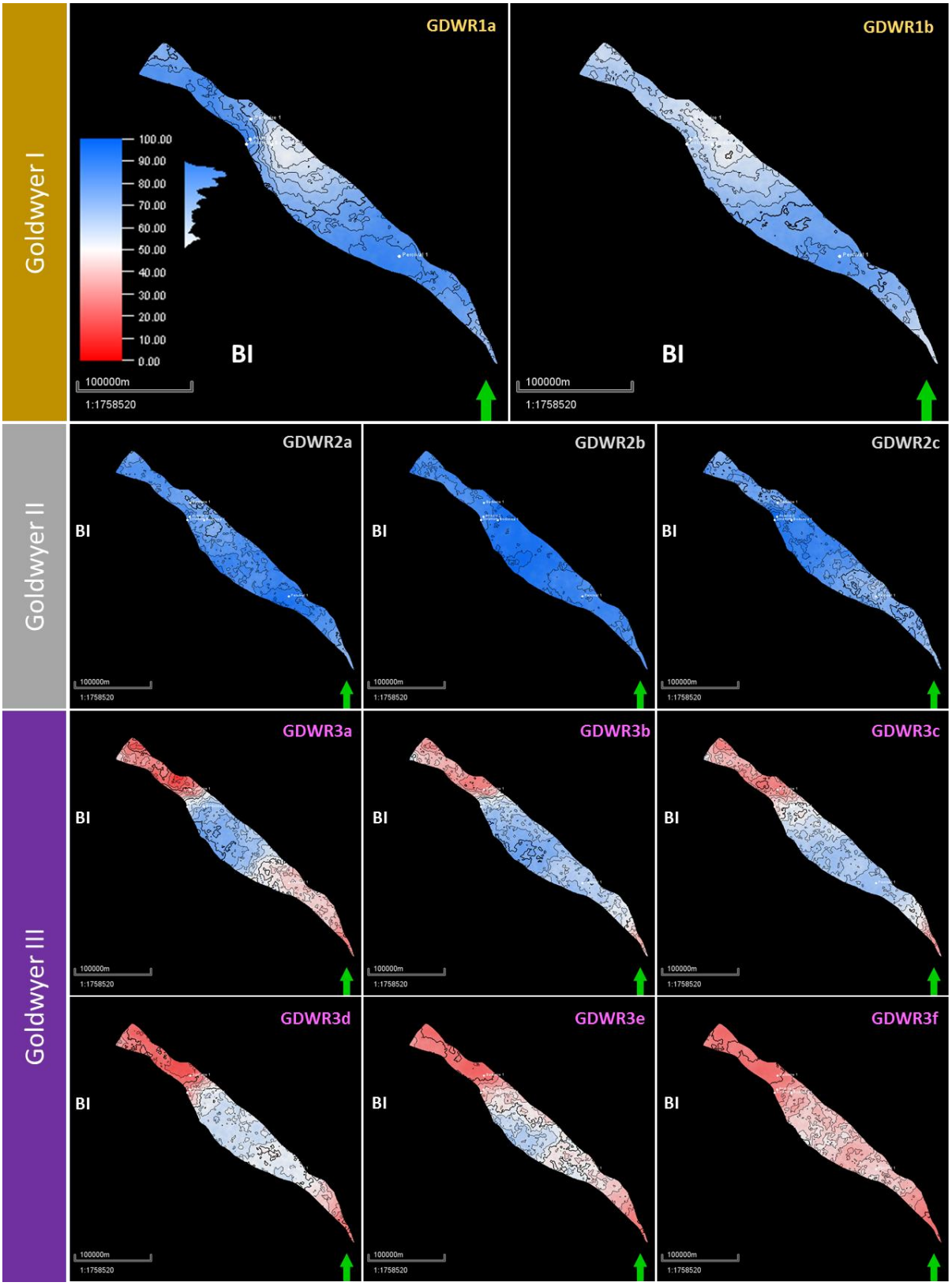

Figure 4.9 BI property model average maps for each subzone in the Goldwyer. Colour scale legend is displayed for the top subzone and is representative for all maps.

4.5 Sweet-Spot Mapping

A practical approach of combining different analytical information for a certain shale play is sweet-spot mapping. The process aims to simplify the prospectivity evaluation of a shale play, where property modelling is often involved. It is utilized to combine whatever data or models deemed necessary to provide a critical assessment of the unconventional resource. This could include a wide range of information, such as petrophysical models, geophysical attributes, structural information, geomechanical data, and production history.

A main objective of this study is to look into the formation evaluation aspects of the Goldwyer Formation. Consequently, the associated sweet-spot mapping is combining the four key properties estimated earlier in the study; TOC, PHIT, S_w, and BI. For such a combination to be valid, all properties are normalized so that adding different petrophysical models together can be meaningful. However, normalizing property average maps should not be done independently. Same normalization parameters of each property are applied to all subzone average maps. This is essential to keep each property comparable across the different zones and subzones.

Before combining the different properties together, analyzing each one individually is required to see what the resultant values would indicate. Higher values of TOC, PHIT, and BI all suggest higher prospectivity of the Goldwyer Formation. However, higher S_w values suggest the opposite. In order to make such property combination meaningful, we replace S_w with S_h (Eq.2.14), so that higher values of any property suggest higher prospectivity of the shale and vice versa.

Thickness information was integrated into all generated petrophysical models as part of the model's main structure. In the form of average property maps, however, thickness and all other structural information are eliminated. There is an average thickness of each map, which is highlighted in Table 4.1, but no actual thickness data across the map. Since thickness plays an important factor in the prospectivity of the shale play, where thicker prospective shale is favourable and more prospective than a thin one, thickness was also incorporated in the calculation of the sweet-spot maps in addition to the other four estimated properties. Thickness isochore maps for each subzone were normalized to be implemented in the sweet-spot map estimation. Similar to the other properties, the normalization process is not done independently for each subzone isochore, same parameters are applied to all thickness maps across the Goldwyer.

Properties are added in a weighted manner, each shale play has some properties that are more important than others. For example, a shale play could have relatively high TOC values all across the formation, but the abundance of clay could deem the source rock non-prospective for adequate hydraulic stimulation and sufficient production. This example would entitle clay content or brittleness index to have a higher weight than TOC in generating sweet-spot maps.

In the case of the Barbwire Terrace, however, brittleness index and hydrocarbon saturation of the shaly sections of the Goldwyer Formation suggest overall consistent rock quality. On the other hand, TOC and PHIT values tend to be too low in some areas where they are considered non-prospective. As a result, BI and S_h average maps were given relatively lower weights of 0.18 each, thickness was given the same weight as well. TOC and PHIT were given weights of 0.23 each, the sum of all utilized weights must be one. The resultant sweet-spot map of each subzone can be expressed in Eq.4.1.

$$Sweet\ Spot\ Map = TOC(0.23) + PHIT(0.23) + S_h(0.18) + BI(0.18) + Thk(0.18) \qquad (4.1)$$

Where *TOC*, *PHIT*, S_h, and *BI* are all normalized property average maps of each subzone. *Thk* is the normalized thickness of each subzone. Based on the maturity information in Section 2.2, the Barbwire Terrace is generally considered to be mature in the oil generation window and hence no maturity information was incorporated in the sweet-spot approach.

The resultant maps represent the prospectivity of the Goldwyer expressed in the four combined properties plus thickness. The values of the maps range between 0 and 1, where 0 is least prospective and 1 is the highest estimated prospectivity of Goldwyer. In further discussions, these values will be referred to as *prospective values*.

Chapter 5. Discussion and Conclusion

5.1 Analyses of Estimated Properties

With all four properties estimated (Figure 5.1), a better analysis of the Goldwyer Formation in the Barbwire Terrace can be carried out. Original log information is always valuable for formation evaluation. However, porosity, TOC, water saturation, and brittleness are, in this case, key properties for evaluating the prospectivity of the Goldwyer as a shale play.

Derived TOC data across wells in the Barbwire Terrace show lowest values in Goldwyer II. This is expected as this middle zone is known to be lean and mainly consist of tight limestone. Goldwyer I and III, however, contain varying quantities of TOC and certainly appear to be more prospective than Goldwyer II. Zones with highest TOC values can slightly vary from one well to another. Overall TOC values tend to be highest at the bottom of Goldwyer I and top of Goldwyer III. The Goldwyer Formation may have gone through deposition of relatively abundant amounts of organic matter in anoxic conditions, interrupted by the deposition of the middle limestone zone where very limited organic matter had been deposited and preserved. Nevertheless, the TOC values of the Goldwyer Formation in the study area are generally quite low. All TOC measurements and estimated values are less than 2.5%.

The derived properties are often influenced by one another. A clear example is the TOC and porosity logs. They both have similar signatures across the whole Goldwyer section. Density was the main input for the estimation of both properties, which will result in both logs being highly influenced by the same property, and hence some similarities can be observed. However, the porosity of shale plays, in many cases, tends to mimic TOC regardless of the derivation approach. As TOC increases, there is a higher chance of hydrocarbon generation that will be hosted in pore spaces. Furthermore, kerogen-hosted porosity would increase as there is more TOC, and hence more kerogen in the rock. Consequently, a strong agreement between porosity and TOC logs is often regarded to porosity being abundantly hosted in the organic matter. This is often verified by scanning electron microscope (SEM) imaging.

Subsequently, porosity values tend to be highest in the top of Goldwyer III and the bottom of Goldwyer I. Slightly lower porosity appears in the remaining parts of the two zones. The Goldwyer II, however, mainly consists of tight limestone with porosity values close to zero. Density porosity values of the Goldwyer Formation are overall below 10%.

In theory, Water saturation should somewhat be related to TOC as well. An increase in TOC could potentially increase hydrocarbon generation, which by definition would decrease water saturation. In general, estimated S_w shows reasonable water saturation quantities across the shaly Goldwyer intervals of values that range around 15 – 30%. High water saturation values are found in the lean tight carbonate intervals, which are predominant in Goldwyer II and sometimes in Goldwyer III. This was manually edited after confirming the lack of any hydrocarbon traces from mud gases and other hydrocarbon tests across such intervals, as discussed earlier.

Brittleness index estimation was carried out as an attempt to measure the ability of the rock to break. This indicates how the rock would react to hydraulic fracturing process in a well completion stage. The presence of clays and organic matter tends to influence the brittleness index negatively. Such compositions are more lenient to be ductile. Furthermore, lean non-porous intervals generally tend to be more brittle than their porous and organic-rich counterparts. On the other hand, the abundance of calcite or silica in the rock commonly lead to a more brittle interval. Shales often would have variable brittleness index based on the change of composition of the shale interval. The Goldwyer Formation is no exception, the low TOC, low porosity, and high calcite content zone of

Goldwyer II has the highest brittleness index values of the whole Goldwyer section. In Goldwyer I and III where we have variable compositions and changing amounts of TOC and porosity, brittleness index would be variable accordingly. This does not indicate that wherever there is high TOC, there is ductile rock. TOC is one factor out of many that influence brittleness. Some wells show BI average of about 35% in Goldwyer I and III, where others can go higher than 50% while containing similar amounts of TOC. Even though the highest brittleness index values are in Goldwyer II, this does not necessarily suggest that brittleness is non-prospective in all other sections. In fact, Goldwyer I and III have various sufficient brittle intervals with BI values higher than 50% (Figure 5.1).

Spiky behaviour and sudden variations in logs can be observed in data of most properties of the Goldwyer. In most cases, such a behaviour suggests a laminated shale. Those laminations represent sudden changes in rock properties resulted by changes of conditions during deposition. Those laminae appear to have relatively low TOC, low porosity, high water saturation, and high brittleness index. This reinforces the concept of cyclic sediments and thin limestone interbeds stated by Haines (2004).

Such phenomenon has the potential to cause some challenges along the way. For instance, the laminae-induced highly variable brittleness in some intervals could act as a geomechanical barrier of hydraulic fracture propagation. Furthermore, intervals with high lamina frequency could also end up producing more water than anticipated. This case emphasizes the significance of well placement and how considering such occurrences along the process can decide how successful a certain well is.

Goldwyer I and III generally show prospective values of different key properties. However, the bottom section of Goldwyer I and the top part of Goldwyer III are optimized shale intervals. They contain the highest TOC and porosity, low water saturations, and adequately high brittleness. The laminations are somewhat minimized in those intervals in some wells but still exist, nonetheless. As a result, laminations could be an occurrence that needs to be analyzed and worked around, once they are confirmed to pose issues in completed future wells in the area.

In most cases, the values of TOC and porosity are in the low-end corresponding to borderline prospective shales. Therefore, the generally low values of the two properties are believed to be the most important factors in deciding the prospectivity of the Goldwyer in the terrace.

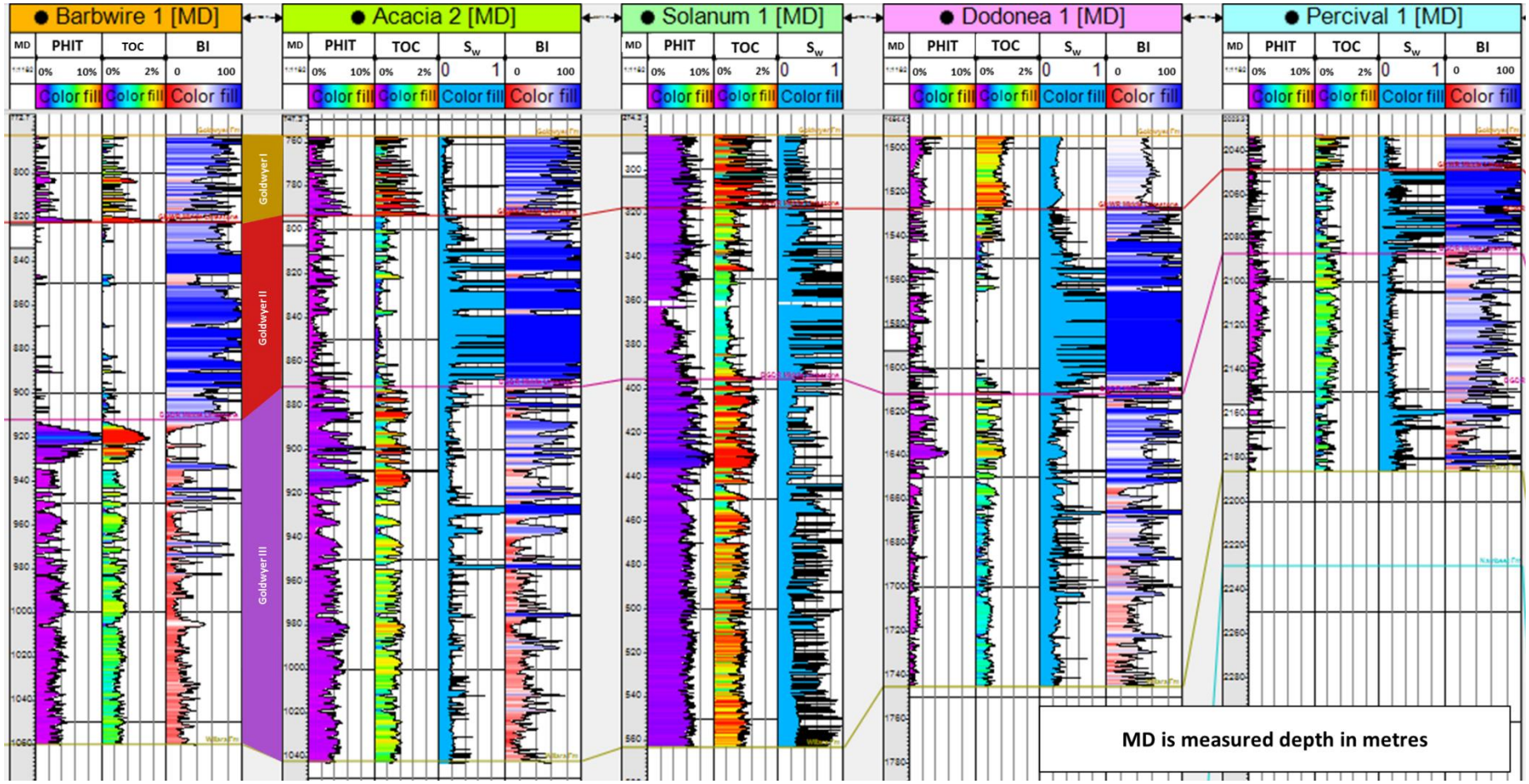

Figure 5.1 Well cross-section showing all four estimated properties of all five key wells in the Barbwire Terrace.

5.2 Overview of Sweet-Spot Models

Eleven sweet-spot maps were generated, one for each subzone in the Goldwyer. An overview of all sweet-spot maps can be seen in Figure 5.2. The least prospective section of the model is Goldwyer II (Zone 2). This is expected, as the middle Goldwyer is known to be lean carbonate zone. Subzones in Goldwyer III have varying potential, upper subzones seem to be more prospective. This is especially highlighted in the top two subzones; GDWR3a and GDWR3b. However, the most prospective zone in the model is Goldwyer I, where both subzones appear to be relatively more prospective than any other subzone in the model. Nonetheless, the deeper GDWR1b shows more prospectivity than the shallower GDWR1a subzone.

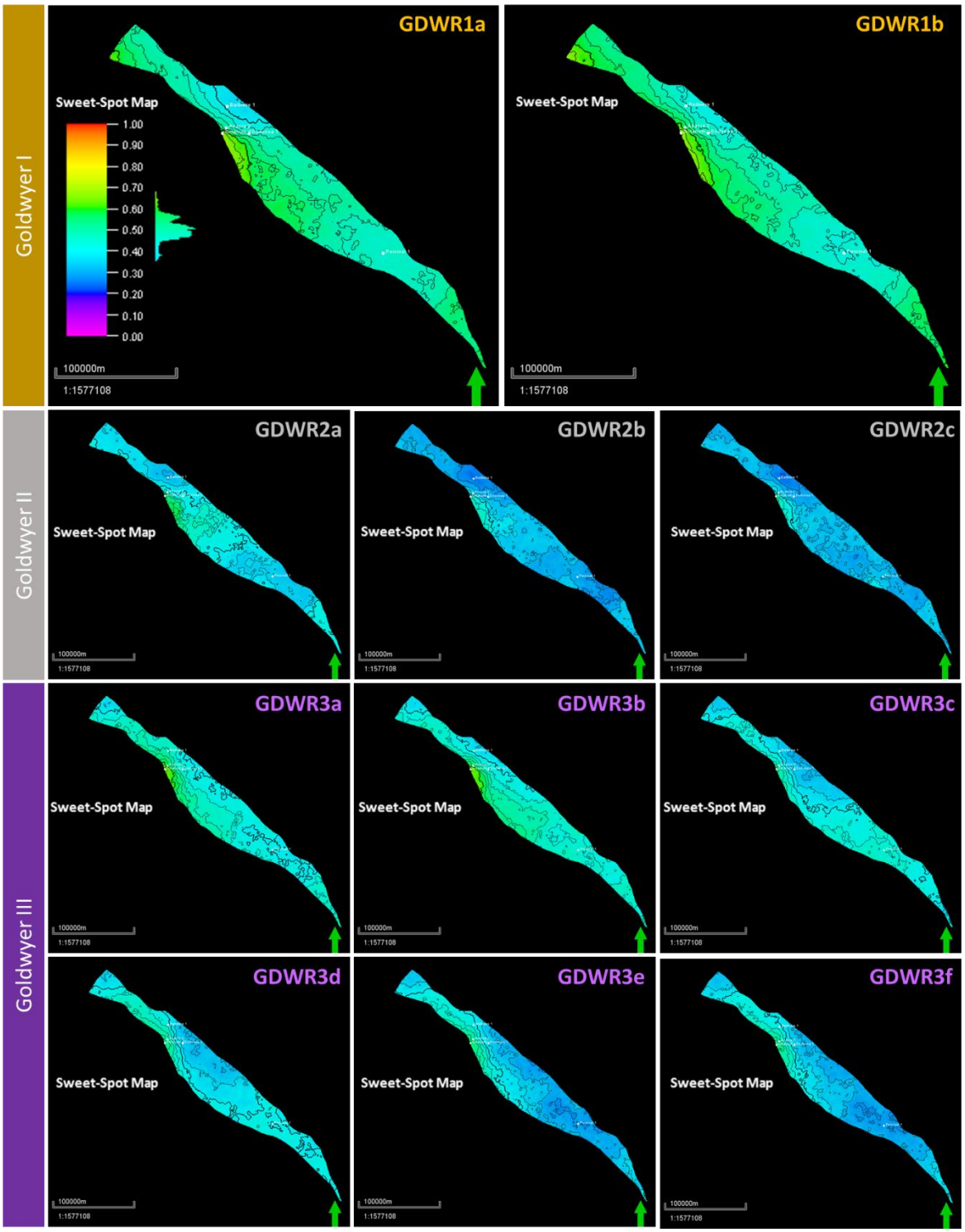

Figure 5.2 Sweet-spot maps for all subzones of the Goldwyer Formation model, Barbwire Terrace. Colour scale legend is displayed for the top subzone and is representative for all maps.

A common characteristic of sweet-spot maps of all subzones is that prospective values tend to generally improve around the areas of Acacia 2, and Solanum 1 wells. Those wells have relatively higher TOC and PHIT values. Other common high prospective values are those that appear at the north-western end of the terrace and are mainly caused by the anticipated thickness increase interpreted from the surface generation model.

One sweet-spot map representing all zones of the Goldwyer in the Barbwire Terrace was also produced (Figure 5.3). It attempts to provide a single solution for the Goldwyer assessment process and it gives a much broader overall analysis than that of the more focused eleven-subzone sweet-spot maps. The resultant map shows higher prospective values in the middle and north-western parts of the terrace. More specifically, the southern flanks of north-western and middle areas are more prospective than others. This is rather consistent with the trend we have seen from different maps of individual subzones.

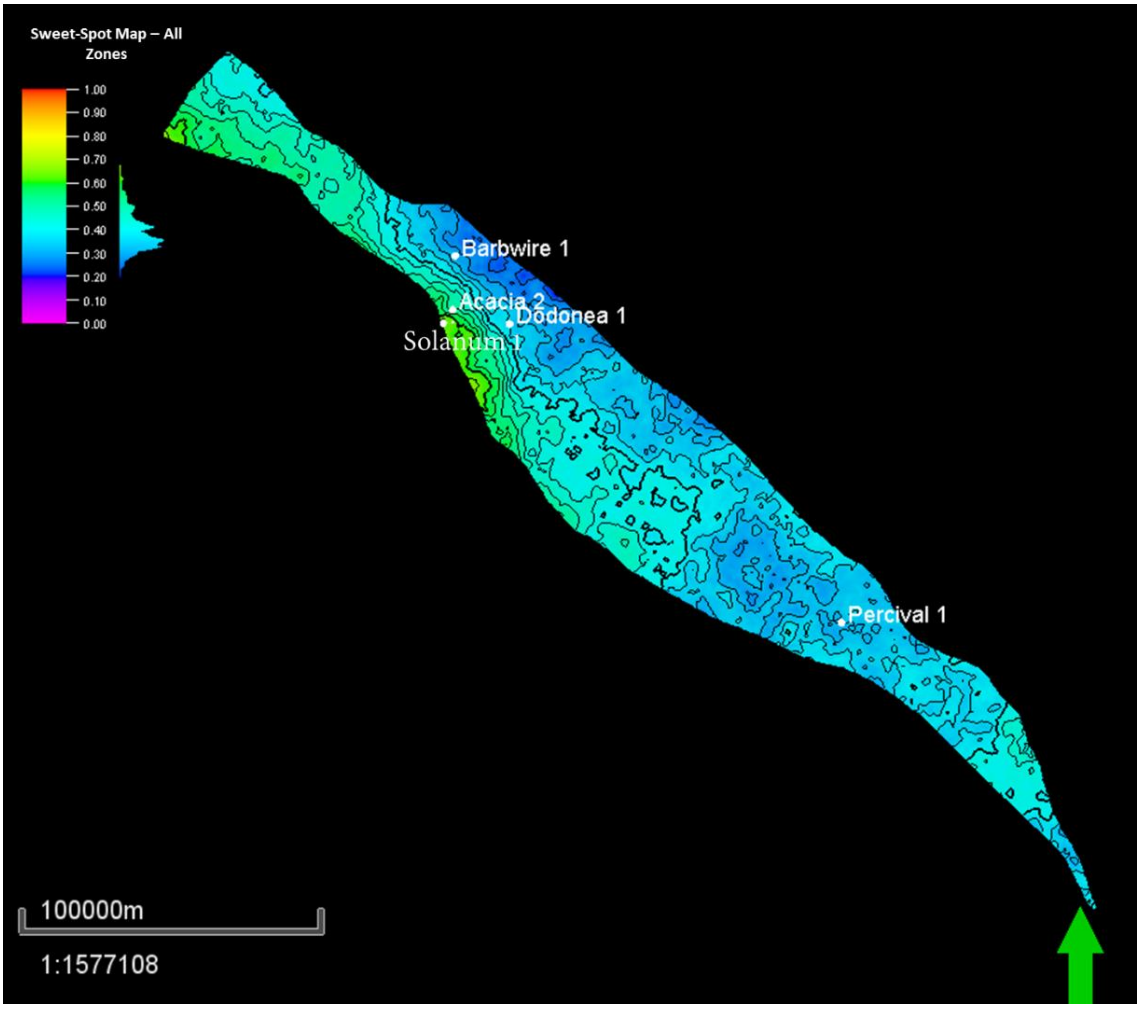

Figure 5.3 Sweet-Spot map of the whole Goldwyer Formation in the Barbwire Terrace.

It is noteworthy that this specific sweet-spot mapping approach can be misleading in the case of drastic value increases or decreases. For example, a relatively very high increase in thickness can indicate an area to be quite prospective even if it had too low TOC content for a sufficient hydrocarbon production. Therefore, sweet-spot maps can be alternatively estimated after applying cut-off values for each property. Those cut-offs eliminate all areas where each property is deemed non-prospective for a successful shale and the resultant sweet-spot maps only show areas where all properties have prospective overlaps.

Assigning cut-off values is somewhat subjective. Nevertheless, the TOC cut-off was given to be 1%, where all areas of TOC averages less than 1% were eliminated. Similarly, porosity was given a cut-off value of 3%. Whereas general cut-off values for brittleness index and hydrocarbon saturations were considered 50% and 55%, respectively. No cut-off value was applied for thickness but it was analyzed for the resultant areas. In this case, the resultant average maps are not normalized but instead

converted to volume fractions by dividing each map by its maximum value. Similar to the previous approach, the volume fraction estimations are not done independently for each subzone, a same maximum value is applied to all maps across the Goldwyer. This is, again, significant to keep each property comparable across the different subzones. Sweet-spot maps are then calculated using Eq.4.1, where TOC, PHIT, S_h, BI, and Thk are all volume fraction maps instead of normalized ones.

All subzone average maps of Goldwyer II and III do not pass the cut-off conditions, where TOC and PHIT maps generally do not pass their cut-off values. In fact, only small areas of GDWR1a and GDWR1b pass those conditions.

Based on the conditions applied, the resultant maps are only showing the southern flanks in the middle Barbwire Terrace to be prospective in the top two subzones of GDWR1a and GDWR1b (Figure 5.4). It is noteworthy that the thickness of those areas for each subzone ranges between 14 - 22 m. The same areas were also the most prospective in the previous approach. However, the potentially prospective areas of the northwest portions of the Barbwire Terrace in the earlier sweet-spot maps are deemed non-prospective here. The thickness increase suggested a prospective section in the previous method. With cut-offs applied, however, TOC appears to be too low for prospectivity considerations.

Nonetheless, it is essential to note that lateral extensions of prospective areas in the cut-off approach would vary based on the thickness of the subzones. For example, if we treat the Goldwyer section as a whole and produce one average map of each property for the whole formation, no area across the Barbwire Terrace would be considered prospective based on our cut-off conditions. The reason is that the generally thin intervals of prospective shales are masked by the thick non-prospective intervals. On the other hand, if average maps were taken for thinner subzones, those prospective intervals would be more prominent and hence prospective areas would be more laterally extended, while being vertically reduced. This emphasizes some limitations of the average maps and how they should not be analyzed independently. Well data and 3D property models should be incorporated into the assessment process to provide a sufficient shale evaluation.

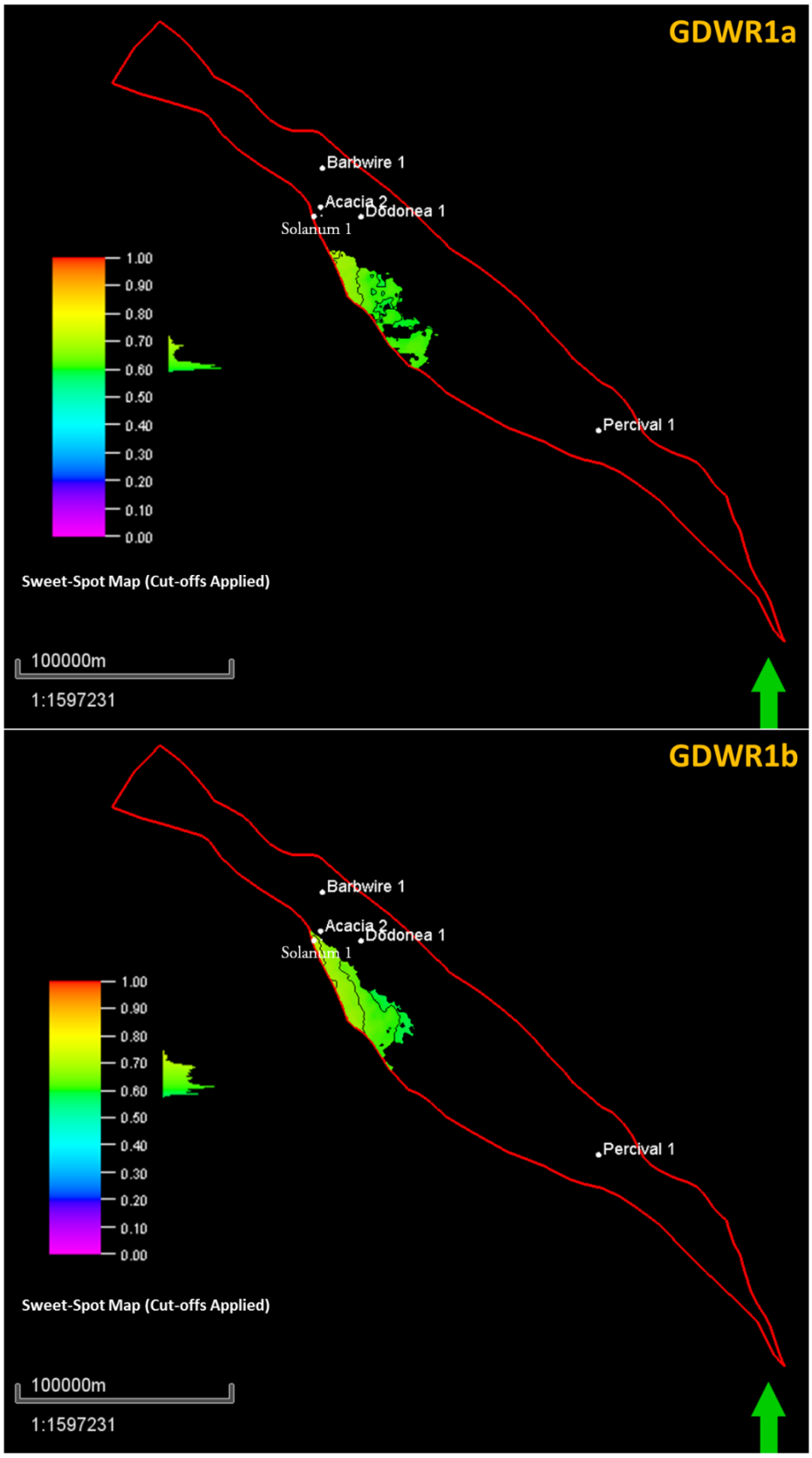

Figure 5.4 Sweet-spot maps for all subzones that pass the cut-off value conditions applied on all four properties. The populated sections of the maps represent the locations where all cut-off conditions were met and overlapped.

5.3 Significance and Considerations

This study provided a prospectivity assessment of the Goldwyer Formation as an unconventional resource. This was achieved by sweet-spot mapping through formation evaluation and petrophysical modelling of the shale play. Total organic carbon, total porosity, water saturation, and brittleness index were considered key properties of formation evaluation, and hence were all estimated for wells in the Barbwire Terrace.

Property estimations provided valuable information about the Goldwyer Formation as a potential unconventional resource. Water saturation values have shown to be generally around 30% or less in most non-lean shaly intervals. Brittleness index is quite variable across the Goldwyer, but generally showing values of sufficient brittleness for hydraulic stimulation. Total porosity values range between 0 to 10%, where porosities tend to be lowest in the lean carbonate intervals. Nonetheless, TOC can be considered the most significant property of all four since it has the lowest range of values of less than 2.5%. This low range of TOC can negatively affect the potential of the Goldwyer as a hydrocarbon resource more than any other estimated property. If future wells in the Barbwire Terrace show no improvement in TOC, hydrocarbon production of such intervals may turn out to be non-commercial.

Petrophysical modelling provided a geostatistical distribution of properties in the Barbwire Terrace. The generated models would be improved if more wells were incorporated with better scattering. Furthermore, such geostatistical distribution can be more informative if more data were inputted in the modelling process. For instance, fault models and 3D seismic attributes can uplift data distribution if incorporated in the petrophysical modelling process or even in surface generation. Although such data were either not available or outside the scope of this study, there is always room for improvement in any generated model as more data is acquired and interpreted.

The resultant one sweet-spot map generated for the whole Goldwyer provided a broad analysis of the shale play. It highlights the most prospective geographical locations of the Barbwire Terrace, which are the southern flanks of the middle and north-western part of the terrace. On the other hand, the generated eleven sweet-spot maps provide a more detailed look into different sections of the Goldwyer Formation, by which most prospective intervals can be identified. Such maps have shown that the top zone (Goldwyer I) is the most prospective zone of all three. Prospective values are the highest in GDWR1b. GDWR1a is a close second, where GDWR3a and GDWR3b come in third and fourth order, respectively. Applying cut-off values for the sweet-spot mapping process provided a more strict analysis of the Goldwyer Formation. Only limited areas of the southern flanks of the Barbwire Terrace of GDWR1b and GDWR1a showed prospectivity that have met the cut-off values conditions.

In summary, the most prospective section of the Goldwyer Formation is the bottom section of Goldwyer I. It has the highest TOC and porosity, with sufficient hydrocarbon saturation and brittleness index. Property modelling and sweet-spot mapping show that the most prospective area to target the bottom Goldwyer I in the Barbwire Terrace is the southern flank of the central part of the terrace. This where all studied properties are overlapping with prospective estimations.

Sweet-spot mapping is a valuable tool that attempts to simplify the complexity of shale play evaluation. The combination of different properties into one map provides a robust assessment of the shale play. Nevertheless, such maps should only be utilized as a reference summary of the assessment and not to replace the comprehensive interpretation of the individual properties. The more data incorporated into a sweet-spot map, the more meaningful it is.

Given the resulted observations, future studies can take an extended look at the further southern and western areas outside the Barbwire Terrace and into the Broome Platform where an

extrapolation of such prospective areas is expected. Studying the bounding layers of the Goldwyer Formation can also prove to be a necessary step to ensure a successful completion of any future Goldwyer wells. Such studies can assess the possibility of hydraulic fractures propagating into the bounding layers and any associated risk of water production. Furthermore, future studies can also aim to evaluate the significance of the depth of the Goldwyer and how variable depths can affect pore pressure and hence the production potential of the shale play, especially when the depth of the Goldwyer varies greatly in the Barbwire Terrace from few hundred to couple of thousand metres.

References

Alford, J., Blyth, M., Tollefsen, E., Crowe, J., Loreto, J., Mohammed, S., . . . Rodriguez-Herrera, A. (2012). Sonic Logging While Drilling - Shear Answers. *Oilfield Review, Schlumberger, 24*(1).

Apak, S. N., & Carlsen, G. M. (1997). *A compilation and review of data pertaining to the hydrocarbon prospectivity of the Canning Basin / by S.N. Apak and G.M. Carlsen*. East Perth, W.A: Geological Survey of Western Australia.

Archie, G. E. (1942). The Electrical Resistivity Log as an Aid in Determining Some Reservoir Characteristics. doi:10.2118/942054-G

Brown, S. A., Boserio, J. M., Jackson, K. S., & Spence, K. W. (1984). *The Geological Evolution of the Canning Basin: Implications for Petroleum Exploration.* Paper presented at the Proceedings of Geological Society of Australia/Petroleum Exploration Society of Australia Symposium, Perth.

Cadman, S. J., Pain, L., Vuckovic, V., & Le Poidevin, S. R. (1993). Canning Basin, W.A. *Australian Petroleum Accumulation, Department of Primary Industries and Energy Bureau of Resource Sciences, Petroleum Resource Branch*(Report 9).

Carey, S. W. (1976). *The Expanding Earth* (Vol. 10): Elsevier.

Castagna, J. P., Batzle, M. L., & Eastwood, R. L. (1985). Relationships between compressional-wave and shear-wave velocities in clastic silicate rocks. *GEOPHYSICS, 50*(4), 571-581. doi:10.1190/1.1441933

Clark, I. (2010). Statistics or geostatistics? Sampling error or nugget effect? *The Journal of The Southern African Institute of Mining and Metallurgy, 110*, 307-312.

Cluff, B., & Miller, M. (2010). Logs Evaluation of Gas Shales: a 35-year Perspective. Denver, CO: Presentation, DWLS Luncheon.

Cook, P. J., & Totterdell, J. M. (1990). *THE ORDOVICIAN PALAEOGEOGRAPHY OF AUSTRALIA*. Retrieved from Australian Petroleum Industries Research Association:

Core Lab. (2013). *A study of the Goldwyer and Nita Formations from 8 wells, Canning Basin, Western Australia*. Retrieved from

Crowe, R. W. A., Gibson, D. L., & Towner, R. R. (1978). Permian and Mesozoic geology of the Derby and Mount Anderson 1:250 000 sheet areas, Western Australia. *Bureau of Mineral Resources, Australia, Record 1978/8*.

Dellisanti, F., Pini, G. A., & Baudin, F. (2010). Use of Tmax as a thermal maturity indicator in orogenic successions and comparison with clay mineral evolution. *Clay Minerals, 45*(1), 115-130. doi:10.1180/claymin.2010.045.1.115

Druce, E. C., & Radke, B. M. (1979). *The geology of The Fairfield Group, Canning Basin, Western Australia*. Bureau of Mineral Resources, Geology and Geophysics: Australian Government Publishing Service.

Edwards, D. S., Summons, R. E., Kennard, J. M., Nicoll, R. S., Bradshaw, M., Foster, C. B., . . . Zumberge, J. E. (1997). Geochemical Characteristics of Palaeozoic Petroleum Systems in Northwestern Australia. *APPEA Journal, 37*, 351-377.

Energy Information Administration. (2013). *Technically Recoverable Shale Oil and Shale Gas Resources: An Assessment of 137 Shale Formations in 41 Countries Outside the United States*. U.S. Department of Energy.

Forman, D. J., & Wales, D. W. (1981). *Geological evolution of the Canning Basin, Western Australia*. Bureau of Mineral Resources, Geology and Geophysics: Australian Government Publishing Service.

Foster, C. B., O'Brien, G. W., & Watson, S. T. (1986). Hydrocarbon Source Potential of the Goldwyer Formation, Barbwire Terrace, Canning Basin, Western Australia. *APEA Journal, v. 26*, 142-155.

France, R. E. (1986). *Percival No. 1 Well Completion Report*. Retrieved from https://wapims.dmp.wa.gov.au/WAPIMS/Search/WellDetails#

France, R. E., & Scibiarski, J. (1984). *Solanom No. 1 Well Completion Report, Canning Basin*. Retrieved from https://wapims.dmp.wa.gov.au/WAPIMS/Search/WellDetails#

Franquet, J. A., Bratovich, M. W., & Glass, R. D. (2012). *State-of-the-Art Openhole Shale Gas Logging*. SPE Saudi Arabia Section Technical Symposium and Exhibition, Al-Khobar, Saudi Arabia. 10.2118/160862-MS.

Glorioso, J. C., & Rattia, A. J. (2012). *Unconventional Reservoirs: Basic Petrophysical Concepts for Shale Gas*. SPE/EAGE European Unconventional Resources Conference and Exhibition, Vienna, Austria. 10.2118/153004-MS.

Glover, P. Petrophysics MSc Course Notes. University of Leeds, UK.

Gonzalez, J., Lewis, R., Hemingway, J., Grau, J., Rylander, E., & Schmitt, R. (2013). *Determination of Formation Organic Carbon Content Using a New Neutron-Induced Gamma Ray Spectroscopy Service that Directly Measures Carbon*. SPWLA 54th Annual Logging Sympsium.

Grieser, W. V., & Bray, J. M. (2007). *Identification of Production Potential in Unconventional Reservoirs*. SPE Production and Operations Symposium, Oklahoma City, Oklahoma. 10.2118/106623-MS.

Haines, P. W. (2004). *Depositional Facies and Regional Correlations of the Ordovician Goldwyer and Nita Formations Canning Basin, Western Australia with Implications for Petroleum Exploration*. Retrieved from

Hester, T. C., & Schmoker, J. W. (1987). *Determination of organic content from formation-density logs, Devonian-Mississippian Woodford Shale, Anadarko Basin, Oklahoma* (87-20). Retrieved from http://pubs.er.usgs.gov/publication/ofr8720

Jacobi, D. J., Breig, J. J., LeCompte, B., Kopal, M., Hursan, G., Mendez, F. E., . . . Longo, J. (2009). *Effective Geochemical and Geomechanical Characterization of Shale Gas Reservoirs From the Wellbore Environment: Caney and the Woodford Shale*. SPE Annual Technical Conference and Exhibition, New Orleans, Louisiana. 10.2118/124231-MS.

James, N. P. (1984). *Shallowing-upward sequences in carbonates, in Facies Models* (R. G. Walker Ed. 2 ed.): Geological Association of Canada.

Jarvie, D. M., Claxton, B., Henk, B., & Breyer, J. (2001). *Oil and Shale gas from the Barnett Shale, ft. Worth basin, Texas*. AAPG National Convention, Denver, CO.

Jarvie, D. M., Hill, R. J., Ruble, T. E., & Pollastro, R. M. (2007). Unconventional shale-gas systems: The Mississippian Barnett Shale of north-central Texas as one model for thermogenic shale-gas assessment. *AAPG Bulletin, 91*(4), 475-499. doi:10.1306/12190606068

Kamali, M. R., & Mirshady, A. A. (2004). Total organic carbon content determined from well logs using ΔLogR and Neuro Fuzzy techniques. *Journal of Petroleum Science and Engineering, 45*(3–4), 141-148. doi:http://dx.doi.org/10.1016/j.petrol.2004.08.005

Krief, M., Garat, J., Stellingwerf, J., & Ventre, J. (1990). A Petrophysical Interpretation Using The Velocities Of P And S Waves (full-waveform Sonic). *The Log Analyst, 31*(06).

Labani, M., & Rezaee, R. (2015). Petrophysical Evaluation of Gas Shale Reservoirs *Fundamentals of Gas Shale Reservoirs* (pp. 117-137): John Wiley & Sons, Inc.

Laurie, J. R. (1997). Early Ordovician fauna of the Gap Creek Formation, Canning Basin, Western Australia. *AGSO Journal of Australian Geology & Geophysics, 16(5)*, 701-716.

Legg, D. P. (1978). Ordovician biostratigraphy of the Canning Basin, Western Australia. *Alcheringa: An Australasian Journal of Palaeontology, 2*(4), 321-334. doi:10.1080/03115517808527788

Luffel, D. L., & Guidry, F. K. (1992). New core analysis methods for measuring reservoir rock properties of devonian shale. *Journal of Petroleum Technology; (United States)*, 1184-1190.

McCracken, S. R. (1994). *Timing of hydrocarbon migration into the Admiral Bay Fault Zone, Canning Basin, in The Sedimentary Basins of Western Australia.* Paper presented at the Petroleum Exploration Society of Australia, Western Australian Basins Symposium, Perth, WA.

McCracken, S. R. (1997). *Stratigraphic, diagenetic, and structural controls of the Admiral Bay carbonate-hosted Zn–Pb–Ag deposit, Canning Basin, Western Australia.* (PhD), University of Western Australia.

McCracken, S. R., Etminan, H., Connor, A. G., & Williams, V. A. (1996). Geology of the Admiral Bay carbonatehosted zinc–lead deposit, Canning Basin, Western Australia, in Carbonate-hosted lead–zinc deposits. *Society of Economic Geologists*(Special Publication no. 4), 330-349.

McTavish, R. A., & Legg, D. P. (1976). *The Ordovician of the Canning Basin, Western Australia.* Paper presented at the Proceeding of a Palaeontological Association Symposium, Birmington.

Menzel, B., & Norlin, K. (1982). *Great Sandy No. 1 Well Completion Report*. Retrieved from WAPIMS: https://wapims.dmp.wa.gov.au/WAPIMS/Search/WellDetails#

Nicoll, R. S. (1993). *Ordovician Conodont Distribution in Selected Petroleum Exploration Wells, Canning Basin, Western Australia*: Australian Government Publishing Service

Nicoll, R. S., Romine, K. K., & Watson, S. T. (1994). Early Silurian (Llandovery) conodonts from the Barbwire Terrace, Canning Basin, Western Australia. [northlimit=-16.0; southlimit=-24.0; westlimit=118.0; eastLimit=129.0; projection=GDA94].

Olson, R. K., & Grigg, M. W. (2008). *Mercury Injection Capillary Pressure (MICP) A Useful Tool for Improved Understanding of Porosity and Matrix Permeability Distributions in Shale Reservoirs*. AAPG Annual Convention, San Antonio, Texas.

Passey, Q. R., Creaney, S., Kulla, J. B., Moretti, F. J., & Stroud, J. D. (1990). A practical model for organic richness from porosity and resistivity logs. *AAPG Bulletin, 74*(12), 1777.

Playford, P. E. (1980). Devonian "Great Barrier Reef" of Canning Basin, Western Australia. *AAPG Bulletin, 64*(6), 814-840.

Porosity Logging. Retrieved from The Kansas Geological Survey: http://www.kgs.ku.edu/PRS/Info/pdf/doveton2.PDF

Rickman, R., Mullen, M. J., Petre, J. E., Grieser, W. V., & Kundert, D. (2008). *A Practical Use of Shale Petrophysics for Stimulation Design Optimization: All Shale Plays Are Not Clones of the Barnett Shale*. SPE Annual Technical Conference and Exhibition, Denver, Colorado, USA. 10.2118/115258-MS.

Royle, A., & Bezdan, S. (2001). *Shear-wave velocity estimation techniques: a comparison*. CSEG Convention.

Russell, T., & Edwards, H. (1984). *Cudalgarra-1 Final Well Report*. Retrieved from WAPIMS: https://wapims.dmp.wa.gov.au/WAPIMS/Search/WellDetails#

Schlumberger. (2009). Log Interpretation Charts.

Schmoker, J. W. (1979). Determination of organic content of Appalachian Devonian shales from formation-density logs. *AAPG Bulletin, 63*(9), 1504-1509.

Schmoker, J. W. (1989). Use of Formation-Density Logs to Determine Organic-Carbon Content in Devonian Shales of the Western Appalachian Basin and an Additional Example Based on the Bakken Formation of the Williston Basin. *Petroleum Geology of the Black Shale of Eastern North America*.

Schmoker, J. W., & Hester, T. C. (1983). Organic carbon in Bakken Formation, United States portion of Williston Basin. *AAPG Bulletin, 67*(12), 2165-2174.

Selley, R. C. (1998). *Elements of Petroleum Geology* (2 ed.): Academic Press.

Smithson, T. (2012). How Porosity Is Measured. *Oilfield Review, Schlumberger*, 63-64.

Sneider, R. M., Sneider, J. S., Bolger, G. W., & Neasham, J. W. (1997). Comparison of Seal Capacity Determinations: Conventional Core vs. Cuttings. *AAPG Memoir, 67*.

Sondergeld, C. H., Newsham, K. E., Comisky, J. T., Rice, M. C., & Rai, C. S. (2010). *Petrophysical Considerations in Evaluating and Producing Shale Gas Resources*. SPE Unconventional Gas Conference, Pittsburgh, Pennsylvania. 10.2118/131768-MS.

Speight, J. G. (2014). *The Chemistry and Technology of Petroleum, Fifth Edition*: CRC Press.

Summary of Petroleum Prospectivity: Canning Basin. (2014). Retrieved from Department of Mines and Petroleum, Petroleum Division:

Sun, S. Z., Sun, Y., Sun, C., Liu, Z., & Dong, N. (2013). *Methods of Calculating Total Organic Carbon from Well Logs and its Application on Rock's Properties Analysis*. GeoConvention 2013: Integration, Geoscience Engineering Partnership.

Tissot, B. P., & Welte, D. H. (1978). *Petroleum formation and occurrence: A new approach to oil and gas exploration*. New York: Springer-Verlag.

Towner, R. R., & Gibson, D. L. (1983). *Geology of the onshore Canning Basin, Western Australia*. Bureau of Mineral Resources, Geology and Geophysics: Australian Government Publishing Service.

Triche, N. E., & Bahar, M. (2013). *Shale gas Volumetrics of unconventional resource plays in the canning basin, western Australia*. SPE Unconventional Resources Conference and Exhibition-Asia Pacific. 10.2118/167078-ms.

Wang, F. P., & Gale, J. F. W. (2009). Screening Criteria for Shale-Gas Systems. *Gulf Coast Association of Geological Societies Transactions, V. 59, p. 779-793*.

WAPIMS. (2017). WA Petroleum & Geothermal Information Management System WAPIMS. Retrieved 20 Nov, 2015, from Department of Mines and Petroleum, Government of Western Australia https://wapims.dmp.wa.gov.au/wapims

Waples, D. W. (1985). *Geochemistry in Petroleum Exploration* (1 ed.): Springer Netherlands.

Ward, J. (2010). *Kerogen Density in the Marcellus Shale*. SPE Unconventional Gas Conference, Pittsburgh, Pennsylvania, USA. 10.2118/131767-MS.

Waters, G. A., Lewis, R. E., & Bentley, D. (2011). *The Effect of Mechanical Properties Anisotropy in the Generation of Hydraulic Fractures in Organic Shales*. SPE Annual Technical Conference and Exhibition, Denver, Colorado. 10.2118/146776-MS.

Watson, S., & Derrington, S. (1982). *Acacia No. 2 Well Completion Report, Canning Basin*. Retrieved from https://wapims.dmp.wa.gov.au/WAPIMS/Search/WellDetails#

Western Australia's Petroleum and Geothermal Explorer's Guide. (2014). Government of Western Australia: Department of Mines and Petroleum.

Winchester-Seeto, T., Foster, C., & O'Leary, T. (2000). The environmental response of Middle Ordovician large organic walled microfossils from the Goldwyer and Nita Formations, Canning Basin, Western Australia. *Review of Palaeobotany and Palynology, 113*(1–3), 197-212. doi:http://dx.doi.org/10.1016/S0034-6667(00)00060-9

Wust, R. A. J., Nassichuk, B. R., Brezovski, R., Hackley, P. C., & Willment, N. (2013). Vitrinite reflectance versus pyrolysis Tmax data: Assessing thermal maturity in shale plays with special reference to the Duvernay shale play of the western Canadian sedimentary basin, Alberta, Canada. *SPE Unconventional Resources Conference and Exhibition-Asia Pacific*. doi:10.2118/167031-ms

Yeates, A. N., Gibson, D. L., Towner, R. R., & Crowe, R. W. A. (1984). *Regional geology of the onshore Canning Basin, W.A.* Paper presented at the Geological Society of Australia and Petroleum Exploration Society of Australia Symposium, Perth.

Young, R. J. B. (1972). *Barbwire No. 1 Canning Basin Well Completion Report*. Retrieved from https://wapims.dmp.wa.gov.au/WAPIMS/Search/WellDetails#

Yu, G., & Aguilera, R. (2011). *Use of Pickett Plots for Evaluation of Shale Gas Formations*. SPE Annual Technical Conference and Exhibition, Denver, Colorado. 10.2118/146948-MS.

Yu, H., Rezaee, R., Wang, Z., Han, T., Zhang, Y., Arif, M., & Johnson, L. (2017). A new method for TOC estimation in tight shale gas reservoirs. *International Journal of Coal Geology, 179*, 269-277. doi:https://doi.org/10.1016/j.coal.2017.06.011

Zhao, H., Givens, N. B., & Curtis, B. (2007). Thermal maturity of the Barnett Shale determined from well-log analysis. *AAPG Bulletin, 91*(4), 535-549. doi:10.1306/10270606060